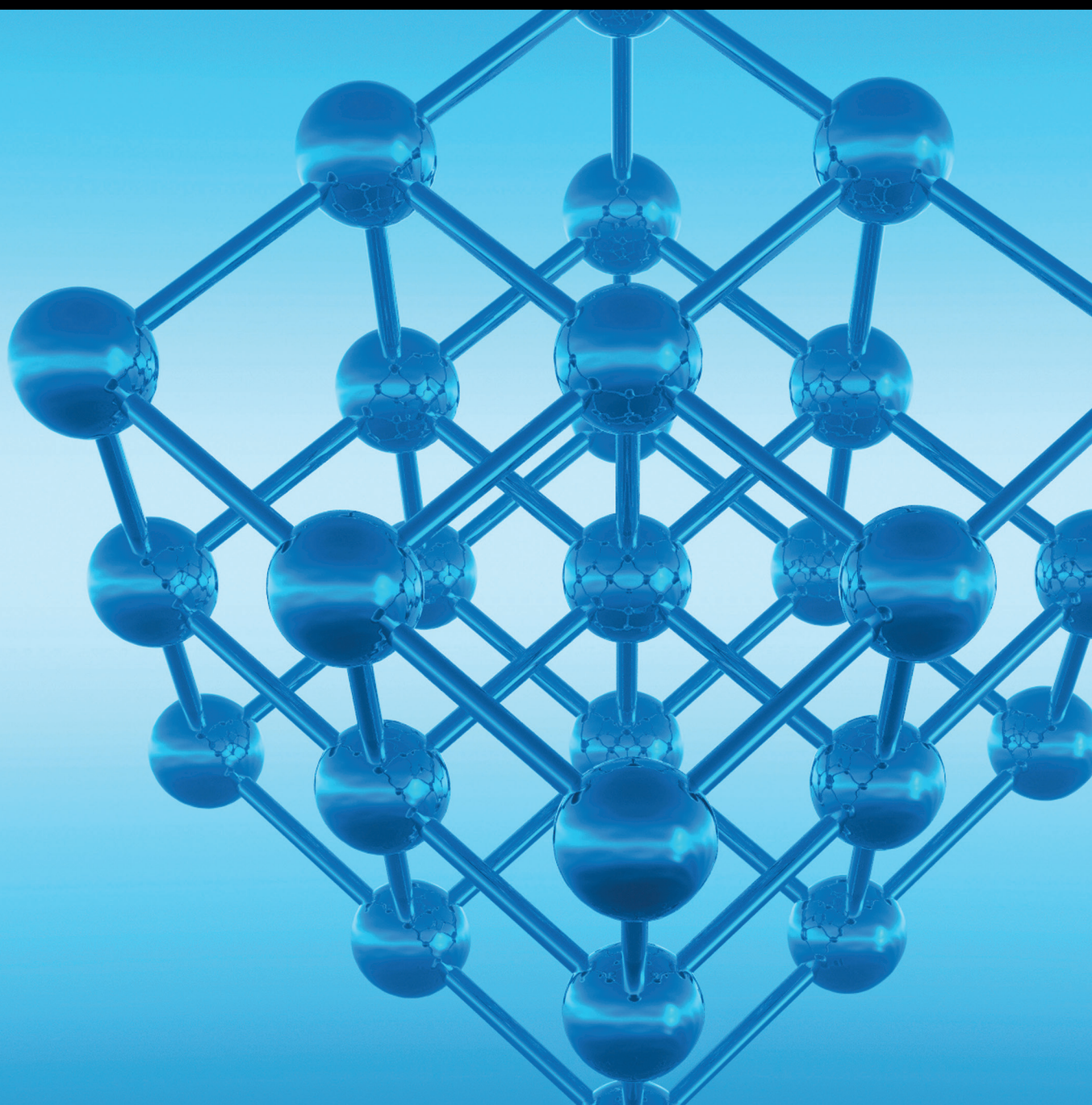


Advances in Condensed Matter Physics

Condensed Matter in Energy, Environment, and Beyond

Lead Guest Editor: Hong Fang

Guest Editors: Jiajie Zhu and Jun-Cheng Zhang





**Condensed Matter in Energy, Environment,
and Beyond**

Advances in Condensed Matter Physics

Condensed Matter in Energy, Environment, and Beyond

Lead Guest Editor: Hong Fang

Guest Editors: Jiajie Zhu and Jun-Cheng Zhang



Copyright © 2019 Hindawi. All rights reserved.

This is a special issue published in “Advances in Condensed Matter Physics.” All articles are open access articles distributed under the Creative Commons Attribution License, which permits unrestricted use, distribution, and reproduction in any medium, provided the original work is properly cited.

Editorial Board

Ward Beyermann, USA
Golam M. Bhuiyan, Bangladesh
Luis L. Bonilla, Spain
Ashok Chatterjee, India
Ram N. P. Choudhary, India
Oleg Derzhko, Ukraine
Raouf El-Mallawany, Egypt

Gayanath Fernando, USA
Yuri Galperin, Norway
Prasenjit Guptasarma, USA
Da-Ren Hang, Taiwan
Jan A. Jung, Canada
Leonid Pryadko, USA
Charles Rosenblatt, USA

Sergei Sergeenkov, Brazil
Sergio E. Ulloa, USA
Markus R. Wagner, Germany
Gary Wysin, USA
Kiyokazu Yasuda, Japan
Fajun Zhang, Germany
Jiandi Zhang, USA

Contents

Condensed Matter in Energy, Environment, and Beyond

Hong Fang , Jiajie Zhu, and Juncheng Zhang

Editorial (2 pages), Article ID 1692143, Volume 2019 (2019)

Physical Structure Induced Hydrophobicity Analyzed from Electrospinning and Coating Polyvinyl Butyral Films

Shuo Chen, Guo-Sai Liu, Hong-Wei He , Cheng-Feng Zhou , Xu Yan , and Jun-Cheng Zhang

Research Article (5 pages), Article ID 6179456, Volume 2019 (2019)

Light Sum Accumulation in ZnSe Crystals at X-Ray Excitation

V. Ya. Degoda, G. P. Podust, and M. Alizadeh 

Research Article (9 pages), Article ID 8784109, Volume 2019 (2019)

Thickness Induced Line-Defect Reconfigurations in Thin Nematic Cell

M. Ambrožič  and S. Kralj 

Research Article (7 pages), Article ID 4256526, Volume 2019 (2019)

Influence of Gold Nanoparticles on the Luminescence of an Acrylated Isocyanonaphthalene Derivative

J. Burunkova, S. Keki, A. Veniaminov , M. Nagy , L. Daroczi , and S. Kokenyesi

Research Article (5 pages), Article ID 8084659, Volume 2019 (2019)

Effect of Deposition Time on the Optoelectronics Properties of PbS Thin Films Obtained by Microwave-Assisted Chemical Bath Deposition

Enue Barrios-Salgado , Y. Rodríguez-Lazcano , Juan Pablo Pérez-Orozco, J. Colin, P. Altuzar, J. Campos , and David Quesada

Research Article (8 pages), Article ID 5960587, Volume 2019 (2019)

Effect of Adding Co on Crystallization Behavior and Magnetoimpedance Effect of Amorphous/Nanocrystalline FeCuNbSiB Alloy Strips

Da-guo Jiang, Yuan-xiu Ye, and Bin Guo 

Research Article (6 pages), Article ID 2710396, Volume 2019 (2019)

Mechanical Characterization of Reduced Graphene Oxide Using AFM

Alem Teklu , Canyon Barry, Matthew Palumbo, Collin Weiwadel, Narayanan Kuthirummal, and Jason Flagg

Research Article (13 pages), Article ID 8713965, Volume 2019 (2019)

Influence of Crystallization Time on Energy-Storage Density and Efficiency of Lead-Free

$\text{Bi}_{0.5}(\text{Na}_{0.8}\text{K}_{0.2})_{0.5}\text{TiO}_3$ Thin Films

Ngo Duc Quan , Tran Quoc Toan, and Vu Ngoc Hung

Research Article (8 pages), Article ID 4949365, Volume 2019 (2019)

Improved Electrochemical Performance of $\text{Li}_{1.25}\text{Ni}_{0.2}\text{Co}_{0.333}\text{Fe}_{0.133}\text{Mn}_{0.333}\text{O}_2$ Cathode Material Synthesized by the Polyvinyl Alcohol Auxiliary Sol-Gel Process for Lithium-Ion Batteries

He Wang , Mingning Chang, Yonglei Zheng, Ningning Li, Siheng Chen, Yong Wan, Feng Yuan, Weiquan Shao, and Sheng Xu 

Research Article (7 pages), Article ID 1217639, Volume 2018 (2019)

Performance Investigation of a Silicon Photovoltaic Module under the Influence of a Magnetic Field

Dioari Ulrich Combari, Emmanuel Wendsongré Ramde , Idrissa Sourabie, Martial Zoungrana,
Issa Zerbo , and Dieudonné Joseph Bathiebo

Research Article (8 pages), Article ID 6096901, Volume 2018 (2019)

Editorial

Condensed Matter in Energy, Environment, and Beyond

Hong Fang ,¹ Jiajie Zhu,² and Juncheng Zhang³

¹Department of Physics, Virginia Commonwealth University, Richmond, VA, USA

²Department of Materials Science, Shenzhen University, Shenzhen, China

³Department of Physics, Qingdao University, Qingdao, China

Correspondence should be addressed to Hong Fang; hfangtom@gmail.com

Received 7 April 2019; Accepted 7 April 2019; Published 2 May 2019

Copyright © 2019 Hong Fang et al. This is an open access article distributed under the Creative Commons Attribution License, which permits unrestricted use, distribution, and reproduction in any medium, provided the original work is properly cited.

One of the most important themes of today's scientific research is the design and development of energetic and environmental materials, as well as the understanding of their physics and chemistry. Condensed matters, such as organic-inorganic hybrid perovskites, superionic conductors, metal-organic frameworks, covalent organic frameworks, black phosphorus, penta-graphene, and mechanoluminescent materials, have attracted tremendous interest. In this special issue, we intend to cover recent theoretical and experimental progress in the condensed matter materials that have applications related to energy and environment, but also with a much broader touch on other important functionality. The focus will be on the physical properties of novel condensed matter materials in terms of their applications, for example, in solar cells, rechargeable batteries based on metal ions, greenhouse gas sequestration and conversion, gas sensory and separation, photovoltaics, photoluminescence, and mechanical sensors. The purpose of this special issue is to present the recent progress in these exciting fields. A brief summary of all accepted papers is provided below.

In the paper by S. Chen et al., they have reported the controlling physical surface structure of polyvinyl butyral (PVB) films by different film-forming methods, spin-coating, bar-coating, and electrospinning. The wettability of these PVB films was examined, and the surface morphologies and roughness were investigated. The results indicated that coating PVB films were hydrophilic, while electrospun films were hydrophobic. The physical surface structure was the key role on the interesting transition of their surface wettability. These results may help to find the way to control the PVB film surface wettability and then guide for applications.

The paper by G. P. Podust et al. presents their results of the dose dependencies of the light sum accumulation in ZnSe

single crystals at a different X-ray excitation at 85 K. The values of light sum accumulation at different deep traps were determined from the thermally stimulated luminescence and conductivity curves. It was confirmed that the accumulated light sum is uniquely determined by the dose of radiation only, that is, the product of the intensity of excitation by the time of X-ray exposure.

The work by M. Ambrožič and S. Kralj studied the impact of the cell thickness on configurations of line disclinations within a plane-parallel nematic cell. The Lebwohl-Lasher semimicroscopic approach was used and (meta)stable nematic configurations were calculated using Brownian molecular dynamics. Defect patterns were enforced topologically via boundary conditions. The resulting structures exhibit line defects which either connect the facing plates or remain confined within the layers near confining plates. The first structure is stable in relatively thin cells and the latter one in thick cells. It is demonstrated that "history" of samples could have strong impact on resulting nematic configurations.

The paper by J. Burunkova et al. reported dodecanethiol-functionalized gold nanoparticles that were incorporated into the polymer matrix of diurethane-methacrylate monomer mixture in the presence of SiO₂ nanoparticles (8 wt%) and a new reactive organic luminescent material ACAIN (1-N-(2-acryloyloxy-3-chloroprop-1-yl)-amino-5-isocyanonaphthalene, 1 wt%). It was shown that the addition of SiO₂ nanoparticles enhances the fluorescent intensity of ACAIN by 1.5 times in the 450-550 nm spectral range. Furthermore, an additional fluorescence enhancement up to 4.5 times was observed when Au nanoparticles were added to the nanocomposite in a rather low (0.12 wt%) concentration.

Hong Fang
Jijie Zhu
Juncheng Zhang

The paper by E. Barrios-Salgado et al. reported PbS thin films with thickness between 100 and 150 nm which were grown for the first time by microwave-assisted chemical bath deposition in a commercial automated system with deposition times not exceeding 5 min. X-ray diffraction analysis shows that the thin films have cubic rock salt type structure with good crystallinity. The grain size increased from 18 to 20 nm, as the deposition time increased. Energy dispersive X-ray results confirm that the films are stoichiometric. Optical measurements show that thin films have relatively high absorption coefficients between 104 and 105 cm⁻¹ in the visible range. In addition, the films exhibit a direct gap, within the energy range from 1.0 to 1.35 eV. The electrical properties, such as conductivity, the Seebeck coefficient, carrier concentration, and carrier mobility, are discussed.

The paper by D. Jiang et al. studied the effect of adding Co on crystallization behavior and magnetoimpedance effect of amorphous/nanocrystalline FeCuNbSiB alloy strips.

A. Teklu et al. studied stiffness, hardness, and the reduced Young's modulus of reduced graphene oxide by using nanoindentation coupled with atomic force microscopy.

The paper by N. D. Quan et al. reported the synthesis of lead-free Bi_{0.5}(Na_{0.80}K_{0.20})_{0.5}TiO₃ (BNKT) ferroelectric films on Pt/Ti/SiO₂/Si substrates via chemical solution deposition. The influence of crystallization time on the microstructures and ferroelectric and energy-storage properties of the films was investigated in detail. The obtained results indicate that the BNKT films have application potentials in advanced capacitors.

The paper by H. Wang et al. reported the preparation of a lithium-rich manganese-based cathode material, Li_{1.25}Ni_{0.2}Co_{0.333}Fe_{0.133}Mn_{0.333}O₂, using a polyvinyl alcohol (PVA-) auxiliary sol-gel process using MnO₂ as a template. The effect of the PVA content on the electrochemical properties and morphology of the material was investigated.

D. U. Combari et al. conducted an experiment and investigated the performance of a silicon photovoltaic module subjected to a magnetic field. The current-voltage and power-voltage characteristics were plotted in the same axis system and allowed us to find, as a function of the magnetic field, the electrical parameters of the photovoltaic module such as maximum electric power, fill factor, conversion efficiency, and charge resistance at the maximum power point. These electrical parameters were then used to calculate the series and shunt resistances of the equivalent circuit of the photovoltaic module. The results have shown that the efficiency of a solar module is affected by the presence of magnetic fields.

Conflicts of Interest

The authors declare that they have no conflict of interest.

Acknowledgments

We would like to express our gratitude to all authors who made this special issue possible. We hope this collection of articles will be useful to the scientific community.

Research Article

Physical Structure Induced Hydrophobicity Analyzed from Electrospinning and Coating Polyvinyl Butyral Films

Shuo Chen,¹ Guo-Sai Liu,¹ Hong-Wei He ,¹ Cheng-Feng Zhou ,²
Xu Yan ,^{1,3,4} and Jun-Cheng Zhang⁴

¹Industrial Research Institute of Nonwovens and Technical Textiles, College of Textiles and Clothing, Qingdao University, Qingdao 266071, China

²State Key Laboratory of Bio-Fibers and Eco-Textiles, Qingdao University, Qingdao 266071, China

³Collaborative Innovation Center for Eco-Textiles of Shandong Province, Qingdao University, Qingdao 266071, China

⁴Collaborative Innovation Center for Nanomaterials and Optoelectronic Devices, College of Physics, Qingdao University, Qingdao 266071, China

Correspondence should be addressed to Cheng-Feng Zhou; chengfengzhou@qdu.edu.cn and Xu Yan; yanxu-925@163.com

Received 5 November 2018; Accepted 5 March 2019; Published 1 April 2019

Academic Editor: Golam M. Bhuiyan

Copyright © 2019 Shuo Chen et al. This is an open access article distributed under the Creative Commons Attribution License, which permits unrestricted use, distribution, and reproduction in any medium, provided the original work is properly cited.

Surface wettability of a film plays a critical role in its practical applications. To control the surface wettability, modification on the physical surface structures has been a useful method. In this paper, we reported the controlling physical surface structure of polyvinyl butyral (PVB) films by different film-forming methods, spin-coating, bar-coating, and electrospinning. The wettability of these PVB films was examined, and the surface morphologies and roughness were investigated. The results indicated that coating PVB films were hydrophilic, while electrospun films were hydrophobic. The physical surface structure was the key role on the interesting transition of their surface wettability. Theoretical analyses on these results found that the coating PVB films showed different mechanism with electrospun ones. These results may help to find the way to control the PVB film surface wettability and then guide for applications.

1. Introduction

The wetting behavior of solid surfaces by a liquid as a very important aspect of surface properties has been a focused interest for a long time [1–4] and has shown a wide variety of practical applications in various fields, such as protecting clothes [5], medical care [6–8], and filtration [9]. Consequently, great efforts have been made to find the way to control the surface wettability [10–13].

According to the term biomimetic, “lotus leaves effect” indicates that the cooperation of hierarchical structures and other specific components on the natural surfaces results in the desired wettability [1–3, 14]. Moreover, from the theoretical view, such as Young’s equation [15], Wenzel model [16], and Cassie model [17], the surface roughness plays a critical role in surface wettability [18–21]. Furthermore, the rough surface is extended to porous surfaces and even micro-nano structures [22–24]. To achieve these structures,

especially in film structures, several methods are developed such as solution cast and electrospinning [5–10, 19, 21].

Among various materials, polyvinyl butyral (PVB), which is characterized by high adhesion to glass, excellent mechanical strength, excellent biocompatibility, nontoxicity, and good solubility in alcohol, has been applied to many fields such as an adhesive interlayer in safety glass, wound dressing, and coating film [5–7, 10, 11]. Moreover, PVB shows both hydrophobic and hydrophilic properties due to its chemical structure with both vinyl butyral group and vinyl hydroxyl group [10, 25]. And previous study has suggested that electrospun PVB nanofibrous structures and patterns showed larger water contact angle (WCA) than that of the solution casting film [7, 10, 11]. However, these works most focus on the electrospun PVB meshes and rarely discuss the comparison of the structures between the different methods.

In this paper, we focused on the comparison of PVB films made by several methods, spin-coating, bar-coating, and

TABLE 1: The SWCA of the prepared PVB films by different methods.

Methods		SWCA (°)	SWCA (°)	SWCA (°)	ASWCA (°)
	Concentrations/parameters	8 wt%	10 wt%	12 wt%	
Spin-coating	250 r/s	77.767	78.800	78.900	78.593
	300 r/s	74.300	82.600	79.933	
	350 r/s	76.033	82.733	76.267	
Bar-coating	6 μm	86.438	83.297	84.303	83.067
	8 μm	81.255	82.626	81.437	
	10 μm	81.093	81.360	85.796	
Positive electrospinning	15 cm	135.833	130.833	131.933	132.404
	20 cm	132.167	133.600	129.700	
	25 cm	131.667	135.400	130.500	
Negative electrospinning	15 cm	131.033	135.733	130.867	131.615
	20 cm	128.633	135.100	133.367	
	25 cm	128.300	133.233	128.267	

electrospinning. The WCAs on these films were measured and the morphologies and surface roughness of them were also examined. By analyzing these results, we want to find a way to control the surface wettability.

2. Materials and Methods

2.1. Materials. Polyvinyl butyral (PVB) (MW~100,000, Sino-pharm Chemical Reagent Co., Ltd., China) was dissolved in ethyl alcohol (analytical reagent, 99%) at 8 wt%, 10 wt%, and 12 wt% firstly and then stirred for 2 h at room temperature.

2.2. Preparation of the Films. The PVB/alcohol solutions were used to produce films by spin-coating, bar-coating, and electrospinning, respectively. During spin-coating process, PVB/alcohol solutions were dripped onto cover slips (20 mm×20 mm) with 5 μl and then set on the spin-coater (KW-4A, Institute of Microelectronics of the Chinese Academy of Sciences). The spinning velocities were selected at 250 r/s, 300 r/s, and 350 r/s, and spinning time was set at 30 seconds. In bar-coating process, 10 μl PVB/alcohol solutions were dripped onto slide glasses (76 mm×26 mm), and the bars were selected with 6 μm , 8 μm , and 10 μm film thickness. For electrospun meshes, both positive electrospinning and negative electrospinning were processed. PVB/alcohol solutions were firstly loaded into syringes (5 ml) and then set on the electrospinning apparatus (DW-P303-IACF5 (positive), DW-N303-IACDF0 (negative), Dongwen, China), the electrospinning voltage was set at 15 kV and -15 kV, and the distances were selected at 15 cm, 20 cm, and 25 cm.

2.3. Characterization. The static water contact angles (SWCA) of the prepared films were examined by an optical tensiometer (Attension Theta, Biolin Scientific, Germany) with a 2 μL water droplet for three sites at room temperature and analysis was performed by fitting drops with a Young-Laplace formula using the Theta software. The surface roughness was also measured by optical tensiometer with 3D surface roughness module. The morphologies of the films were examined by a scanning electron microscope (SEM,

Phenom ProX, Phenom Scientific Instruments Co., Ltd., China) at 10 kV, and all samples were coated with gold for 30 s before analysis. The fiber diameters were analyzed by Nano Measurer software. The Fourier transform infrared spectroscopy (FTIR) spectrums were measured by a Thermo Scientific Nicolet iN10 spectrometer.

3. Results and Discussion

To ensure the wettability of the prepared PVB films, SWCA were measured and shown in Table 1. One can find that the spin-coating and bar-coating PVB films showed hydrophilicity with SWCA $<90^\circ$, while the electrospun films showed hydrophobicity with SWCA $>90^\circ$, which agreed with the previous study [7, 10, 11]. Moreover, the bar-coating PVB films had larger SWCA than spin-coating ones generally. The SWCA of electrospun PVB films with positive electrospinning process is mostly larger than that of negative electrospinning. Nevertheless, as seen from Figure 1, the prepared PVB films showed similar absorption peaks, which indicated that these films had same chemical structures. It is interesting that the same material showed different wettability for its different film-forming methods.

To understand the interesting PVB film wettability, we firstly examined the morphologies of selected PVB films (10% concentration) with spin-coating 250 r/s, bar-coating 6 μm , and positive and negative electrospinning with distance of 15 cm. As shown in Figure 2(a), the spin-coating PVB film showed a macroscopically relative smooth surface with SWCA 78.8° ; the bar-coating film also had a smooth surface with SWCA 83.3° (Figure 2(b)). Both smooth films showed hydrophilicity. Meanwhile, both the positive and negative electrospun PVB films showed porous rough surfaces, as can be found in Figures 2(c) and 2(d), and the SWCA were 130.8° and 135.7° , respectively. Both the porous rough electrospun films showed hydrophobicity. According to these results, it seems that the surface roughness determined the wettability of the films.

For further investigation, we examined the roughness of the selected films, as shown in Figure 3. It is strange

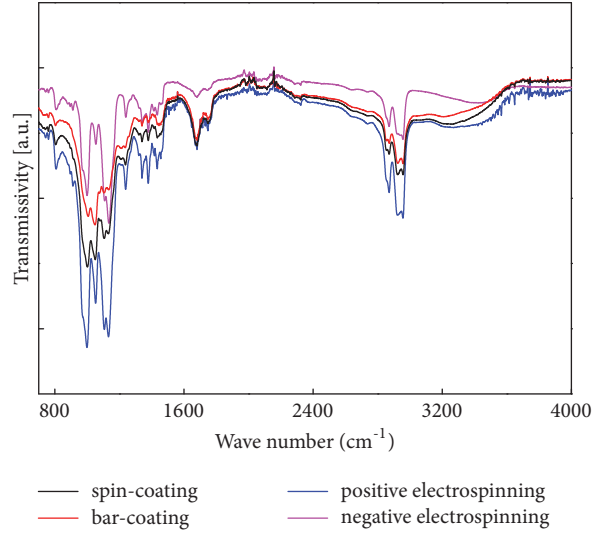
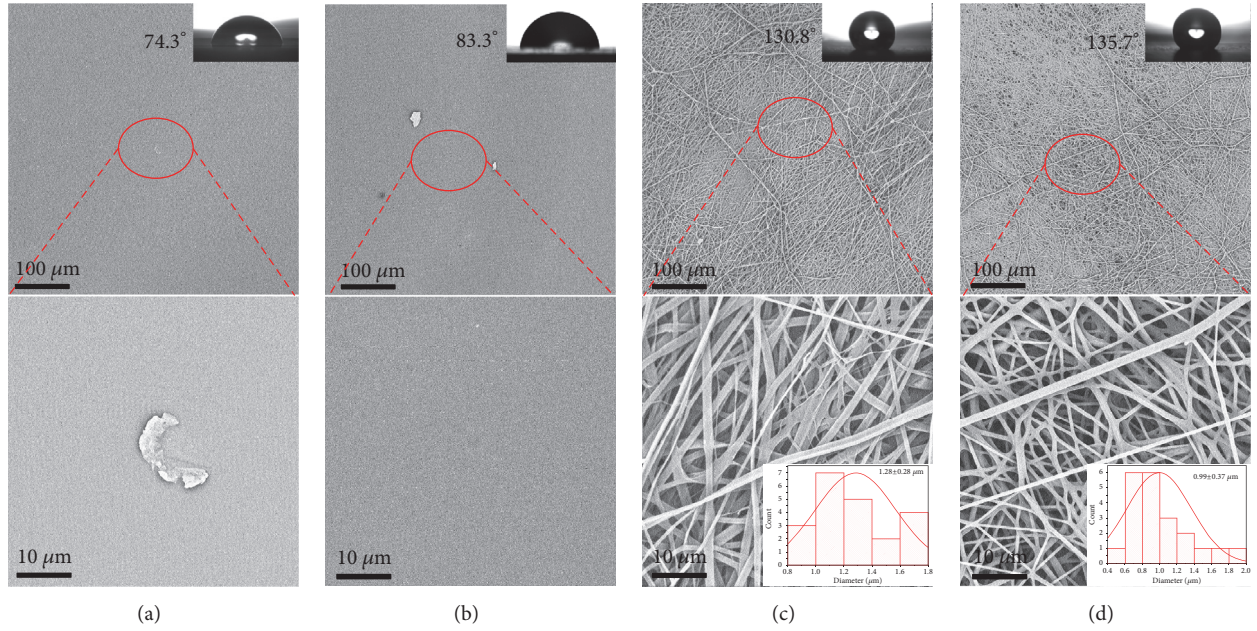


FIGURE 1: FTIR spectra of PVB films made by different methods.

FIGURE 2: SEM images of the PVB films made by spin-coating 250 r/s (a), bar-coating 6 μm (b), positive electrospinning 15 cm (c), and negative electrospinning 15 cm (d). The upper inset images showed the water droplet onto these films, and the lower inset images showed the electrospun fiber diameter distributions.

that the macroscopical smooth surfaces shown in Figure 2 have higher roughness than the electrospun films. In our opinion, this case may result from the different surface structures of the films that coating films showed relative dense surface structure, while electrospun films had porous surface structure, as can be seen in Figure 2. For the hydrophobic coating PVB films [seen in Figures 3(a) and 3(b)], bar-coating ones showed higher roughness than the spin-coating ones with $r=3.715>2.351$, where r is the factor of the surface roughness. According to the Wenzel model [1, 22],

$$\cos \theta' = r \cos \theta_c, \quad (1)$$

where $\theta_c < 90^\circ$, the larger the factor of roughness r is, the smaller θ' will get, and the increasing roughness will make the film more hydrophilic. The case in coating PVB films followed the Wenzel model; consequently the bar-coating films with more roughness showed smaller SWCA than spin-coating ones. Meanwhile, for the electrospun films, the porous and micro-nano surface structures made the Wenzel model not work. As suggested in Figures 3(c) and 3(d) and Figures 2(c) and 2(d), the positive electrospun PVB film with more roughness ($r=1.106$) had smaller SWCA (130.8°) than that of negative electrospinning PVB film ($r=1.076$, SWCA 135.7°). In this case, the Cassie model, which gives a composite state

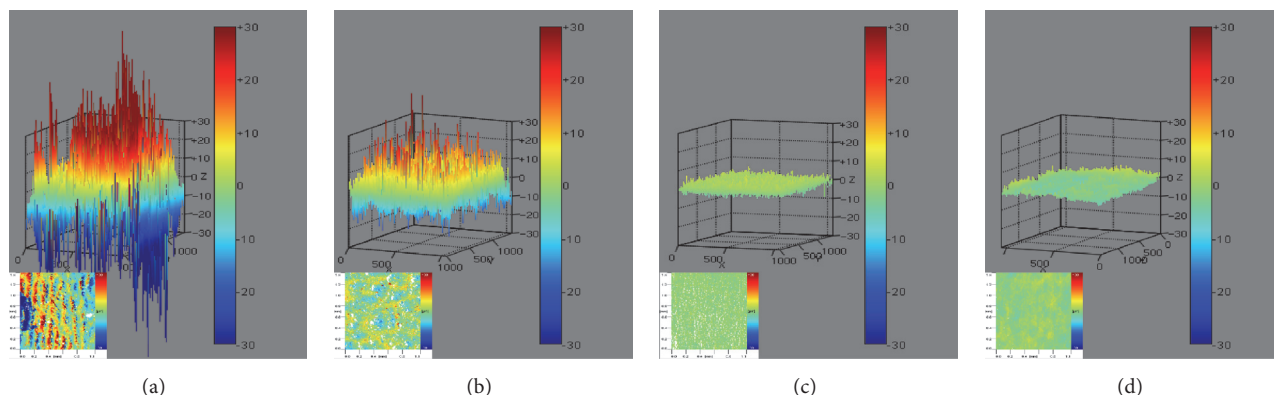


FIGURE 3: 3D surface roughness of the prepared PVB films under spin-coating 250 r/s (a), bar-coating 6 μm (b), positive electrospinning 15 cm (c), and negative electrospinning 15 cm (d). The inset images showed the 2D surface roughness of these films.

that liquids are assumed to only contact the solid through the top of the asperities and air pockets are assumed to be trapped underneath the liquid [1, 22], may be considered; the function can be expressed as

$$\cos \theta' = -1 + f_s (1 + r \cos \theta_c), \quad (2)$$

where f_s are the area fractions of the solid on the surface. From (2), one can find that the smaller f_s is, the more hydrophobicity will be obtained. Specifically to the electrospun PVB films, the smaller the fiber diameter is, the smaller f_s will be achieved, and then higher hydrophobicity will be shown [5, 7, 10, 11]. From lower inset images in Figure 2, we can obviously find that negative electrospun PVB fibers had smaller diameters and less uniform and consequently exhibited higher SWCA.

4. Conclusions

In conclusion, we have prepared several kinds of PVB films through spin-coating, bar-coating, and electrospinning. The FTIR spectra suggested that these films have the same chemical structures. Meanwhile, these films showed different wettability that coating films were hydrophilicity and electrospun films were hydrophobicity. SEM images indicated that the different films showed different physical surface structures, which may introduce the different wettability. Further investigation on the surface roughness confirmed that the wettability of coating films obeyed the Wenzel model, while the electrospun films agreed with the Cassie model. These results may help to understand the mechanism of the PVB films and then guide for its practical application.

Data Availability

The data used to support the findings of this study are available from the corresponding author upon request.

Conflicts of Interest

The authors declare that there are no conflicts of interest regarding the publication of this paper.

Acknowledgments

This work was supported by the National Natural Science Foundation of China (51703102, 51373082, and 51673103), the Shandong Provincial Natural Science Foundation, China (ZR2016EMB09 and ZR2017BEM045), and the Qingdao Postdoctoral Applied Research Project.

References

- [1] K. Liu, X. Yao, and L. Jiang, "Recent developments in bio-inspired special wettability," *Chemical Society Reviews*, vol. 39, no. 8, p. 3240, 2010.
- [2] T. L. Sun, L. Feng, X. F. Gao, and L. Jiang, "Bioinspired surfaces with special wettability," *Accounts of Chemical Research*, vol. 38, no. 8, pp. 644–652, 2005.
- [3] L. Feng, S. Li, Y. Li et al., "Super-hydrophobic surfaces: from natural to artificial," *Advanced Materials*, vol. 14, no. 24, pp. 1857–1860, 2002.
- [4] J. C. Zhang, C. Pan, Y. F. Zhu et al., "Achieving thermo-mechano-opto-responsive bitemporal colorful luminescence via multiplexing of dual lanthanides in piezoelectric particles and its multidimensional anticounterfeiting," *Advanced Materials*, vol. 30, Article ID 1804644, 2018.
- [5] M. N. Liu, X. Yan, and M. H. You, "Reversible photochromic nanofibrous membranes with excellent water/windproof and breathable performance," *Journal of Applied Polymer Science*, vol. 135, no. 23, Article ID 46342, 2018.
- [6] H. Xu, H. Li, and J. Chang, "Controlled drug release from a polymer matrix by patterned electrospun nanofibers with controllable hydrophobicity," *Journal of Materials Chemistry B*, vol. 1, no. 33, p. 4182, 2013.
- [7] G. S. Liu, X. Yan, F. F. Yan et al., "In situ electrospinning iodine-based fibrous meshes for antibacterial wound dressing," *Nanoscale Research Letters*, vol. 13, Article ID 309, 2018.
- [8] J. Zhang, S. Li, D. Ju et al., "Flexible inorganic core-shell nanofibers endowed with tunable multicolor up conversion fluorescence for simultaneous monitoring dual drug delivery," *Chemical Engineering Journal*, vol. 349, pp. 554–561, 2018.
- [9] N. Wang, Y. Si, J. Yu, H. Fong, and B. Ding, "Nano-fiber/net structured electrospun PVA membrane: effects of formic acid as solvent and crosslinking agent on solution properties and

- membrane morphological structures,” *Materials and Corrosion*, vol. 120, pp. 135–143, 2017.
- [10] X. Yan, M. H. You, T. Lou et al., “Colorful hydrophobic poly(vinyl butyral)/cationic dye fibrous membranes via a colored solution electrospinning process,” *Nanoscale Research Letters*, vol. 11, no. 540, 2016.
- [11] H. Wu, R. Zhang, Y. Sun et al., “Biomimetic nanofiber patterns with controlled wettability,” *Soft Matter*, vol. 4, no. 12, p. 2429, 2008.
- [12] S. S. Liu, C. H. Zhang, J. G. He et al., “Wetting state transition on hydrophilic microscale rough surface,” *Acta Physica Sinica*, vol. 62, no. 20, Article ID 206201, 2013.
- [13] J. Yang, Y. Pu, D. Miao, and X. Ning, “Fabrication of durably superhydrophobic cotton fabrics by atmospheric pressure plasma treatment with a siloxane precursor,” *Polymers*, vol. 10, Article ID 460, 2018.
- [14] J. B. Boreyko and C. H. Chen, “Restoring superhydrophobicity of lotus leaves with vibration-induced dewetting,” *Physical Review Letters*, vol. 103, no. 17, Article ID 174502, 2009.
- [15] T. Young, “An essay on the cohesion of fluids,” *Philosophical Transactions of the Royal Society London*, vol. 95, pp. 65–87, 1805.
- [16] R. N. Wenzel, “Resistance of solid surfaces to wetting by water,” *Industrial and Engineering Chemistry*, vol. 28, no. 8, pp. 988–994, 1936.
- [17] A. B. D. Cassie and S. Baxter, “Wettability of porous surfaces,” *Transactions of the Faraday Society*, vol. 40, pp. 546–551, 1944.
- [18] D. Quéré, “Wetting and roughness,” *Annual Review of Materials Research*, vol. 38, pp. 71–99, 2008.
- [19] H. Ems and S. Ndao, “Microstructure-alone induced transition from hydrophilic to hydrophobic wetting state on silicon,” *Applied Surface Science*, vol. 339, pp. 137–143, 2015.
- [20] M. Khorasani, H. Mirzadeh, and Z. Kermani, “Wettability of porous polydimethylsiloxane surface: morphology study,” *Applied Surface Science*, vol. 242, no. 3–4, pp. 339–345, 2005.
- [21] Y. Zhang, X. Chen, F. Liu et al., “Enhanced coffee-ring effect via substrate roughness in evaporation of colloidal droplets,” *Advances in Condensed Matter Physics*, vol. 2018, Article ID 9795654, 9 pages, 2018.
- [22] K. Lum, D. Chandler, and J. D. Weeks, “Hydrophobicity at small and large length scales,” *The Journal of Physical Chemistry B*, vol. 103, no. 22, pp. 4570–4577, 1999.
- [23] S. Rajamani, T. M. Truskett, and S. Garde, “Hydrophobic hydration from small to large lengthscales: Understanding and manipulating the crossover,” *Proceedings of the National Academy of Sciences of the United States of America*, vol. 102, no. 27, pp. 9475–9480, 2005.
- [24] X. B. Li and Y. Liu, “Wetting mechanisms and models on solid surfaces,” *Journal of Functional Materials*, vol. 38, pp. 3919–3924, 2007 (Chinese).
- [25] W. Chen, D. J. David, W. J. MacKnight, and F. E. Karasz, “Miscibility and Phase Behavior in Blends of Poly(vinyl butyral) and Poly(methyl methacrylate),” *Macromolecules*, vol. 34, no. 12, pp. 4277–4284, 2001.

Research Article

Light Sum Accumulation in ZnSe Crystals at X-Ray Excitation

V. Ya. Degoda, G. P. Podust, and M. Alizadeh 

Taras Shevchenko National University of Kyiv, faculty of Physics, 60 Volodymyrs'ka Street, Kyiv 01033, Ukraine

Correspondence should be addressed to M. Alizadeh; trefoilsymbol@gmail.com

Received 25 October 2018; Accepted 3 February 2019; Published 1 April 2019

Guest Editor: Hong Fang

Copyright © 2019 V. Ya. Degoda et al. This is an open access article distributed under the Creative Commons Attribution License, which permits unrestricted use, distribution, and reproduction in any medium, provided the original work is properly cited.

This paper presents the results of the dose dependencies of the light sum accumulation in ZnSe single crystals at a different X-ray excitation at 85 K. The values of light sum accumulation at different deep traps were determined from the thermally stimulated luminescence and conductivity curves. It was confirmed that the accumulated light sum is uniquely determined by the dose of radiation only, that is, the product of the intensity of excitation by the time of X-ray exposure. The same result is also given by the theoretical consideration of the kinetics of the light sum accumulation on deep traps for a multicenter model of crystal phosphors.

1. Introduction

Zinc selenide (ZnSe) belongs to wide-bandgap materials of $A^{II}B^{VI}$ type and is a well-studied material [1–3]. ZnSe is widely used in the creation of semiconductor electronic devices and information display systems [4]. Over the last decade, another promising direction for ZnSe application has been developed: as detectors of an indirect ionizing radiation [4–6] and direct high-energy conversion of radiation into electric current [7]. Relatively high value of the effective atomic number $Z_{ef} = 32$ and a band gap width $E_g = 2.7$ eV (at 300 K), as well as the technology for growing high-quality single crystals with low concentrations of uncontrolled impurities and high material resistivity at $\sim 10^{10} - 10^{14}$ Ohm cm make zinc selenide a promising material for creating X-ray semiconductor detectors that do not require cooling [7]. It should be noted that the resistivity of $\sim 10^{14}$ Ohm cm in ZnSe crystals means that the concentration of free electrons in the conduction band does not exceed 10^3 cm⁻³ at room temperature.

The kinetics of luminescence and conductivity in the crystal phosphors substantially depend not only on the concentration of various luminescence centers but also on the concentrations of various traps. Therefore, when studying the kinetics of luminescence and conductivity, it is necessary to know the kinetics of accumulation of the charge carriers on deep traps and the kinetics of accumulation of recharge of the luminescence centers. The classical kinetic theories

of photoluminescence [8–10] and photoconductivity [11–13], which use the simplest model of crystal phosphors with one trap and one recombination center, show that the value of the maximum accumulated light sum intensity on the trap $n_{\infty} \sim \sqrt{I_{ex}}$ (where I_{ex} – excitation intensity). Since real crystals, as a rule, contain a set of traps and several luminescence centers, it is necessary to verify this ratio experimentally.

Thus, there arises a need for a comprehensive study of the luminescent and electrical properties of ZnSe. This paper is devoted to the study of the features of the light sum accumulation in the ZnSe single crystals at different intensities and duration of X-ray excitation in order to verify the influence of the excitation intensity on the value of the maximum accumulated light sum. For comparison, it is also necessary to obtain a theoretical dependence for the light sum accumulation on deep traps for a multicenter model of crystal phosphors.

1.1. Experimental Method. A comprehensive experimental study of X-ray conductivity (XRC), X-ray luminescence (XRL), phosphorescence (Ph), and conduction current relaxation (CCR) was carried out; however the main focus was on the studies of thermally stimulated conductivity (TSC) and luminescence (TSL) and their dose dependencies at different intensities of X-ray excitation. ZnSe crystals were grown from a prepurified initial charge and were not specifically doped during their growth. For the study purpose, the samples were made in the form of parallelepipeds with dimensions: 18×9×2

mm^3 . By the method of thermo-EMF, it was found that the samples had n-type conductivity. It is also known [14] that the photoconductivity in ZnSe is due to free electrons.

To examine conductivity, the electrical contacts in the form of two parallel strips of $1 \times 5 \text{ mm}^2$ (at a distance of 5 mm from each other) were sprayed on the very surface of the single crystal samples. The conductors were then soldered to the contacts. In this work, we used such a contact geometry, in which the sprayed electrodes were located in the central part of the most polished surface of the sample. A constant stabilized voltage from 0 to 1000 V was applied to one electrode, and the other was connected to a nanoammeter to record the current. The magnitude of the conduction current was measured with an accuracy of 1% for the currents from 10 pA to 1 mA. For all values of the conduction current, the following condition was satisfied: the input impedance of the nanoammeter was by several orders of magnitude smaller than the electrical resistance of the ZnSe sample. The nanoammeter is a part of a specially designed measuring unit of I – V curve, which allows choosing different modes of voltage variations: manual, stepwise, and linear with various speeds.

To study the TSL and TSC, the sample was placed in a cryostat and was secured with a large polished surface (opposite to the surface with contacts) to a polished copper block to ensure good thermal contact of the sample with the cryostat's copper substrate. It is necessary to conduct temperature studies, as it ensures the minimum temperature gradient in the sample. Previously it was found that the maximum temperature difference in various parts of the sample does not exceed 0.3 K. During the studies, the sample was in a vacuum ($p < 1 \text{ Pa}$). The sample surface between the electrical contacts was irradiated with the integral radiation of the BHV-7 X-ray tube (Re, 20 kV, 5 mA ($I_{1X} = 0.13 \text{ mW/cm}^2$) or 25 mA ($I_{2X} = 0.64 \text{ mW/cm}^2$), $L=130 \text{ mm}$) through a beryllium window in a cryostat. The intensity of the X-ray excitation was changed by varying the anode current of the X-ray tube at a constant voltage. The shape of the emission spectrum of the X-ray tube remained unchanged, and the intensity was proportional to the magnitude of the anode current of the X-ray tube.

The luminescence spectra were recorded at 8, 85, and 295 K. The dose dependencies of TSL and TSC were measured after X-ray excitation for a fixed time τ_X at a temperature of 85 K. After irradiation and relaxation of phosphorescence and conduction current (about 10 minutes), the sample was heated to 450 K using an electric furnace of 800 W embedded in the cryostat. The heating rate of the sample was $0.40 \pm 0.02 \text{ K/s}$. The cooling was made by liquid nitrogen. The radiation dose was changed by altering the time of exposure τ_X at a constant intensity of the X-ray tube, using two operating modes: 20 kV, 25 mA, and 20 kV, 5 mA.

Two channels were used to record the luminescence: integral and spectral. The optical axes of the two recording systems were exactly in the middle between the electrical contacts and at an angle of 45° to the normal of the sample surface, which was uniformly irradiated by the X-ray quanta (Figure 1).

When using an integral channel, the luminescent radiation was focused using quartz lens onto the photocathode of a photoelectric multiplier PMT-106.

For the spectral registration the luminescent irradiation from the sample through a quartz condenser and a monochromator MDR-2 (600 lines/mm diffraction grating) was recorded either PMT-106 (in the spectral range of 350 – 820 nm) or cooled PMT-83 (in the range of 600 – 1200 nm). The accuracy of determining the intensity of X-ray luminescence was not worse than 3%, and TSL – 5% and was limited by the presence of the dark currents of the photomultiplier and the noises of the recording system. All luminescence spectra were corrected for the spectral sensitivity of the recording system.

2. Results of the Experimental Studies

2.1. The Luminescence Spectra for X-Ray Luminescence of the ZnSe. The characteristic XRL spectra for ZnSe single crystal ZnSe samples in the spectral region from 400 to 1200 nm at different temperatures (8 – 420 K) consist of two known [14–18] wide luminescence bands with maxima at 630 nm (1.92 eV) and 970 nm (1.28 eV). The spectra of different high-resistance samples differ only in the intensity ratio of these two main luminescence bands. Figure 2 shows the XRL spectra of two ZnSe samples, which were studied in detail for the dose dependencies of TSL and TSC. The edge luminescence and the luminescence of donor-acceptor pairs in high-resistance ZnSe samples were not found.

The 630 nm band, according to [14, 15], is due to the complex center which contains a zinc vacancy, and the band with a maximum at 970 nm is due to the complex center with a selenium vacancy [16, 17]. Both XRL bands are due to the luminescence recombination mechanism since they are observed in the phosphorescence and TSL [18]. The spectral maxima of these bands [19] vary little with temperature change, which allows recording them at a fixed wavelength at different temperatures. In all luminescence studies for the 970 nm band, the registration was carried out at a wavelength of 953 nm, since at this length the maximum luminescence of this band is observed without taking into account the spectral sensitivity of the recording system.

2.2. Thermally Stimulated Luminescence and Conductivity ZnSe. The TSL and TSC curves are intense enough to register, and they indicate a significant level of stockpiling of the charge carriers at the traps. For convenience, we will denote TSL curves when registering in the 630 nm band as TSL-630 and TSL-970, when registering in the 970 nm band. Figures 3 and 4 show the characteristic TSL-630, TSL-970, and TSC curves for two samples of ZnSe single crystal at high and low radiation doses. It should be noted that the ratio of the intensities of the TSL and TSC peaks vary for different samples, which indicates a different concentration of various traps in different ZnSe crystals.

Most of the charge carriers are thermally delocalized from the traps when heated to a temperature of 250 K, which indicates the dominance of the concentration of traps which

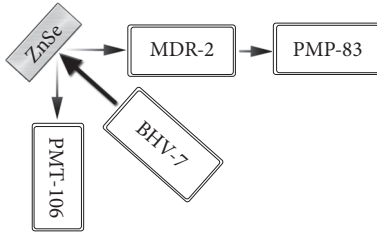


FIGURE 1: Geometry of XRL and TSL spectra registration.

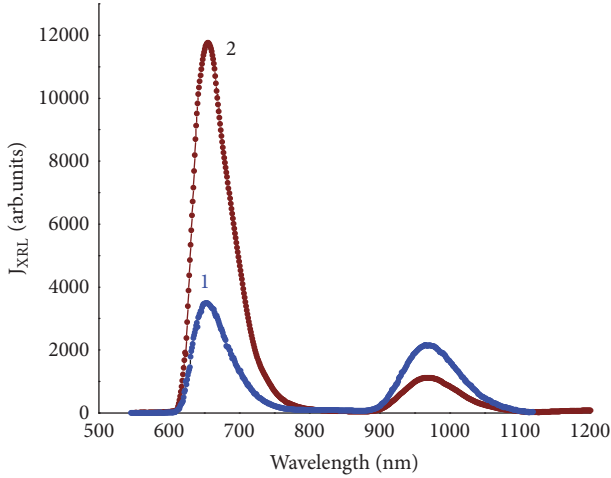


FIGURE 2: XRL spectra of the first (1) and the second (2) ZnSe samples at 85 K.

are not deep-level traps in the test material. The most high-temperature maximum (very weak) is observed at $T_m = 292$ K on the TSC curves.

In the TSL and TSC curves for each ZnSe sample the same peaks are observed. Thus, for the first sample, the dominant peaks are $T_m \sim 129$ K, 170 K, 184 K, 211 K, and 238 K. For the second sample, the dominant peaks on the TSL and TSC curves are $T_m \sim 143$ K, 170 K, 184 K, and 224 K and a weak peak at 292 K, which is not visible in the TSL due to the temperature luminescence extinction of 630 nm and 970 nm bands. Let us note that although the temperature position of one and the same TSL and TSC peak do not coincide (and should not coincide), but the temperature difference between them does not exceed 2-3 K, which is significantly less than the temperature difference between adjacent peaks [20] ($\Delta T_m = 13.6$ K).

The similarity between the TSL curves when registering at two recombination centers TSL-630 and TSL-970 and TSC curves means that the delocalization of charge carriers from any trap leads to the appearance of free carriers in the zone (TSC peak) and their subsequent recombination at the recharged luminescence centers of both samples (630 and 970 nm), the TSL peaks. It also indicates that we have a similar electronic recombination mechanism at the luminescence centers, which determine the 630 and 970 nm bands.

An analysis of the temperature position of the TSL and TSC peaks in ten different samples of ZnSe single crystals at $\beta = 0.40$ K/s shows that peaks from the same set are observed, and their intensities vary significantly in different samples. That is, for ZnSe single crystals, there is a certain set of traps and various samples differing only in the concentration ratio. Moreover, this set of traps corresponds to the data [20] and obeys the formula of a harmonic oscillator.

The temperature position of the TSL and TSC peaks practically does not alter with a change in the dose of X-ray irradiation ($D = I_X \cdot \tau_X$) from the minimum (D_{\min}) to the maximum (D_{\max}), while $D_{\max}/D_{\min} = 10,000$. Since the TSL and TSC peaks from neighboring traps noticeably overlap, firstly the temperature position of peaks was determined for the resulting experimental maxima, depending on the X-ray irradiation dose. Once it was verified that the temperature situation remains unchanged within a few degrees, the next step was to decompose the TSL and TSC curves into its components. In this case, the theoretical forms of the peaks of the TSL and TSC curves, given in [19], were used. It was verified that the temperature positions of the maxima of these components also remain practically unchanged at various doses of irradiation. It indicates that the probability of relocalization to the same trap is much less than the total probability of recombination at different luminescence centers and localization to the deeper traps. But the accumulation rate for traps of different depths is different, and therefore the TSL and TSC curves (Figures 3 and 4), obtained at different doses of X-ray irradiation, differ.

At high temperatures ($T > 350$ K) in all ZnSe samples, we observe conductivity appearance, while the current magnitude does not depend on the X-ray dose received. Reheating without irradiation repeats this dependence of the current magnitude on temperature. It clearly indicates that at $T > 350$ K the dark conductivity grows in these ZnSe samples.

Referring to papers that have been previously published, the way how to determine trap concentrations sometimes has been used a *thermostimulated conductivity (TSC) technique* [21, 22]. However, with this method, the filling of the trap levels could not be more accurately determined and does not consider the spatial distribution of localized charge carriers on traps.

3. The Light Sum Accumulation in ZnSe Single Crystals

The classical kinetic theories of luminescence and conductivity are not suitable for determining the kinetics of charge carrier accumulation on deep traps since they use a model of crystal phosphors with one type of traps and one luminescence center. In real crystals, several traps are always observed (several peaks on the TSL and TSC curves). Let us consider the light sum accumulation on deep traps within multicenter model of crystal phosphor, in which at excitation temperature T_0 the following are present: several types of shallow traps, phosphorescent trap, and several types of deep traps for electrons, and at least two kinds of luminescent centers with

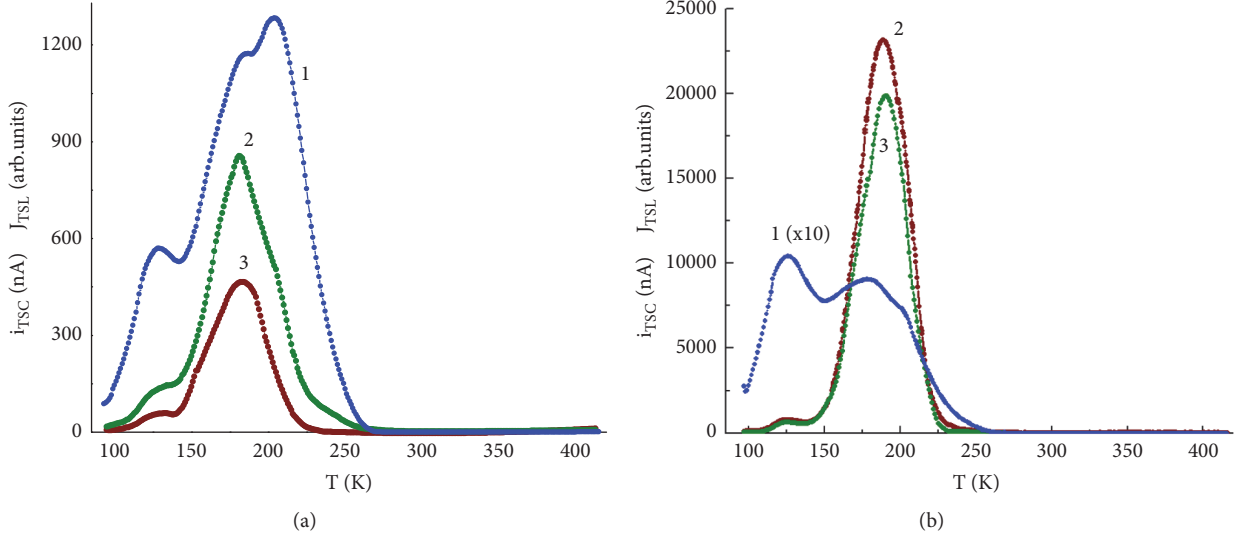


FIGURE 3: TSC (1), TSL-630 (2), and TSL-970 (3) curves of ZnSe sample #1: at a low dose of radiation ($D_X = 7.8 \text{ mJ/cm}^2$) (a) and at a high dose of radiation ($D_X = 4608 \text{ mJ/cm}^2$) (b).

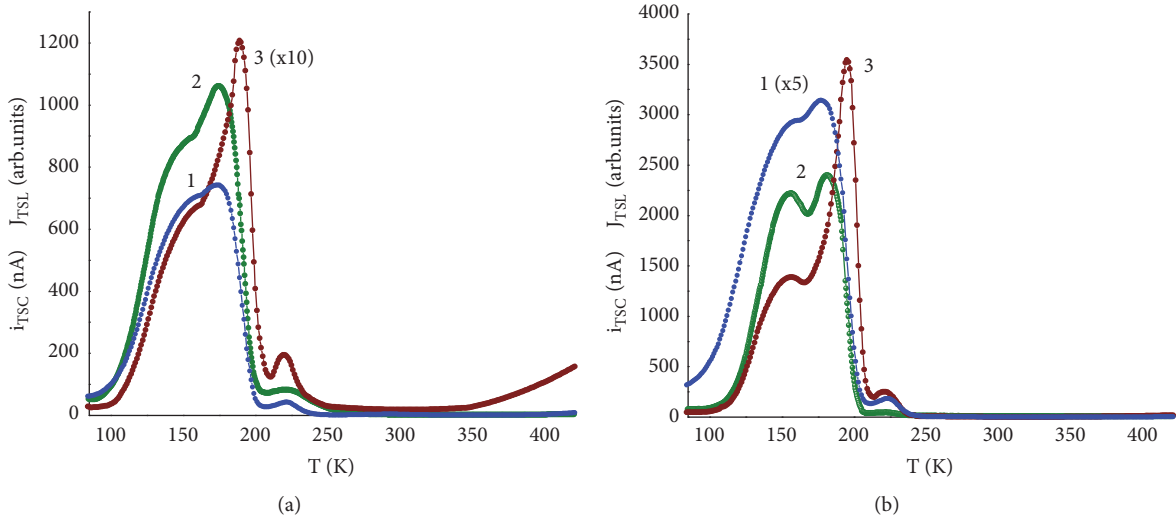


FIGURE 4: TSC (1), TSL-630 (2), and TSL-970 (3) curves of ZnSe sample #2: at a low dose of radiation ($D_X = 7.8 \text{ mJ/cm}^2$) (a) and at a high dose of radiation ($D_X = 4608 \text{ mJ/cm}^2$) (b).

electronic recombination mechanism (deep traps for holes). Shallow traps do not significantly affect the luminescence kinetics since electrons on them are in a localized state for a very short time ($< 1 \text{ s}$).

We can determine the levels of deep traps' maximum filling (r_e) based on their kinetic equations (for example, for m - and k -type traps) for the stationary state:

$$\begin{aligned} \frac{\partial n_m}{\partial t} &= N^- u^- \sigma_m^- (v_m - n_m) - w_m n_m - P^+ u^+ \sigma_m^+ n_m = 0 \\ \frac{\partial n_k}{\partial t} &= N^- u^- \sigma_k^- (v_k - n_k) - w_k n_m - P^+ u^+ \sigma_k^+ n_k = 0 \end{aligned} \quad (1)$$

and kinetic equations for free electrons (N^-) and holes (P^+)

$$\begin{aligned} \frac{\partial N^-}{\partial t} &= G - \sum N^- u^- \sigma_m^- (v_m - n_m) - \sum w_m n_m \\ &\quad - \sum N^- u^- \sigma_j^- p_j = 0 \\ \frac{\partial P^+}{\partial t} &= G - \sum P^+ u^+ \sigma_j^+ (v_{p_j} - p_j) - \sum w_j p_j \\ &\quad - \sum P^+ u^+ \sigma_m^+ n_m = 0 \end{aligned} \quad (2)$$

using the notation: n and p are the concentrations of the localized electrons and holes; u^- and u^+ are the thermal velocity of free charge carriers; σ is localization cross sections

(the superscript is the sign of the charge of the free carrier; subscript is a type of the local center); ν is concentrations of local centers; w is the probability of thermal delocalization of charge carriers; G is the generation rate of free charge carriers (proportional to the excitation intensity I_x).

Since the probability of thermal delocalization from deep traps is very small ($w_m, w_k, w_j \approx 0$), this process can be neglected. As a result, the maximum concentration of localized electrons ($n_{m\infty}, n_{k\infty}$) will be determined by the competition of two processes: the localization of free electrons and the recombination of free holes with localized electrons. From (2), it is possible to obtain stationary concentrations of free electrons and holes, which are determined by the intensity of generation of free charge carriers (G) and their lifetime in the zones (τ^-, τ^+) [19]:

$$\begin{aligned} N^- &= G\tau^- = \frac{G}{\sum u^- \sigma_m^- \nu_m}, \\ P^+ &= G\tau^+ = \frac{G}{\sum u^+ \sigma_j^+ \nu_{pj}} \end{aligned} \quad (3)$$

When a steady state is reached, if we consider that the ratio of the cross sections of holes localization to the electron's localization σ_m^+/σ_m^- should not vary much for each of the deep traps, then for the maximum level of deep traps filling we get

$$\begin{aligned} \frac{n_{m\infty}}{\nu_m} &= \frac{1}{1 + (\sigma_m^+/\sigma_m^-) (\sum \nu_d \sigma_d^- / \sum \nu_p \sigma_p^+)} \approx \frac{n_{k\infty}}{\nu_k} \\ &= \frac{1}{1 + (\sigma_k^+/\sigma_k^-) (\sum \nu_d \sigma_d^- / \sum \nu_p \sigma_p^+)} = r_e \end{aligned} \quad (4)$$

For two types of luminescence centers ($j=1,2$), which are deep traps for holes, it is also logical to introduce the level of their recharge (r_h). For them, the corresponding kinetic equations will be

$$\begin{aligned} \frac{\partial p_1}{\partial t} &= P^+ u^+ \sigma_1^+ (\nu_{p1} - p_1) - N^- u^- \sigma_1^- p_1 = 0 \\ \frac{\partial p_2}{\partial t} &= P^+ u^+ \sigma_2^+ (\nu_{p2} - p_2) - N^- u^- \sigma_2^- p_2 = 0 \end{aligned} \quad (5)$$

Similarly, as for electrons, we get

$$\begin{aligned} \frac{p_{1\infty}}{\nu_{p1}} &= \frac{1}{1 + (\sigma_1^-/\sigma_1^+) (\sum \nu_{pj} \sigma_{pj}^+ / \sum \nu_d \sigma_d^-)} \approx \frac{p_{2\infty}}{\nu_{p2}} \\ &= \frac{1}{1 + (\sigma_2^-/\sigma_2^+) (\sum \nu_{pj} \sigma_{pj}^+ / \sum \nu_d \sigma_d^-)} = r_h \end{aligned} \quad (6)$$

if the ratio of the cross sections of the localization of electrons and holes σ_j^-/σ_j^+ is not very different for various recombination centers.

At excitation in crystal phosphors at each moment of time, the charge conservation law must be satisfied; that is, the balance equation must be satisfied

$$p_1 + p_2 = \sum n_d \implies r_h (\nu_{p1} + \nu_{p2}) = r_e \sum \nu_d \quad (7)$$

The number of electrons localized in the traps should correspond to the number of localized holes. As a result, the following equation should be satisfied:

$$\begin{aligned} \frac{r_e}{r_h} &= \frac{\sum \nu_p}{\sum \nu_d} = \frac{1 + (\sum \nu_p \sigma_p^+ / \sum \nu_d \sigma_d^-) (\sigma_j^- / \sigma_j^+)}{1 + (\sum \nu_d \sigma_d^- / \sum \nu_p \sigma_p^+) (\sigma_m^- / \sigma_m^+)} \\ &\cong \frac{\sum \nu_p \sigma_p^+ \sigma_j^-}{\sum \nu_d \sigma_d^- \sigma_j^+} \end{aligned} \quad (8)$$

Equation (8) will be valid for all crystal phosphors, in which the ratio of localization cross sections for electrons and holes is not very different for various traps and for various luminescence centers.

By using (8), which we substitute in (4) and (6), we obtain simple relations for the filling levels of the deep traps and the recharge level of the luminescence centers:

$$\begin{aligned} r_e &= \frac{n_{m\infty}}{\nu_m} = \frac{n_{k\infty}}{\nu_k} = \frac{1}{1 + \sum \nu_d / \sum \nu_{pj}} = \frac{\sum \nu_{pj}}{\sum \nu_d + \sum \nu_{pj}} \\ r_h &= \frac{p_{1\infty}}{\nu_{p1}} = \frac{p_{2\infty}}{\nu_{p2}} = \frac{1}{1 + \sum \nu_{pj} / \sum \nu_d} = \frac{\sum \nu_d}{\sum \nu_d + \sum \nu_{pj}} \end{aligned} \quad (9)$$

Thus, the maximum recharge levels for the deep traps and luminescence centers are determined by the relation of concentrations, while the following is performed: $r_e + r_h = 1$.

For such a multicenter model of crystal phosphorus, it is possible to determine the kinetics of electron accumulation on deep traps by integrating the differential equation (1) with the initial condition: at $t = 0$ all $n_m = 0$.

$$\begin{aligned} \frac{\partial n_m}{\partial t} &= N^- u^- \sigma_m^- (\nu_m - n_m) - P^+ u^+ \sigma_m^+ n_m \implies \\ &\frac{dn_m}{n_m - (N^- u^- \sigma_m^- / (N^- u^- \sigma_m^- + P^+ u^+ \sigma_m^+)) \nu_m} \\ &= -(N^- u^- \sigma_m^- + P^+ u^+ \sigma_m^+) dt \\ n_m(t) &= n_{m\infty} \left\{ 1 - \exp \left[- \left(\frac{\sigma_m^-}{\sum \nu_d \sigma_d^-} + \frac{\sigma_m^+}{\sum \nu_{pj} \sigma_j^+} \right) G \cdot t \right] \right\} \\ &= n_{m\infty} \left\{ 1 - \exp \left(- \frac{t}{t_{Gm}} \right) \right\} \end{aligned} \quad (10)$$

where

$$\begin{aligned} n_{m\infty} &= r_e \nu_m, \\ t_{Gm} &= \frac{1}{(\sigma_m^- / \sum \nu_d \sigma_d^- + \sigma_m^+ / \sum \nu_{pj} \sigma_j^+) G} \end{aligned} \quad (11)$$

The t_{Gm} parameter differs for various traps, but their difference is determined by various localization cross sections. And since their difference is within the same order, the rates

of light sum accumulation on different traps will not differ very much. Of course, less deep traps saturate faster because $\sigma_m^- > \sigma_k^-$ if $m < k$. It is also confirmed experimentally (see Figures 3 and 4).

Respectively, according to the balance equation, the kinetics of accumulation of the recharged luminescence centers will be

$$p_1(t) + p_2(t) = \sum_m n_{m\infty} \left\{ 1 - \exp\left(-\frac{t}{t_{Gm}}\right) \right\} \quad (12)$$

Considering (9), eventually, we have

$$\begin{aligned} p_1(t) &= r_h v_{p1} \frac{\sum_m n_{m\infty} \{1 - \exp(-t/t_{Gm})\}}{\sum_m n_{m\infty}}, \\ p_2(t) &= r_h v_{p2} \frac{\sum_m n_{m\infty} \{1 - \exp(-t/t_{Gm})\}}{\sum_m n_{m\infty}} \end{aligned} \quad (13)$$

Thus, a theoretical consideration of the light sum accumulation in the crystal phosphors showed that, first, the maximum value of the accumulated light sum does not depend on the intensity of the exciting radiation, and the total concentrations of the deep traps and recombination centers are decisive. Secondly, the accumulated light sum value is determined by the radiation dose (a product of the intensity of the exciting radiation by the exposure $D_X = I_X \cdot \tau_X$). Thirdly, the kinetics of accumulation of the light sum on each type of deep trap are described by its simple exponential dependence, which allows determining the parameters of this exponent by several experimental points.

An important difference of the X-ray excitation is the spatial microinhomogeneity of the generation of the electronic excitations upon absorption of an X-ray quantum. Thousands of generated $e-h$ pairs are in a small area with a diameter of less than 0.5 microns. The Coulomb interaction between electrons and holes prevents the rapid expansion of this region. As a result, if there are a sufficient number of recombination centers in the material, as in our ZnSe samples, most of the free charge carriers will recombine in this local region, creating scintillations. It is confirmed experimentally by the dose dependencies of the luminescence at low temperatures [20]. It also means that not all generated free charge carriers are involved in the conductivity and localization on deep traps [23, 24].

3.1. The Experimental Dose Dependencies of TSC and TSL in ZnSe. The dose dependencies for the light sum accumulation in the ZnSe single crystals on different traps were determined by the intensities of the main TSL and TSC peaks. Each TSL and TSC curve was decomposed into components so that the sum of the components did not differ from the experimental TSL and TSC curves by more than 5%. We discovered that curve shapes (their half widths and peak temperature positions) are similar for different doses of X-ray radiation. Of course, at the same time, we neglected the peaks with very low intensities.

For all dose dependencies of the TSL and TSC peaks obtained at two X-ray excitation intensities ($I_{X1} = 0.13$ and

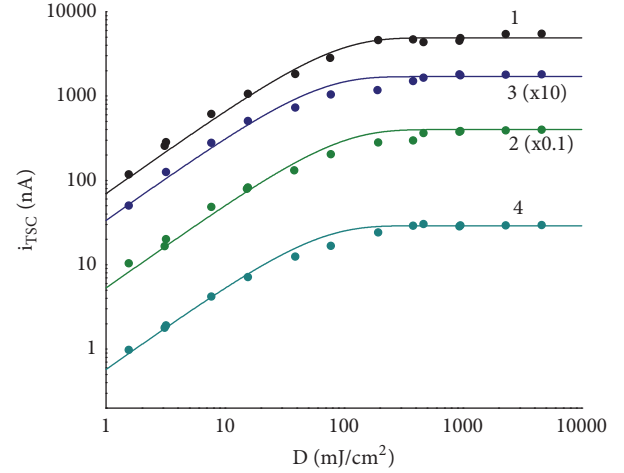


FIGURE 5: Dose dependencies of TSC peaks of ZnSe (#2) $T_m = 143$ K (1), 170 K (2), 183 K (3), and 224 K (4) with $U_0 = 15$ V (dots) and theoretical curves of the light sum accumulation (solid lines) by (10).

$I_{X2} = 0.64$ mW/cm²) we have almost similar peak intensities at the same radiation doses. That is, if $I_{X1} \cdot \tau_{1X} = I_{X2} \cdot \tau_{2X}$, then the corresponding TSL and TSC curves coincide with each other within the limits of error.

The characteristic dose dependencies of the TSC peaks of ZnSe single crystal at two X-ray excitation intensities are shown in Figure 5 by the example of the second sample (dots are the experimental values; lines are the theoretical dependencies (10)), the dependencies (2) and (3) are multiplied by certain coefficients for greater visibility. As expected, the t_{Gm} parameter value for different TSC peaks does not differ much from each other. Most importantly, the maximum accumulated concentration of electrons in deep traps does not depend on the intensity of the exciting X-ray radiation, that is, $n_{m\infty} \neq f(G)$.

Thus, the proposed multicenter model of crystal phosphor more sufficiently describes the light sum accumulation on deep traps than the classical kinetic theories. The second important point is that the kinetics of electron accumulation on traps is well described by the exponential dependence (10). The same dependence is observed for TSL. Figures 6 and 7 show the dose dependencies of TSL-630 and TSL-970.

All dose TSL and TSC curves are well approximated by the exponential dependence. Moreover, $t_{Gm} = \tau_{exp} \cdot I_X$ for each peak (that is, for each type of trap) there are almost the same values for the two excitation intensities and which differ fivefold. It means that the rate and kinetics of the light sum accumulation for each peak are the same at any excitation intensity.

When comparing the light sum accumulation for each peak in different recording channels, it should be noted that there is a more rapid saturation of TSC peaks rather than the TSL peaks (t_{Gm}^{TSC} less related t_{Gm}^{TSL} by several times). It agrees well with the core differences between TSL and TSC. The TSC curves show the variation of the concentration of the free electrons delocalized from the traps $N^-(T)$, while the TSL curves are the product of the concentration of free electrons

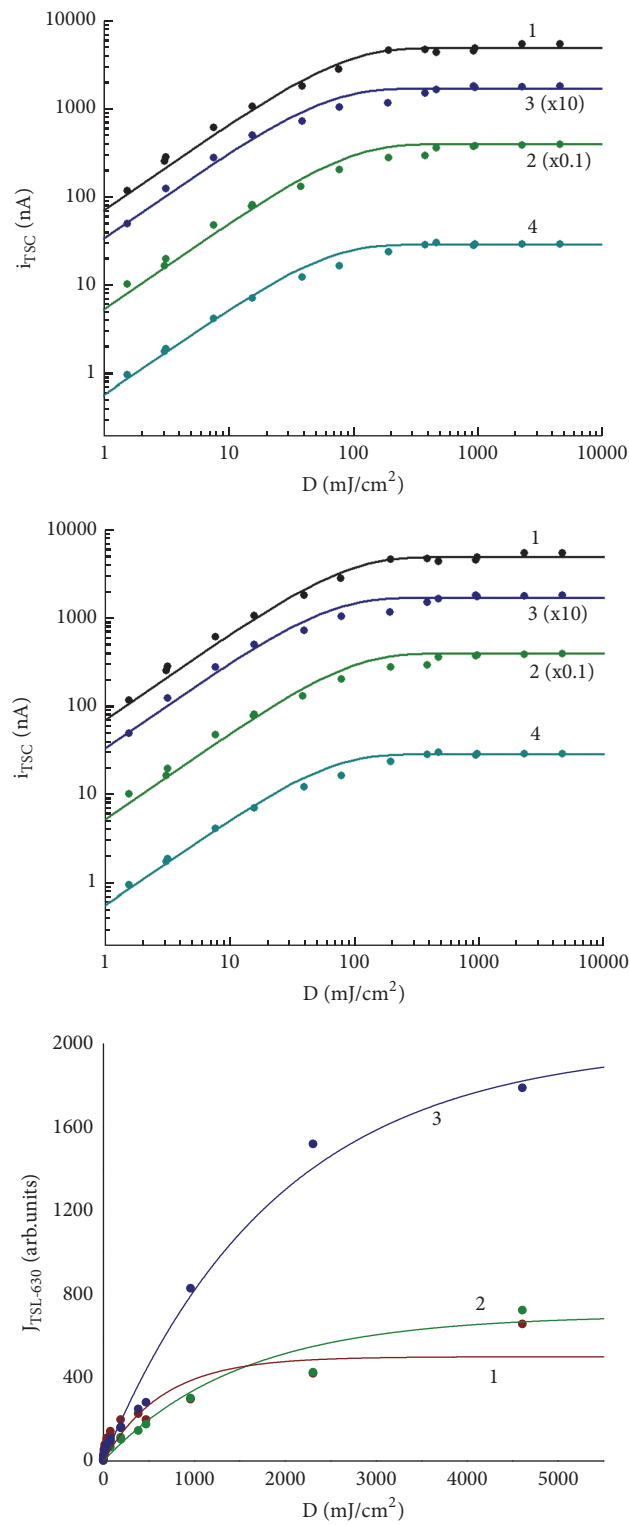


FIGURE 6: Dose dependencies of the TSL-630 peaks at $T_m = 129$ K (1), 184 K (2), and 211 K (3) of the sample #1 under two intensities of X-ray excitation and the theoretical curves of the light sum accumulation (solid lines).

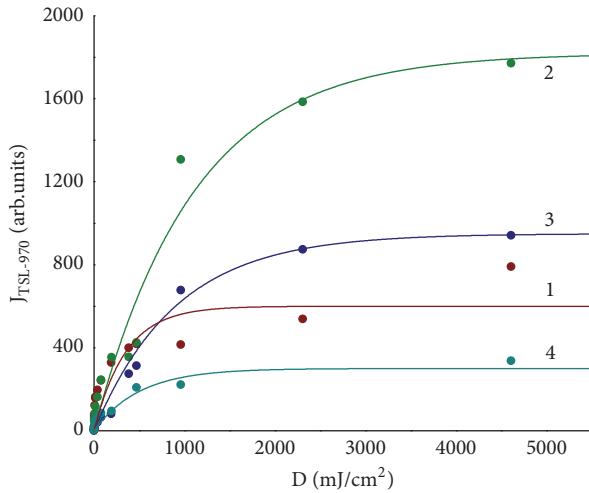


FIGURE 7: Dose dependencies of the TSL-970 peaks at $T_m = 129$ K (1), 184 K (2), and 211 K (3) of the sample #1 under two intensities of X-ray excitation (dots) and the theoretical curves of the light sum accumulation (solid lines) by (10).

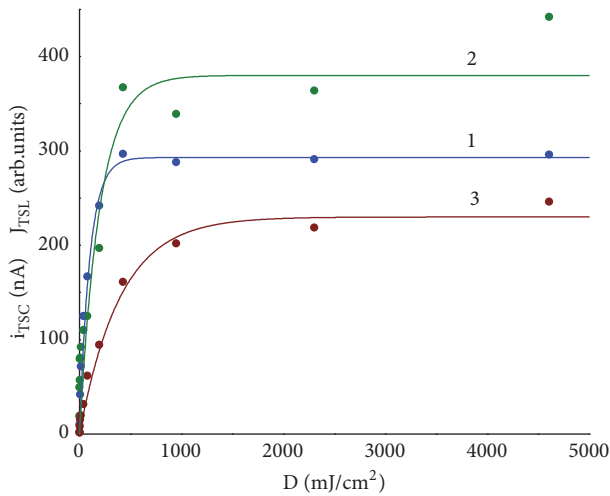


FIGURE 8: Dose dependencies of TSC (1), TSL-630 (2), and TSL-970 (3) peak $T_m = 224$ K of the ZnSe #2 sample at two X-ray excitation intensities (dots) and theoretical light sum accumulation curves (solid lines) by (10).

on the concentration of the recharged luminescence centers $N^-(T) \cdot p(T)$. As is known, the intensity of luminescence recombination is understood as the total number of free carriers' recombination events at the recharged recombination centers. It means that the dose dependencies of the TSC and TSL will differ, since $p(T)$ also changes during the excitation and the light sum accumulation and, accordingly, when recombining delocalized electrons. But it should be noted that the change in the concentration of the recharged luminescence centers occurs only by the magnitude of the delocalized electrons. That is, a relative change in the number of the recharged luminescence centers is not very significant when one type of an electron trap gets emptied. That is why the temperature positions of the corresponding TSL and TSC peaks differ slightly. For example, Figure 8 presents the dose

dependencies of the peak at $T_m = 224$ K of the second sample observed in both TSC and TSL-630, as well as TSL-970.

When comparing TSL-630 and TSL-970 it is necessary to take into account the fact that the intensity of the luminescence, which is being recorded, is due to the intracenter quantum output of the luminescence center and its temperature dependence; the geometric coefficient (determined by that part of the luminescent quanta that enters the recording system) by the spectral sensitivity of the recording system in the region of the luminescence spectrum. In fact, we consider a relative intensity, which is proportional to the product of the concentrations of free electrons and recharges of the recombination centers. The study of TSL and TSC of other zinc selenide single crystals did not reveal experimental facts that would contradict with these experimental results and theoretical conclusions.

Based on the results obtained, one can explain the behavior of the dose dependencies of the TSL and TSC for all traps. Thus, the total concentration of traps in the second sample is greater than in the first ZnSe sample. The light sum accumulation rate is determined by the ratio of recombination centers in the concentration of traps (and not just the traps concentration). The smaller the size of the localization region of the carriers at the absorption of an X-ray quantum is, the greater the concentration of traps is. Accordingly, in the first sample, a smaller part (than in the second one) of charge carriers goes to localization when one X-ray quantum is absorbed. It causes a slower initial rate of the light sum accumulation in the sample.

4. Conclusions

In ZnSe single crystals, the TSL curves, when detected on two luminescence bands (630 and 970 nm), and TSC curves have a similar character. It indicates that the peaks in the TSL and TSC are due to delocalization of the carriers from a trap to a zone of their subsequent recombination on both types of the recharged luminescence centers (630 and 970 nm). While the differences in the parameters of the light sum accumulation during the TSL registration on two luminescence bands are due to the difference in the parameters of the luminescence centers and their concentrations.

A theoretical model of crystal phosphors with several types of traps has been proposed for which was found next: (1) the accumulation of the light sum on each trap is described by a simple exponential dependence with its characteristic accumulation time and (2) the maximum accumulated light sum at the X-ray excitation does not depend on the intensity of exciting radiation. These conclusions are experimentally confirmed by the research of light sum accumulation in ZnSe single crystals at X-ray excitation.

It means that the classical model of crystal phosphor with one type of traps, which provides for a maximum accumulated light sum the dependence $n_{\infty} \sim \sqrt{I_{ex}}$ is too simplistic. It is necessary to use a model of crystal phosphors with several types of traps, for which the dynamics of the accumulation of the light sum on each trap is described by a simple exponential dependence with its characteristic accumulation time and which gives the independence of

the value of the maximum accumulated light sum from the excitation intensity.

Data Availability

All authors declare that they agree to share the data underlying the findings of their manuscripts. Accordingly, they were provided “data availability” to publish the data used in their manuscripts.

Conflicts of Interest

The authors declare that they have no conflicts of interest.

References

- [1] V. I. Gavrilenko, A. M. Grehov, D. V. Korbutyak, and V. G. Litovchenko, *Optical Properties of Semiconductors*, Naukova Dumka, Kiev, Ukraine, 1987.
- [2] N. K. Morozova, V. A. Kuznetsov, and V. D. Ryzhikov, *Zinc Selenide. Receiving and Optical Properties*, Science, 1992.
- [3] L. V. Atroshchenko, S. F. Burachas, L. P. Galchinetski, B. V. Grinev, V. D. Ryzhikov, and N. G. Starzhinskii, *Scintillation Crystals and Ionization Radiation Detectors on Their Base*, Naukova dumka, Kiev, Ukraine, 1998.
- [4] I. Dafinei, M. Fasoli, F. Ferroni et al., “Low temperature scintillation in ZnSe crystals,” *IEEE Transactions on Nuclear Science*, vol. 57, no. 3, pp. 1470–1474, 2010.
- [5] N. Starzhinskiy, B. Grinyov, I. Zenya, V. Ryzhikov, L. Galchinetski, and V. Silin, “New trends in the development of $A^{11}B^{VI}$ -based scintillators,” *IEEE Transactions on Nuclear Science*, vol. 55, no. 3, pp. 1542–1546, 2008.
- [6] V. D. Ryzhikov, “Properties of semiconductor scintillators ZnSe(Te,O) and integrated scintielectronic radiation detectors based thereon,” *IEEE Transactions on Nuclear Science*, vol. 48, no. 1, pp. 356–359, 2001.
- [7] M. S. Brodyn, V. Y. Degoda, A. O. Sofienko, B. V. Kozhushko, and V. T. Vesna, “Monocrystalline ZnSe as an ionising radiation detector operated over a wide temperature range,” *Radiation Measurements*, vol. 65, pp. 36–44, 2014.
- [8] E. I. Adirovich, *Some Questions in the Theory of Luminescence of Crystals*, State Publishing House of Technical and Theoretical Literature, Moscow, Russia, 1956.
- [9] M. V. Fock, *Introduction to Kinetics of Luminescence of Phosphor Crystals*, Nauka, Moscow, Russia, 1964.
- [10] V. V. Antonov-Romanovski, *Photoluminescence Kinetics of Phosphor Crystals*, Nauka, Moscow, Russia, 1966.
- [11] A. Rose, *Concepts in Photoconductivity and Allied Problems*, Interscience publishers, New York, NY, USA, 1963.
- [12] R. H. Bube, *Photoconductivity of Solids*, John Wiley & Sons, New York, NY, USA, 1960.
- [13] V. E. Lashkarev, A. V. Lyubchenko, and M. K. Sheinkman, *Nonequilibrium Processes in Photoconductors*, Nauk Dumka, Kiev, Ukraine, 1981.
- [14] L. V. Atroshchenko, L. P. Galchinetski, S. N. Galkin, V. D. Ryzhikov, and V. I. Silin, “Structure defects and phase transition in tellurium-doped ZnSe crystals,” *Journal of Crystal Growth*, vol. 197, no. 3, pp. 475–479, 1999.
- [15] V. M. Koshkin, A. Ya. Dulfan, V. D. Ryzhikov, L. P. Galchinetski, and N. G. Starzhinskiy, “Thermodynamics of isoivalent tellurium substitution for selenium in ZnSe semiconductors,” *Journal of Functional Materials*, vol. 8, no. 4, pp. 708–713, 2001.
- [16] N. K. Morozova, I. A. Karetnikov, V. V. Blinov, and E. M. Gavrishchuk, “A study of luminescence centers related to copper and oxygen in ZnSe,” *Semiconductors*, vol. 35, no. 1, pp. 24–32, 2001.
- [17] N. K. Morozova, I. A. Karetnikov, V. V. Blinov, and E. M. Gavrishchuk, “Studies of the infrared luminescence of ZnSe doped with copper and oxygen,” *Semiconductors*, vol. 35, no. 5, pp. 512–515, 2001.
- [18] V. Y. Degoda, N. Y. Pavlova, G. P. Podust, and A. O. Sofienko, “Spectral structure of the X-ray stimulated phosphorescence of monocrystalline ZnSe,” *Physica B: Condensed Matter*, vol. 465, pp. 1–6, 2015.
- [19] V. Ya. Degoda, A. F. Gumenjuk, and Yu. A. Marazuev, *Kinetics of Luminescence and Conductivity on Phosphor Crystals*, Kiev, Ukraine, 2016.
- [20] V. Ya. Degoda, M. Alizadeh, N. O. Kovalenko, and N. Yu. Pavlova, “The dependencies of x-ray conductivity and x-ray luminescence of ZnSe crystals on the excitation intensity,” *Advances in Condensed Matter Physics*, vol. 2018, Article ID 1515978, 8 pages, 2018.
- [21] A. Aydinli, N. M. Gasanly, and S. Aytikin, “Trap levels in layered semiconductor Ga_2Se_3 ,” *Solid State Communications*, vol. 132, no. 12, pp. 857–861, 2004.
- [22] T. Yildirim, B. Sülünhat, and N. M. Gasanly, “Low temperature thermally stimulated current measurements in N-implanted TlGaSeS layered single crystals,” *Materials Science in Semiconductor Processing*, vol. 34, pp. 121–125, 2015.
- [23] V. Y. Degoda, M. Alizadeh, N. O. Kovalenko, and N. Y. Pavlova, “V-I characteristics of X-ray conductivity and UV photoconductivity of ZnSe crystals,” *Journal of Applied Physics*, vol. 123, no. 7, Article ID 075702, 2018.
- [24] D. V. Lang, “Deep-level transient spectroscopy: a new method to characterize traps in semiconductors,” *Journal of Applied Physics*, vol. 45, no. 7, pp. 3023–3032, 1974.

Research Article

Thickness Induced Line-Defect Reconfigurations in Thin Nematic Cell

M. Ambrožič ^{1,2,3} and S. Kralj ^{1,2}

¹Faculty of Mathematics and Natural Sciences, University of Maribor, Koroška 160, Maribor, Slovenia

²Jožef Stefan Institute, Jamova 39, Ljubljana, Slovenia

³Faculty of Industrial Engineering, Šegova 112, Novo mesto, Slovenia

Correspondence should be addressed to M. Ambrožič; milan.ambrozic@um.si

Received 29 November 2018; Accepted 10 February 2019; Published 4 March 2019

Guest Editor: Jiajie Zhu

Copyright © 2019 M. Ambrožič and S. Kralj. This is an open access article distributed under the Creative Commons Attribution License, which permits unrestricted use, distribution, and reproduction in any medium, provided the original work is properly cited.

We studied the impact of the cell thickness on configurations of line disclinations within a plane-parallel nematic cell. The Lebwohl-Lasher semimicroscopic approach was used and (meta)stable nematic configurations were calculated using Brownian molecular dynamics. Defect patterns were enforced topologically via boundary conditions. We imposed periodic circular nematic surface fields at each confining surface. The resulting structures exhibit line defects which either connect the facing plates or remain confined within the layers near confining plates. The first structure is stable in relatively thin cells and the latter one in thick cells. We focused on structures at the threshold regime where both structures compete. We demonstrated that “history” of samples could have strong impact on resulting nematic configurations.

1. Introduction

Line topological defects are ubiquitous in nematic liquid crystals (NLC) which is fingerprinted even in their name [1]. They could be stabilised topologically by appropriate boundary conditions [2, 3] or due to energy reasons [4]. They have a strong impact on optical NLC properties and are therefore of potential interest for various electro-optic applications.

Nematic uniaxial liquid crystals exhibit simultaneously liquid properties and local orientational order [5]. The latter is at macroscopic level commonly presented by the nematic director field \vec{n} . It points along the local uniaxial order, where states with $\pm\vec{n}$ are physically equivalent. In bulk equilibrium \vec{n} is spatially homogeneous and aligned along a single symmetry breaking direction. NLC can exhibit line dislocations, which are characterised by the winding number $m = \pm 1/2$ [6, 7]. It reveals the total reorientation of \vec{n} on encircling the defect in counter-clockwise direction. Furthermore, one can assign the total topological charge q to a line defect [6] by enclosing it by a surface. This charge is integer and reveals how many realizations of all orientations

are realised in the nematic order parameter space [6]. Note that the core structure of line $m = \pm 1/2$ line defects is biaxial [8], and the center of the core exhibits negative uniaxiality.

Line defects could be stabilised in different ways. For example, they could be enforced by AFM imprinted patterns to plates enclosing NLC in plane-parallel geometry as illustrated in [2]. It has been shown [9] that, in such geometries the line defects could either span the opposite plates or are confined to the vicinity of the bounding plates. In this paper we focus on these competing structures. We henceforth refer to the defect configurations that (i) connect the bounding plates and (ii) remain confined close to the planes, as the (i) *connected* and (ii) *confined* defect configurations, respectively. In our study we consider networks of line defects in a plane-parallel cell of thickness h . We use the Lebwohl-Lasher semimicroscopic lattice model [10, 11] where the local orientational order is presented by nematic pseudospins. We assume that the bounding plates are patterned by a lattice of concentric circles, enforcing the circular planar nematic alignment, which give rise to line defects. We focus on the impact of h and history of samples on defect patterns. The plan of the paper is as follows. In Section 2 we present model

and in Section 3 results. In the final section we summarize our results.

2. Materials and Methods

We consider nematic structures within a plane-parallel cell of thickness h . At the bounding plates we enforce spatially varying nematic patterns and calculate the corresponding nematic structures within the cell. In our modelling we use the semimicroscopic Lebwohl-Lasher lattice approach [10, 11]. In this modelling the nematic orientational ordering is described in terms of nematic spins \vec{S} (states with $\pm \vec{S}$ are physically equivalent) residing at each lattice site. We henceforth refer to unit vectors \vec{S} as *spins*. The simulation lattice is cubic, characterised by the lattice constant a_0 .

The simulation lattice consists of $M \times M \times L$ sites in the Cartesian coordinate system (x, y, z) . Here L is proportional to the cell thickness, i.e., $h = La_0$, while $M \gg L$ stands for its lateral dimensions. In the following we set $a_0 = 1$, so that we identify L with the cell thickness. Individual sites are denoted by a set of indices (i, j, k) : $1 \leq i \leq M$, $1 \leq j \leq N$, and $1 \leq k \leq L$. Each site is occupied by a *spin* \vec{S}_{ijk} , which tends to orient in parallel direction with its nearest neighbors. The bounding plates have imprinted a two-dimensional (2D) circular nematic “surface field” (see Figures 1 and 2, top left), which enforces line defects to the LC body. Therefore, we impose a lattice of two-dimensional $m = 1$ topological point defects. This surface imprinted structure is positioned symmetrically on both plates. In the model the surface field is determined by frozen-in *spins* at the bounding plates.

The coupling between neighboring *spins* inside the cell is given by the coupling constant $J > 0$, while the coupling between the plates and the nearby spins is parametrized with the anchoring strength $W > 0$. The bulk interaction energy F is the sum of the terms over all lattice sites:

$$F = -\frac{J_{LL}}{2} \sum_{ijk} \sum_{n.n} (\vec{S}_{ijk} \cdot \vec{S}_{n.n})^2, \quad (1)$$

where $J_{LL} = J$. The subscript *n.n.* in the inner sum denotes the 6 nearest neighbors of the site with indices (i, j, k) . The bottom and upper boundary plates are determined artificially by $k = 0$ and $k = L + 1$, respectively, and impose the nematic structure determined by frozen-in *spins*. The corresponding nearest inner *spin* planes (with $k = 1$ and $k = L$, respectively) interact with the boundary planes with the LL interaction written in (1), where $J_{LL} = W > J$. At the lateral boundaries we impose the periodic boundary condition. Besides the torques due to coupling between neighboring *spins* the random thermal fluctuations according to the Gaussian distribution of deviations from equilibrium are included. For numerical purpose, we introduce the dimensionless time step $\Delta t^* = D\Delta t$ and the dimensionless temperature $T^* = kT/J = kT$. Here D is the effective rotational diffusion coefficient, Δt is the physical time step, and k is the Boltzmann constant. Simulation details are described in [11]. Furthermore, we scale W in units of J .

A surface imposes *spin* configuration, consisting of a lattice of 2D circular defects with the winding number $m = 1$

on the boundary plate. Each circular pattern, centered at (x_0, y_0) , is determined by

$$\vec{S}_d \equiv (\cos \theta, \sin \theta, 0) = (-\sin \varphi, \cos \varphi, 0), \quad (2a)$$

$$\varphi = \arctan \frac{y - y_0}{x - x_0}. \quad (2b)$$

In (2a) and (2b) φ is the azimuthal angle in the (x, y) plane and θ is the angle between the *spin* and the x -axis; therefore $\theta = \varphi + \pi/2$ imposes a circular pattern. We place four equal and symmetrically positioned circular defects on each plate as shown in Figure 1. In between the circles we impose a homogeneously aligned *spin* field along the x -axis. Both confining plates impose the same *spin* field, i.e., $\vec{S}_{ij,L+1} = \vec{S}_{ij0}$.

In simulations we vary the cell thickness L . The remaining parameters are fixed: $W = 5$ and $T^* = 0.5$. These conditions correspond to a relatively strong anchoring deeply in the nematic phase.

For given conditions we calculate *spin* configurations using Brownian molecular dynamics, where details are described in [11]. We present key structural characteristics using the following quantities. We define the traceless tensor order parameter:

$$Q_{mn} = \frac{3}{2} \langle S_{ijk,m} S_{ijk,n} \rangle - \frac{1}{2} \delta_{mn}. \quad (3)$$

Here $S_{ijk,m}$ denotes the m -th component of the *spin* \vec{S}_{ijk} , while the triangular bracket denotes the average over the cell and δ_{mn} is the Kronecker symbol. The scalar order parameter S is conventionally defined as the largest eigenvalue of the tensor.

In order to measure impact of the bounding plates on the average LC configuration within the cell we define the quantity $S(0, k)$ which measures the average matching of *spins* in the k -th plane inside the cell with the frozen *spins* in the confining boundaries, i.e.,

$$S(0, k) = \frac{3}{2M^2} \sum_{i,j=1}^M (\vec{S}_{ijk} \cdot \vec{S}_{ij0})^2 - \frac{1}{2} \quad (4)$$

If the matching is perfect it holds $S(0, k) = 1$. Another useful macroscopic parameter is the mean value of the square of the *spin* component S_z , again with averaging over horizontal planes:

$$\langle S_z^2 \rangle(k) = \frac{1}{M^2} \sum_{i,j=1}^M (S_{ijk,3})^2 \quad (5)$$

Note that the bounding plates enforce zero z -component of the *spins*.

We study also the impact of sample “history” on *spins*. For this purpose we impose four different initial *spin* configurations: (1) *spin* configuration imposed by the plates (which we label by “D”), (2) homogeneous configuration with all the *spins* along the x -axis (“XH”), (3) homogeneous configuration with all the *spins* along the z -axis (“ZH”), and (4) random configurations, where the directions of the *spins* are randomly distributed according to isotropic distribution (“R”).

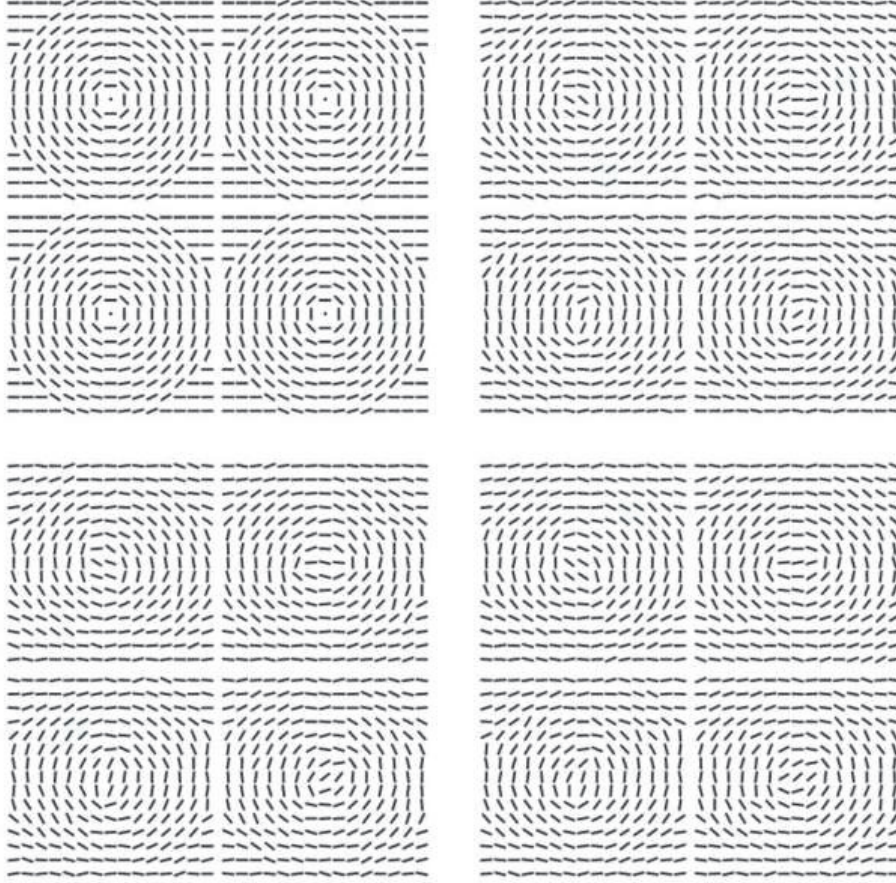


FIGURE 1: *Spin* configurations in different “horizontal” planes for the cell with thickness $L = 10$: $k = 0$, bottom control plane with circular defects (top left), $k = 3$ (top right), $k = 4$ (bottom left), and $k = 5$, middle of the cell (bottom right).

3. Results and Discussion

Of our interest is to analyse the thickness $h=La_0$ driven transformation between *connected* and *confined* defect configurations. In thin enough cells the surface boundary conditions stabilise a *connected* defect configuration. When the cell thickness is increased, the defect structure, as enforced by the plates, tends to unwind into preferable homogeneous structure in the bulk of the cell. This is indicated by 2D cross-sections parallel to the plate in Figures 1 and 2, where the initial *spin* configuration was “D” and the equilibrium *spin* configurations for two different thicknesses of the cell are compared: $L = 10$ (very thin cell) and $L = 30$ (thicker cell), respectively. Because of the symmetry it is sufficient to illustrate the *spin* configurations for the lower half of the cell, i.e., $k \leq L/2$. Thus the four configurations presented in either of Figures 1 and 2 represent the *spin* configuration for the planes with increasing distance from the bottom plate, indicated by increasing parameter k . In order to have a definite (albeit superficial) direction of the *spin* also in the center points of the defects, the *spin* was set to be aligned in z -direction, i.e., perpendicular to the plates there (dots at the defect centers in the figure).

It is evident from Figure 1 ($L = 10$) that the defect structure is essentially preserved through the cell for small thickness,

but the centers of the defects are smoothed. Thus the line disclinations essentially connect the confining plates. On the contrary, in Figure 2 ($L = 30$) the *spin* configuration in the middle of the cell is roughly homogeneous along the x -axis.

Different structures for cells with different thicknesses can also be forecast theoretically and revealed experimentally with the use of polarizing optical microscopy [12, 13]. The essence of the optical polarizing microscopy is the following. The NLC is positioned between a pair of crossed polarizers (perpendicular polarization directions). In the case of optically inactive medium in the cell no light passes through the second polarizer. However, the optically active medium, such as NLC, rotates the polarization direction because of the difference in ordinary and extra-ordinary refraction indices, and so the intensity of the transmitted light is nonzero. The degree of polarization rotation depends on nematic director field. In numerical simulation of the optical pattern, which mimics the experimental situation, the path of the beam through the NLC cell is divided into short segments, and at each segment the small rotation angle of the polarization is calculated by using the Jones matrix. If the direction of the light beam is z (perpendicular to the cell plates), the intensity of the transmitted light generally depends on (x, y) coordinates, resulting in characteristic optical pattern. Each pattern in our calculation corresponds to a single

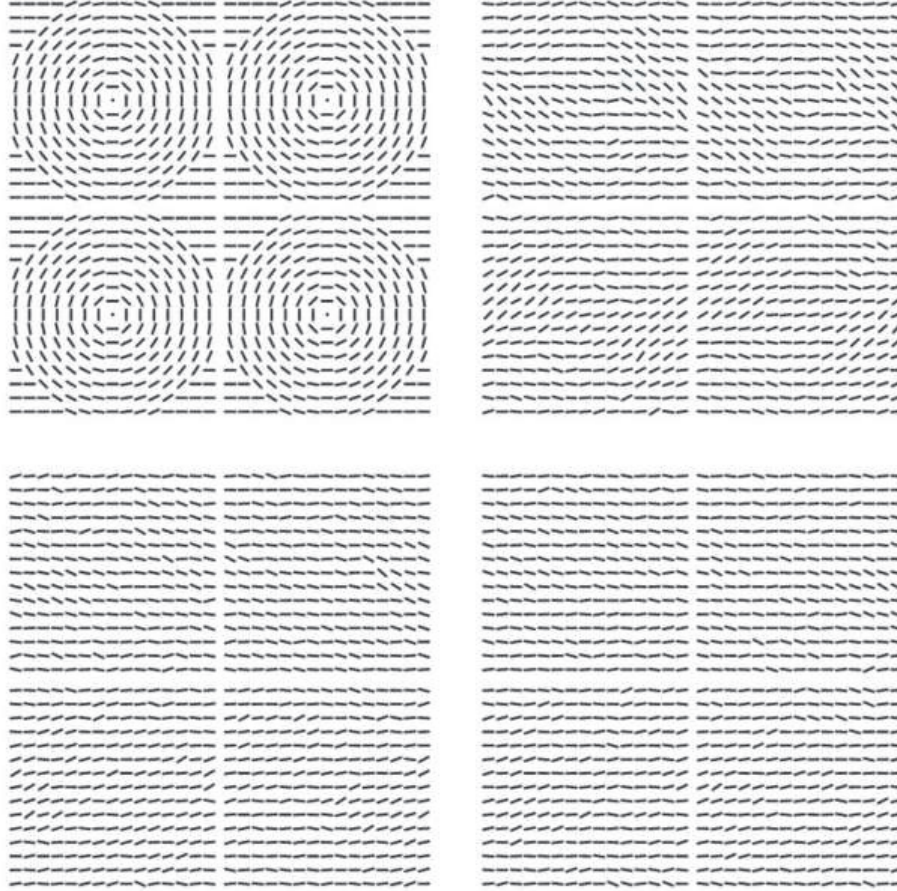


FIGURE 2: *Spin* configurations in different “horizontal” planes for the cell with thickness $L = 30$: $k = 0$ (top left, as for Figure 1), $k = 5$ (top right), $k = 10$ (bottom left), and $k = 15$, middle of the cell (bottom right).

configuration (snapshot). Theoretically modelled patterns for $L = 10$ and $L = 30$ are compared in Figure 3. The left image ($L = 10$) is characteristic for the winding number $m = 1$. However, some traces of the optical patterns of the $m = 1$ line defect are still present for thicker cell ($L = 30$, right image).

The structures (equilibrium *spin* configurations) presented in Figures 1 and 2 above indicate that there exists a threshold value of the cell thickness L_c above which the defect structure unwinds in the middle part of the cell (thicker cells). In our study L_c is between the values 20 and 30, where the thickness of the cell is approximately equal to the size of the imposed circles. The direction of the *spins* in the predominantly homogeneous part of the cell is parallel to the x -axis because this direction is favored by the alignment of frozen *spins* between the circles.

Furthermore, we have studied the effect of different initial *spin* configurations. In the case of thin cells ($L = 10$ or slightly larger) the final equilibrium configurations for all different initial configurations (“D”, “XH”, “ZH”, and “R”) are similar. This was shown by comparison of 2D horizontal cross-sections after relaxation, similarly as for Figures 1 and 2, and it has been also confirmed by similar values of parameters $S(0, k)$ and $\langle S_z^2 \rangle(k)$ in (4) and (5). The value of $\langle S_z^2 \rangle$ is of the order of 0.02 in the middle of the cell ($k = L/2$), indicating

that the spins predominantly lie in the (x, y) plane. The small S_z component is present because of thermal fluctuations.

Only the “ZH” initial *spin* configurations result in the equilibrium configuration which tends to deviate from the (x, y) plane configuration to larger extent, at least for larger values of L . For instance, for $L = 30$ we have found that the “ZH” initial configurations lead to equilibrium configuration with $\langle S_z^2 \rangle \approx 0.6$ at the middle of the cell, while the other three initial configurations result in $\langle S_z^2 \rangle \approx 0.02$, as in the case $L = 10$. However, other differences for initial *spin* configurations “D”, “XH”, and “R” have been noticed. As expected, the final configuration in the cell has the largest similarity to the defect configuration on the plate, when the initial configuration is “D”. This is also confirmed quantitatively by the largest value of the parameter $S(0, k)$ in (4) for all 2D planes (all values of k). Figures 4 and 5 show the plane averages $\langle S_z^2 \rangle$ and $S(0, k)$ as functions of the index k for all initial *spin* configurations and for thicknesses $L = 10$ and 30, respectively.

The degree of alignment of *spins* along the x -axis could be quantified by $\langle S_x^2 \rangle$ in a similar way as $\langle S_z^2 \rangle$ was defined in (5) for the z -component. The “R” initial configuration results in the equilibrium *spin* configuration between those corresponding to “D” and “XH”. We have also noticed that for thin cells ($L = 10$) the quantitative parameters, such as $S(0, k)$, for

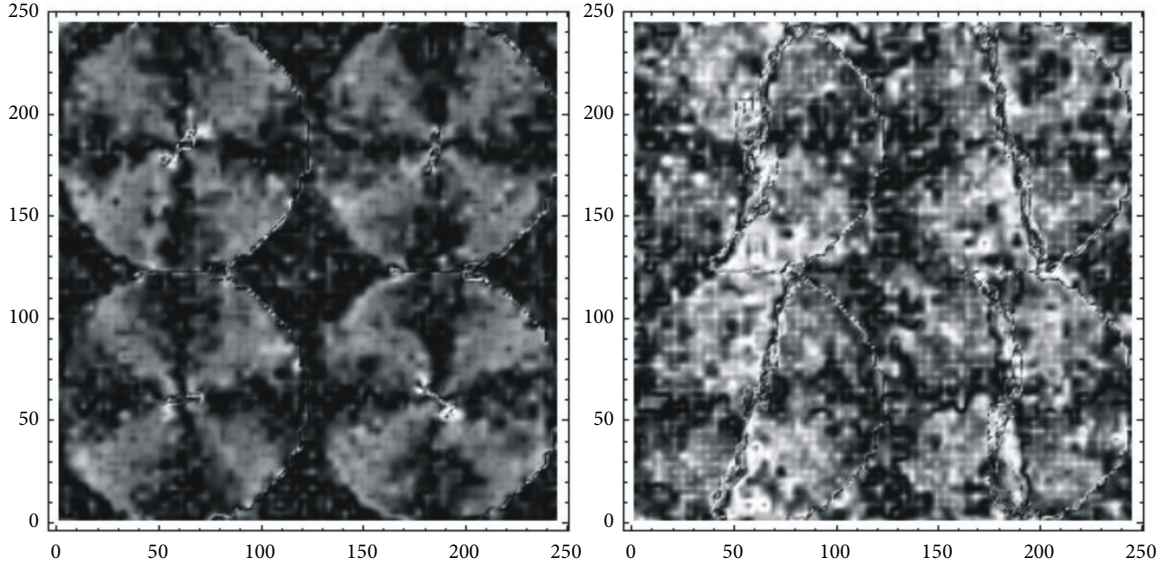


FIGURE 3: Polarizing optical microscopy patterns for two thicknesses: $L = 10$ (left) and $L = 30$ (right). These patterns correspond to spin configurations illustrated in Figures 1 and 2. The laser wavelength 445 nm was arbitrary chosen, and the ordinary and extraordinary refraction indices 1.544 and 1.821 correspond to NLC E7 [12, 13]. The real thickness was set to $h = 2 \mu\text{m}$ for the $L = 10$ cell and $6 \mu\text{m}$ for the $L = 30$ cell.

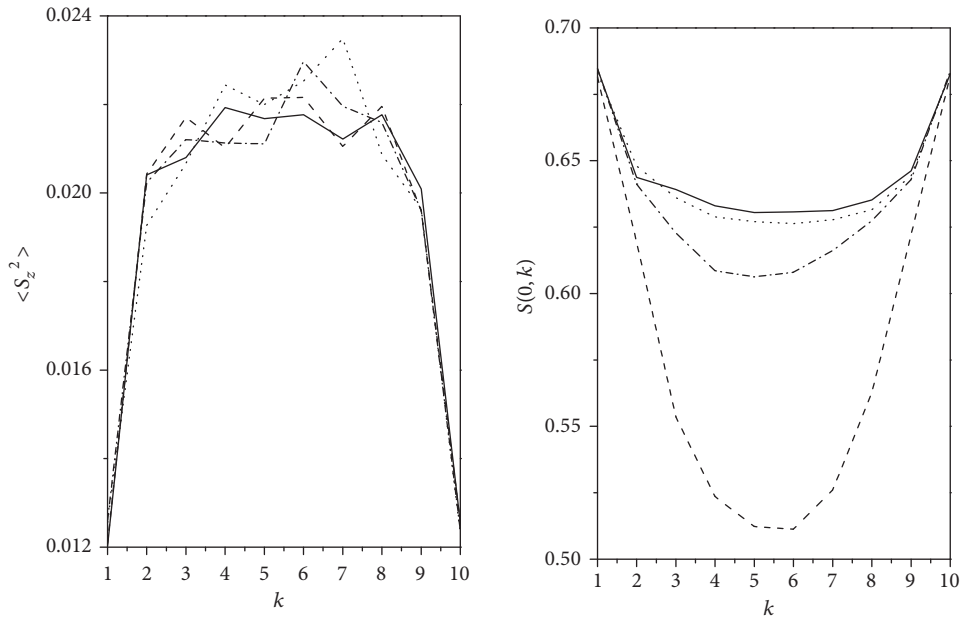


FIGURE 4: Dependence of the plane parameters $\langle S_z^2 \rangle$ (left) and $S(0, k)$ (right) on k in the case $L = 10$ (equilibrium *spin* configuration) for initial configurations “D” (solid line), “XH” (dashed line), “ZH” (dash-dotted line), and “R” (dotted line).

“R” initial *spin* configuration are closer to the corresponding values for “D” as compared to “XH”. The opposite is true for thicker cells. Our simulations reveal that for initial conditions “D”, “XH”, and “R” the structural differences decrease on increasing the cell thickness. However, the “HZ” initial *spin* configuration could lead to significantly different structures as Figure 5 reveals. In this case we also observe a pronounced statistical behavior of the system with respect to the “escape” of *spin* configurations along the z -direction. By repeating calculations several times for the same set of parameters we observe that the system either “escapes” or does not and the

extent of this bifurcation behavior increases on approaching the threshold thickness L_c . The reason behind this is thermal fluctuations included in the simulations. As a quantitative measure of the bifurcation extent we set that the “escape” is realized when $\langle S_z^2 \rangle$ ($k = L/2$) exceeds $\langle S_z^2 \rangle_c = 0.1$. Our statistical analysis in the cell $62 \times 62 \times 30$ reveals that the probability for the escape along the z -direction is roughly equal to 40 %.

We also calculated the interaction energy per site of the equilibrium states $E_s = F_{\text{eq}}/(M^2L)$ (see (1)). We have found that it increases slightly with the cell thickness: $E_s = -3.19$,

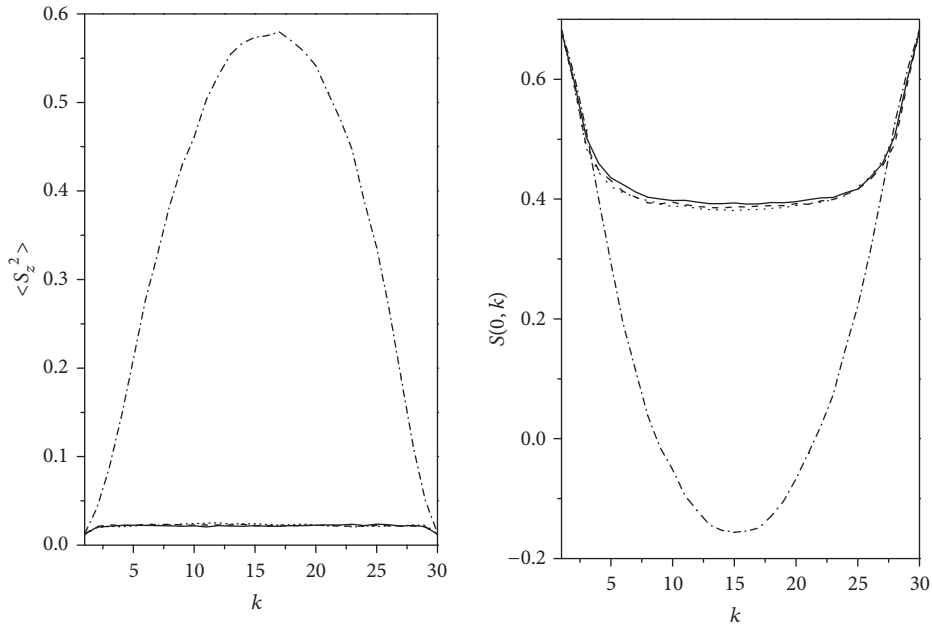


FIGURE 5: Dependence of the plane parameters $\langle S_z^2 \rangle$ (left) and $S(0, k)$ (right) on k in the case $L = 30$ (equilibrium *spin* configuration) for initial configurations “D” (solid line), “XH” (dashed line), “ZH” (dash-dotted line), and “R” (dotted line).

-3.06 , -3.00 , and -2.94 for $L = 10, 15, 20$, and 30 , respectively. The uncertainty of these values due to thermal fluctuations in our simulations is $\delta E_s \sim 0.01$. The quoted energy values must be compared to the energy per site for completely homogeneous state: $E_{\text{hom}} = -3$ since $J = 1$. The smaller energy per site for very thin cells results from relatively strong coupling between the surface and neighbouring spins: $W = 5$. The surface anchoring energy has been included into the total energy and its contribution to the sites at both plates compensates the rise of energy due to inhomogeneity. On the other hand differences in the equilibrium energy for the four different initial configurations for the same L are roughly comparable to fluctuation δE_s .

4. Conclusions

We investigated nematic structures within plane-parallel cells of thickness $h=La_0$ whose bounding plates enforced topologically line-defect patterns. The circular nematic fields at each bounding surface favour surface topological defects bearing $m = 1$ winding number at the centers of the circular patterns. Due to the finite anchoring strength these nucleation sites split and as a result two line defects with $m = 1/2$ emerge from each nucleation site. In order to achieve winding number neutral structure two $m = -1/2$ are formed to compensate the total winding number within each (x, y) plane. In thin cells these defect lines span the bounding plates and their winding number remains the same across the cells. On the other hand in thick cells the defect lines remain confined to the vicinity of the bounding plates. Consequently, they switch the sign of the winding number while linking $m = 1/2$ and $m = -1/2$ daughter nucleation sites. We analysed

structures in the critical region, $L \sim L_c$, where these two different realizations of defect patterns compete. The resulting patterns depend relatively strongly on initial conditions. We imposed four different histories to the nematic cells. We either imposed the surface imposed pattern through whole the cell, homogeneously aligned pattern along the x -axis or z -axis, and isotropic profiles. We label these histories as “D”, “XH”, “ZH”, and “R”, respectively. These patterns could be experimentally imposed. For example, the first pattern is realised in NLC cells below the critical thickness. The second and the third patterns could be realised by using a strong enough spatially uniform electrical field aligned along the x -axis and z -axis, respectively. The fourth profile could be realised by quenching the sample from the isotropic phase. In the case of “ZH” we find behaviour which is reminiscent to the percolation one. In our future study we intend to analyse external electric field driven rewiring of defect patterns in thin ($L < L_c$) and thick ($L > L_c$) cells.

In the studied case we considered substrates imposing four circular “easy axis surface fields”. Note that larger number of circles and different distance between their centers or different arrangement (e.g., hexagonal) would quantitatively affect the results. However, we claim that qualitative structure would be similar. Namely, the key parameter influencing the switching mechanism is the length of disclinations. The crucial parameters are therefore the cell thickness h and the shortest distance between $\pm 1/2$ termination ends of “confined” disclinations.

Furthermore, we considered conditions for which each $m = 1$ surface imposed singularity nucleated a pair of $m = 1/2$ line defects. However, in general also other structural solutions might appear depending on h and the strength

of the surface anchoring interactions. Namely, in our modelling we assume that the confined surfaces locally favour unsplit $m = 1$ defect structure at the defect nucleating sites. On the other hand, bulk elasticity favours formation of defect lines bearing “elementary” (smallest possible) winding numbers, i.e., $|m| = 1/2$. A simple modelling [5] in the approximation of equal nematic elastic constants reveals that the director field dependent elastic free energy cost ΔF_e of a single disclination of strength m within a finite region (characterised by a linear length R) scales as $\Delta F_e \approx F_0 m^2$, where $F_0 = F_0(R)$. Consequently, in bulk a pair of $m = 1/2$ dislocations is energetically more favourable than a single $m = 1$ line defects. Our preliminary simulations (using Landau-de Gennes continuum approach in terms of the tensor nematic order parameter), where we focus on structures emerging from a single $m = 1$ surface imposed singularity, reveal three qualitatively different nematic structures on varying h . For $h \leq h_c^{(1)}$ a single $m = 1$ singularity is most stable. Within the window $h_c^{(1)} \leq h \leq h_c^{(2)}$ a pair of two $m = 1/2$ disclinations appears instead. Furthermore, for $h \geq h_c^{(2)}$ an “escaped” structure corresponds to the global minimum, where the singularity in the director field is avoided by a nonsingular escape of the nematic director field along the 3^{rd} direction [14]. Note that the described behaviour on crossing $h_c^{(2)}$ was already observed experimentally [15, 16]. A more detailed analysis will be published elsewhere.

The observed behavior is reminiscent to the percolation phenomenon. We illustrate this analogy for the simplest case of cubic cell (network) in percolation theory. The cell is divided into small cubes (sites) with two significantly distinct values of some physical quantity. Let us take the usual case of either electrically conducting or insulating sites. The conducting and insulating sites are randomly spatially distributed, so that there is a fraction p of conducting sites. In the vicinity of the percolation threshold p_c and for a finite network there is a probability P that a randomly distributed conducting sites form a conducting (percolation) path between two opposite faces of the entire cube. The percolation threshold p_c is usually defined as the fraction of conducting sites (i.e., the volume fraction of conducting phase) where the percolation probability has the value $P = 50\%$. The percolation threshold p_c is roughly independent on the network size, but the steepness of the monotonically increasing function $P(p)$ around p_c increases with increasing network size [17]. It holds $P = 0$ for $p \ll p_c$, while $P = 100\%$ for $p \gg p_c$. The fraction p in percolation theory plays similar role as the thickness of the NLC cell in our study, and p_c corresponds to the threshold thickness L_c .

Data Availability

The data used to support the findings of this study are available from the corresponding author upon request.

Conflicts of Interest

The authors declare that there are no conflicts of interest regarding the publication of this paper.

References

- [1] D. Dunmur and T. Sluckin, *Soap, Science, and Flat-Screen TVs: A History of Liquid Crystals*, Oxford University Press, Oxford, UK, 2011.
- [2] B. S. Murray, R. A. Pelcovits, and C. Rosenblatt, “Creating arbitrary arrays of two-dimensional topological defects,” *Physical Review E*, vol. 90, Article ID 052501, 2014.
- [3] X. Wang, D. S. Miller, E. Bokusoglu, J. J. Pablo, and N. L. Abbott, “Topological defects in liquid crystals as templates for molecular self-assembly,” *Nature Materials*, vol. 15, p. 106, 2016.
- [4] S. Meiboom, J. P. Sethna, P. W. Anderson, and W. F. Brinkman, “Theory of the blue phase of cholesteric liquid crystals,” *Physical Review Letters*, vol. 46, no. 18, p. 1216, 1981.
- [5] M. Kleman and O. D. Lavrentovich, *Soft Matter Physics*, Springer, Berlin, Germany, 2002.
- [6] O. D. Lavrentovich, “Topological defects in dispersed words and worlds around liquid crystals, or liquid crystal drops,” *Liquid Crystals*, vol. 24, no. 1, pp. 117–126, 1998.
- [7] S. Afghah, R. L. B. Selinger, and J. V. Selinger, “Visualising the crossover between 3D and 2D topological defects in nematic liquid crystals,” *Liquid Crystals*, vol. 45, no. 13-15, pp. 2022–2032, 2018.
- [8] N. Schopohl and T. J. Sluckin, “Defect core structure in nematic liquid crystals,” *Physical Review Letters*, vol. 59, no. 22, p. 2582, 1987.
- [9] A. S. Backer, A. C. Callan-Jones, and R. A. Pelcovits, “Nematic cells with defect-patterned alignment layers,” *Physical Review E: Statistical, Nonlinear, and Soft Matter Physics*, vol. 77, no. 2, Article ID 021701, 2008.
- [10] P. A. Lebowohl and G. Lasher, “Nematic-liquid-crystal order—a monte carlo calculation,” *Physical Review A: Atomic, Molecular and Optical Physics*, vol. 6, no. 1, p. 426, 1972.
- [11] A. Ranjkesh, M. Ambrožič, S. Kralj, and T. J. Sluckin, “Computational studies of history dependence in nematic liquid crystals in random environments,” *Physical Review E: Statistical, Nonlinear, and Soft Matter Physics*, vol. 89, no. 2, Article ID 022504, 2014.
- [12] G. P. Crawford, J. A. Mitcheltree, E. P. Boyko, W. Fritz, S. Zumer, and J. W. Doane, “ K_{33}/K_{11} determination in nematic liquid crystals: An optical birefringence technique,” *Applied Physics Letters*, vol. 60, no. 26, p. 3226, 1992.
- [13] R. D. Polak, G. P. Crawford, B. C. Kostival, J. W. Doane, and S. Žumer, “Optical determination of the saddle-splay elastic constant K_{24} in nematic liquid crystals,” *Physical Review E*, vol. 49, no. 2, p. R978, 1994.
- [14] P. E. Cladis and M. Kleman, “Non-singular disclinations of strength $S = +1$ in nematics,” *Journal de Physique I France*, vol. 40, p. 325, 1979.
- [15] C. Chiccoli, I. Feruli, O. D. Lavrentovich, P. Pasini, S. V. Shiyankovskii, and C. Zannoni, “Topological defects in schlieren textures of biaxial and uniaxial nematics,” *Physical Review E: Statistical, Nonlinear, and Soft Matter Physics*, vol. 66, no. 3, Article ID 030701, 2002.
- [16] B. Murray, S. Kralj, and C. Rosenblatt, “Decomposition vs. escape of topological defects in a nematic liquid crystal,” *Soft Matter*, vol. 45, pp. 8442–8450, 2017.
- [17] D. Stauffer, *Introduction to Percolation Theory*, Taylor & Francis, London, UK, 1985.

Research Article

Influence of Gold Nanoparticles on the Luminescence of an Acrylated Isocyanonaphthalene Derivative

J. Burunkova,¹ S. Keki,² A. Veniaminov ,¹ M. Nagy ,² L. Daroczi ,³ and S. Kokenyesi³

¹ITMO University, Saint Petersburg, Russia

²Department of Applied Chemistry, University of Debrecen, Debrecen, Hungary

³Institute of Physics, University of Debrecen, Debrecen, Hungary

Correspondence should be addressed to M. Nagy; miklos.nagy@science.unideb.hu

Received 9 October 2018; Revised 5 February 2019; Accepted 17 February 2019; Published 4 March 2019

Guest Editor: Hong Fang

Copyright © 2019 J. Burunkova et al. This is an open access article distributed under the Creative Commons Attribution License, which permits unrestricted use, distribution, and reproduction in any medium, provided the original work is properly cited.

Dodecanethiol-functionalized gold nanoparticles were incorporated into the polymer matrix of diurethane-methacrylate monomer mixture in the presence of SiO₂ nanoparticles (8 wt %) and a new reactive organic luminescent material ACAIN (1-N-(2-acryloyloxy-3-chloroprop-1-yl)-amino-5-isocyanonaphthalene, 1 wt %). This way, a new, probably multifunctional, polymer nanocomposite was obtained. It was shown that the addition of SiO₂ nanoparticles enhances the fluorescent intensity of ACAIN by 1.5 times in the 450-550 nm spectral range. Furthermore, an additional fluorescence enhancement up to 4.5 times was observed when Au nanoparticles were added to this nanocomposite in a rather low (0.12 wt %) concentration.

1. Introduction

It is known that the luminescence of organic molecules in the presence of metal nanoparticles can be enhanced or just decreased, in dependence of different factors [1]. The presence of electromagnetic, plasmon field emitted by the proper excited metal nanoparticle can enhance the luminescence of an organic molecule [2]. At the same time the luminescence of the molecule, directly connected to the metal surface, can be essentially decreased because of the resonant transfer of excitation energy to the metal or due to the dissociation of excitons at the interface [3]. In a number of reports the enhancement of luminescence in π -conjugated polymers is related to the changes of polymer structure due to the introduction of metallic nanoparticles [4–6].

It is known that π -conjugated organic systems have been used as optoelectronic and sensing materials due to their characteristic efficient light emission or absorption and p-type charge transport. Hybrid nanostructures of π -conjugated organic systems with nanoscale metals offer surface plasmon- (SP-) enhanced luminescence, which can be applied to organic-based optoelectronics, photonics, and sensing.

The most popular route of metal (for example, Ag) nanoparticle introduction into the polymer matrix consists of the preparation of nanoparticles directly by a certain reduction process. For example, Ag nanoparticles (Ag NPs) can be pre-prepared by sodium citrate reduction and incorporated into agarose by mixing to form an Ag-containing agarose film (Ag@agarose), which yielded a maximum 8.5-fold increase in the fluorescence [7]. However, in a number of applications the selected form and dimensions of the nanoparticles are important, primarily for the determined plasmon resonance peak in the optical excitation and/or absorption spectra. The possibility of the direct introduction of pre-prepared gold nanoparticles to acrylate nanocomposites was shown in our previous paper [8]. Moreover, we recently developed a new reactive solvatochromic dye: 1-N-(2-acryloyloxy-3-chloroprop-1-yl)-amino-5-isocyanonaphthalene (ACAIN), the complexation of which can be used for the selective detection and quantification of silver(I) ions from aqueous media [9]. In addition, ACAIN was found to be a vital cell stain, which could selectively label the tonoplast in plant cells [10]. We assume that the combination of our multifunctional solvatochromic dye with the Au NP containing polymer matrix can be important for sensor applications, since organic

TABLE I: Compositions of the Au-SiO₂-ACAIN monomer composites.

Sample No	Monomers	SiO ₂ NPs [wt %]	Au NPs [wt %]	Initiator [wt %]	ACAIN [wt %]
1	UDMA/IDA=3/7	--	--	0.5 In2	1
2	UDMA/IDA=3/7	8	--	0.5 In2	1
3	UDMA/IDA=3/7	8	0.12	0.5 In2	1
4	UDMA/IDA=3/7	8	-	0.5 In2	-
5	UDMA/IDA=3/7	8	0.12	0.5 In2	-

luminescent materials, which change the characteristics of luminescent spectra under the influence of certain compounds or ions, enable the mass production of cheap sensing elements with the necessary forms and dimensions. Therefore, the increase of luminescence intensity of the markers in the polymeric material with increased stability is an important issue from the practical point of view. Our aim was to enhance the fluorescence of the multifunctional ACAIN and at the same time incorporate it to a polymer matrix, so that it could be used as a starting material for solid state sensors. The introduction of SiO₂ NPs to the polymer should prevent the leaching of luminescent components from the composite. In this paper we present the results on the preparation of an acrylate composite with ACAIN and SiO₂, as well as Au nanoparticles. The influence of Au nanoparticles on the luminescence of this composite film was investigated.

2. Experimental

2.1. Materials. The following materials and chemicals were used in this work: diurethane dimethacrylate, mixture of isomers (436909 Aldrich, UDMA); isodecyl acrylate (408956 Aldrich, IDA); initiator: 2,2-dimethoxy-2-phenylacetophenone (19611-8 Aldrich, In2); dodecanethiol functionalized gold nanoparticles with average size 5 nm (Nanoprobes, No3014, AuNP) SiO₂ nanoparticles with size 7 nm (Aldrich No. 066K0110, SiO₂NP); ACAIN, which is an organic material with the structure shown in Figure 1.

ACAIN was prepared in a two-step reaction according to scheme in Figure 2.

The detailed description of the synthesis and detailed optical characterization of 1-(3-chloro-2-hydroxyprop-1-yl)-amino-5-isocyanonaphthalene (CHAIN) and 1-N-(2-acryloyloxy-3-chloroprop-1-yl)-amino-5-isocyanonaphthalene (ACAIN) can be found in [9]. The compound is a yellow powder at room temperature.

2.2. Preparation of the Au-SiO₂-ACAIN-Monomer Mixtures and the Polymer Nanocomposite Films. The compositions of the Au-SiO₂-ACAIN monomer mixtures are presented in Table I and the preparation procedure is as follows: silicon oxide nanoparticles were added to the above-mentioned monomers and homogeneous solution was prepared by sonication. After homogenization the proper amount of ACAIN powder was mixed in and the solution of Au NP in toluene and initiator (0.5 wt % In2) were added to this solution and

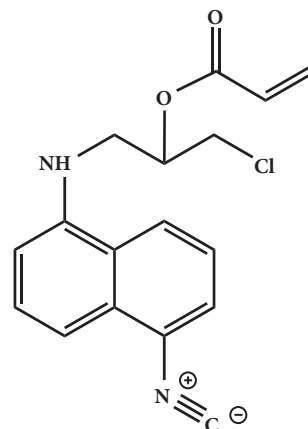


FIGURE 1: The molecular structure of 1-N-(2-acryloyloxy-3-chloroprop-1-yl)-amino-5-isocyanonaphthalene (ACAIN).

carefully mixed. Next the solvent, toluene, was evaporated until constant weight of the nanocomposite.

Preparation of the Polymer Nanocomposite Films. Preparation of the polymer nanocomposite films consists of the UV-curing of the monomer solutions between glass and polyester film to prevent the inhibiting effect of oxygen. The UV light source was a mercury lamp OSRAM, HQV 125 W. 20-30 μ m thick nanocomposite samples were formed on a glass substrate in the gap between the glass and a polyester film, as shown in Figure 3(a). The polyester film was removed after the UV-curing. The SEM picture of the cross-section of the sample is presented in Figure 3(b).

2.3. Experimental Measurements. Optical transmission spectra of the obtained polymer nanocomposites were recorded on a Shimadzu 1800 UV-vis spectrometer. Luminescence spectra were investigated by the scanning laser microscope Zeiss LSM-710 with pumping light wavelength at 405 nm (excitation) and 3 nm spectral steps. The structure of the nanocomposites containing Au NPs was characterized by TEM (JEM-2000FXII).

3. Results and Discussion

For practical applications the uniform distribution of the Au NPs in the polymer matrix is an important issue. Therefore, using transmission electron microscopy first we showed

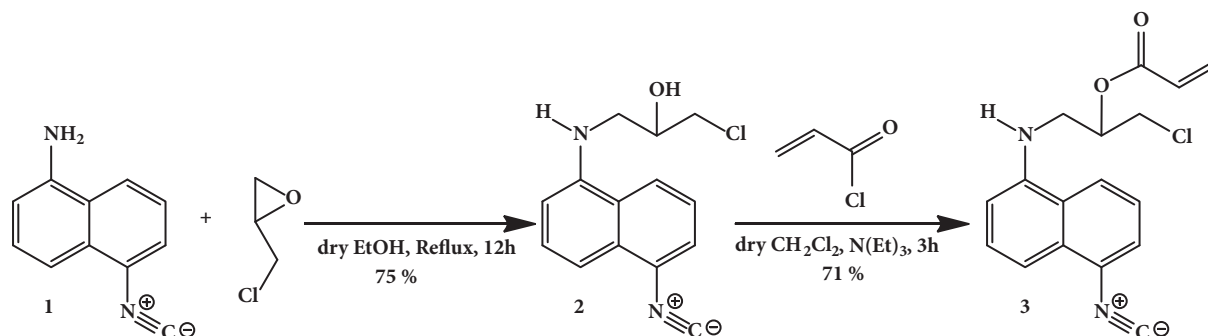


FIGURE 2: Synthesis of 1-(3-chloro-2-hydroxyprop-1-yl)-amino-5-isocyanonaphthalene (2, CHAIN) and 1-(2-acryloyloxy-3-chloro-prop-1-yl)-amino-5-isocyanonaphthalene (3, ACAIN).

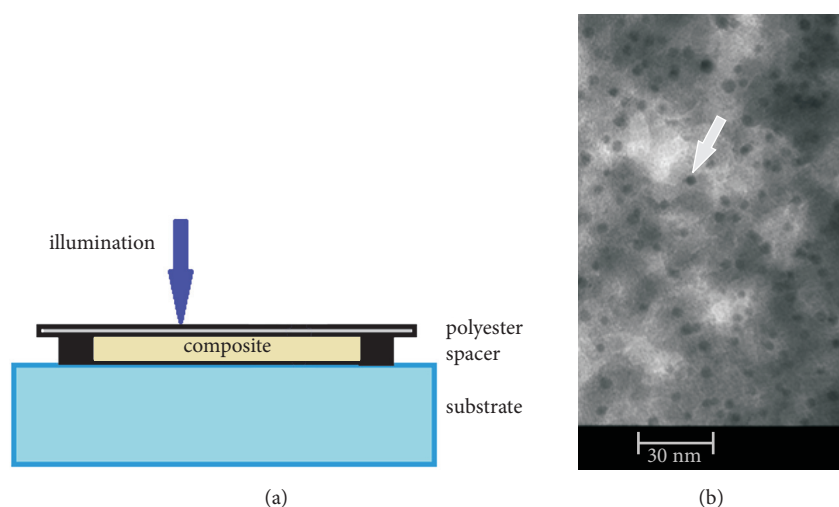


FIGURE 3: (a) Scheme of sample preparation. The polyester film is removed after polymerization. (b) TEM picture of Au NPs (the white arrow selects one) in the polymer matrix, Sample 3.

directly that the Au NPs are well distributed in the matrix and do not agglomerate (see Figure 3(b)). The absence of agglomeration was further supported by the presence of the plasmon resonance absorption peak near ~ 540 nm (see Figure 4), corresponding to the dimensions of the Au NPs (~ 5 nm).

Since ACAIN contains a reactive acrylate functional group, we assumed its complete incorporation in the polymer matrix during the photopolymerization process. The uniform fluorescent color of the polymer films backed this assumption. Optical absorption spectra of pure acrylate composites with 1 wt % of ACAIN and with the addition of two types of nanoparticles (Au NPs and SiO_2 nanoparticles) were measured (Figure 4). The ACAIN absorption maximum for all composites, shown in Table 1, is located near 350 nm (Figure 4). The introduction of 8 wt % of SiO_2 nanoparticles and 0.12 wt % of Au nanoparticles results in the increase of the absorption maximum and its small, about 10 nm shift towards shorter wavelengths. These phenomena may be caused by the formation of a complex between the SiO_2 NPs and ACAIN, which similarly to other cases [11, 12] could also prevent the possible leach out of the luminescent component. It should

also be noted that the addition of the NPs does not change the absorption maximum, essentially.

That is why in our experiments the luminescence was excited at the longwave-side of this maximum, at 405 nm. It is important to note that the introduction of Au NPs results in the appearance of an absorption peak with a maximum at ~ 540 nm, which is related to the resonant absorption of the localized plasmons in the Au NPs.

The photoluminescence spectra of the above-mentioned composites are presented in Figure 5. It was established that the pure polymer matrix (composite 4) and the polymer composite with Au and SiO_2 NPs (composite 5) were not luminescent, while the introduction of ACAIN stimulated a strong luminescence signal. The last spectrum has wide asymmetrical band shapes with small maxima features at 460 and 490 nm for the ACAIN polymer composite without and with SiO_2 nanoparticles, respectively. These spectra have similar shapes as is characteristic for naphthalene derivatives, for example, described in [13]; however the maxima are essentially shifted to the red spectral range, which can be explained by the presence of the $\text{N}\equiv\text{C}$ group in the ACAIN structure. It was established, as presented in Figure 5, that the introduction

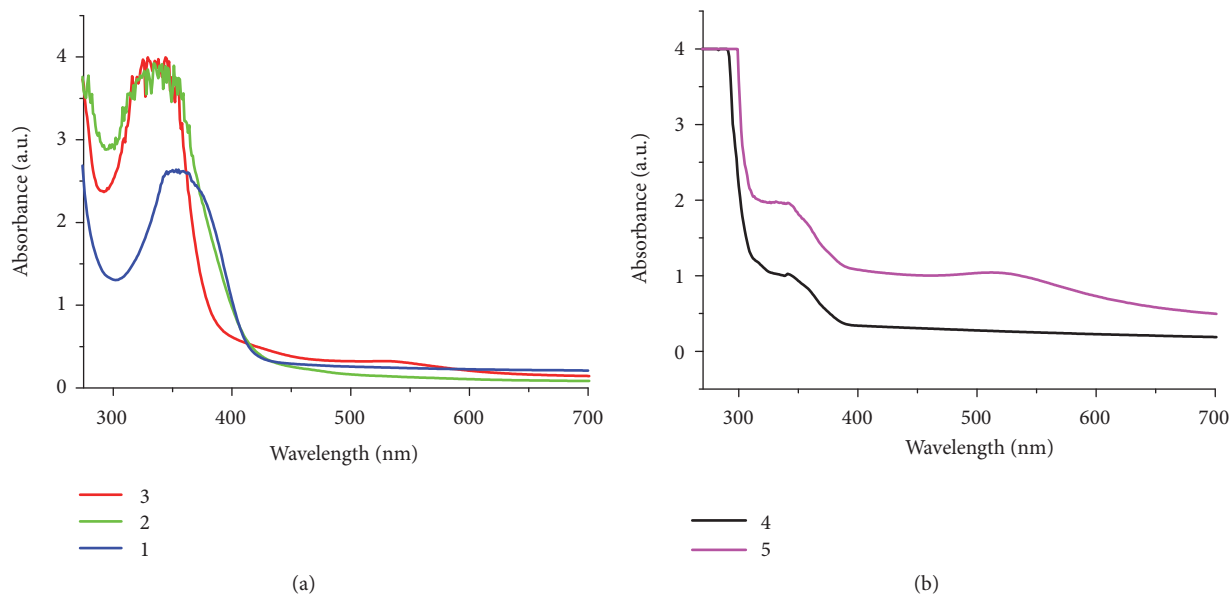


FIGURE 4: Optical absorption spectra of the ACAIN-containing (compositions 1-3) and polymer films without ACAIN (compositions 4,5).

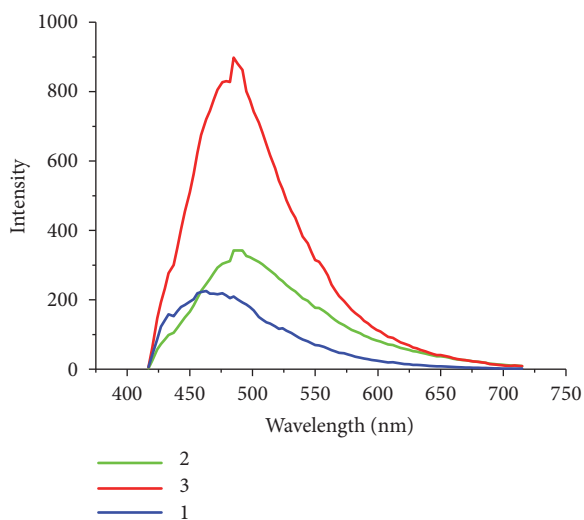


FIGURE 5: Luminescence spectra of the ACAIN-containing polymer films, compositions 1, 2, and 3.

of the SiO₂ nanoparticles to the UDMA/IDA/ACAIN composite increased the luminescence intensity by 1.5 times, and the addition of Au NPs/SiO₂ results in a 4.5-time increase in the intensity of luminescence. Besides the positive role of SiO₂ NPs described in refs. [11, 12] and the similar influence on ACAIN molecules in our materials, the essential role of Au NPs can be attributed to the generation of plasmon fields, which are localized near the Au NPs, causing an efficient interaction with the luminescent molecules. Both phenomena may cause the observed shift of the ACAIN luminescence maximum towards longer wavelengths in comparison with the empty polymer matrix only.

It is quite possible that in our case a donor-acceptor type complex formation occurs between ACAIN and the Au NPs, since the gold nanoparticles possess positive charge at the surface and the isocyanonaphthalene acrylate derivatives are considerably dipolar owing to the presence of the electron donating amino and the electron withdrawing isocyano groups, as it is seen in the ACAIN structure (Figure 1). The possibility of such complex formation was shown in our previous paper [14]. Under the influence of 450-550 nm luminescence, the localized plasmon can be excited at the short wavelength wing of the resonant peak and enhance the luminescence of the organic derivative, although with much less efficiency than in the resonance case. The effect is due to the known localized plasmon (LP) coupling and the local near-field enhancement of optical transitions. Tailoring Au NP size and concentration in such nanocomposites is expected to be used for the design and development of high-performance luminescent materials and functional components. In this case the application of preformed particles, as proposed in this paper, is preferable.

The enhancement of luminescence can be better at double-wavelength excitation, which includes the resonant excitation of localized plasmons in the given type of Au NPs. But in our case an interesting mechanism of luminescence enhancement may be proposed: self-excitation with positive feedback. In this mechanism the luminescence excites plasmon resonance, which in turn enhances the luminescence. Further investigations are in progress in this attractive direction.

4. Summary

Polymer nanocomposites were fabricated by direct introduction of preformed SiO₂ and Au NPs with concentrations 8 wt % and 0.12 wt %, respectively, into the mixture of

acrylate monomers, which contain also a new luminescent isocyanonaphthalene based material, ACAIN. Resonant plasmon absorption was observed in these nanocomposites; i.e., gold nanoparticles were separated and localized plasmon fields can be generated by illumination. The luminescence of ACAIN was essentially enhanced to 4.5 times of the original in such nanocomposites, as a result of a plasmon-assisted process, which can also be explained by a self-exciting process with a positive feedback.

Data Availability

The original data used to support the findings of this study are available from the corresponding and/or first author at burunj@list.ru, upon request.

Conflicts of Interest

The authors declare that they have no conflicts of interest.

Acknowledgments

This work was financially supported by the grants K-116465 and GINOP-2.3.2-15-2016-00041 given by NFKI (National Research, Development and Innovation Office, Hungary). The work/publication is supported by the EFOP-3.6.1-16-2016-00022 project. The project is cofinanced by the European Union and the European Social Fund. Furthermore, this paper was also supported by the János Bolyai Research Scholarship of the Hungarian Academy of Sciences (Miklós Nagy).

References

- [1] O. G. Tovmachenko, C. Graf, D. J. Van Den Heuvel, A. Van Blaaderen, and H. C. Gerritsen, "Fluorescence enhancement by metal-core/silica-shell nanoparticles," *Advanced Materials*, vol. 18, no. 1, pp. 91–95, 2006.
- [2] J. B. Khurgin and G. Sun, "Enhancement of optical properties of nanoscaled objects by metal nanoparticles," *Journal of the Optical Society of America B: Optical Physics*, vol. 26, no. 12, p. B83, 2009.
- [3] E. Dulkeith, A. C. Mortcani, T. Niedereichholz et al., "Fluorescence quenching of dye molecules near gold nanoparticles: radiative and nonradiative effects," *Physical Review Letters*, vol. 89, no. 20, Article ID 203002, 2002.
- [4] P. G. Nicholson, V. Ruiz, J. V. Macpherson, and P. R. Unwin, "Hybrid nanostructures using p-conjugated polymers and nanoscale metals: synthesis, characteristics, and optoelectronic applications," *Chemical Communications*, vol. 8, p. 1052, 2005.
- [5] D. H. Park, M. S. Kima, and J. Jinsoo, "Hybrid nanostructures using π -conjugated polymers and nanoscale metals: Synthesis, characteristics, and optoelectronic applications," *Chemical Society Reviews*, vol. 39, pp. 2439–2452, 2010.
- [6] B. K. Kuila, A. Garai, and A. K. Nandi, "Synthesis, optical, and electrical characterization of organically soluble silver nanoparticles and their poly(3-hexylthiophene) nanocomposites: Enhanced luminescence property in the nanocomposite thin films," *Chemistry of Materials*, vol. 19, no. 22, pp. 5443–5452, 2007.
- [7] X. Wang, F. He, X. Zhu, F. Tang, and L. Li, "Hybrid silver nanoparticle/conjugated polyelectrolyte nanocomposites exhibiting controllable metal-enhanced fluorescence," *Scientific Reports*, vol. 4, article no. 4406, 2014.
- [8] J. Burunkova, S. Kokenyesi, I. Csarnovics, A. Bonyár, M. Veres, and A. Csik, "Influence of gold nanoparticles on the photopolymerization processes and structure in acrylate nanocomposites," *European Polymer Journal*, vol. 64, pp. 189–195, 2015.
- [9] M. Nagy, D. Rácz, Z. L. Nagy et al., "An acrylated isocyanonaphthalene based solvatochromic click reagent: optical and biolabeling properties and quantum chemical modeling," *Dyes and Pigments*, vol. 133, pp. 445–457, 2016.
- [10] M. Nagy, S. Kéki, D. Rácz et al., "Novel fluorochromes label tonoplast in living plant cells and reveal changes in vacuolar organization after treatment with protein phosphatase inhibitors," *Protoplasma*, vol. 255, no. 3, pp. 829–839, 2018.
- [11] S. Santra, K. Wang, R. Tapeç, and W. Tan, "Development of novel dye-doped silica nanoparticles for biomarker application," *Journal of Biomedical Optics*, vol. 6, no. 2, pp. 160–166, 2001.
- [12] G. Canton, R. Riccò, F. Marinello, S. Carmignato, and F. Enrichi, "Modified Stöber synthesis of highly luminescent dye-doped silica nanoparticles," *Journal of Nanoparticle Research*, vol. 13, no. 9, pp. 4349–4356, 2011.
- [13] F. Qu, J. Liu, H. Yan, L. Peng, and H. Li, "Synthesis of organic nanoparticles of naphthalene-thiourea-thiadiazole-linked molecule as highly selective fluorescent and colorimetric sensor for Ag(I)," *Tetrahedron Letters*, vol. 49, no. 52, pp. 7438–7441, 2008.
- [14] J. Burunkova, M.-J. Ohoueu, I. Csarnovics, M. Veres, A. Bonyár, and S. Kokenyesi, "Peculiarities of interaction of gold nanoparticles with photoinitiators in polymer nanocomposites for holographic recording," *Journal of Photochemistry and Photobiology A: Chemistry*, vol. 359, pp. 111–120, 2018.

Research Article

Effect of Deposition Time on the Optoelectronics Properties of PbS Thin Films Obtained by Microwave-Assisted Chemical Bath Deposition

Enue Barrios-Salgado ¹, Y. Rodríguez-Lazcano ¹, Juan Pablo Pérez-Orozco,² J. Colin,³ P. Altuzar,⁴ J. Campos ⁴, and David Quesada⁵

¹Unidad Académica de Ciencias Básicas e Ingenierías, Universidad Autónoma de Nayarit, Ciudad de la Cultura “Amado Nervo” S/N, 63155, Tepic, NAY, Mexico

²Departamento de Ingeniería Química y Bioquímica, Instituto Tecnológico de Zacatepec, Tecnológico Nacional de México, Calzada Tecnológico #27, Col. Centro, 62780, Zacatepec, MOR, Mexico

³Facultad de Ciencias Químicas e Ingeniería, Universidad Autónoma del Estado de Morelos, Av. Universidad 1001, Col. Chamilpa, 62209, Cuernavaca, MOR, Mexico

⁴Instituto de Energías Renovables, Universidad Nacional Autónoma de México, 62580, Temixco, MOR, Mexico

⁵Department of Mathematics, Miami Dade College, Wolfson Campus, Miami, FL 33132, USA

Correspondence should be addressed to Y. Rodríguez-Lazcano; yamilet.lazcano@uan.edu.mx

Received 26 November 2018; Revised 5 February 2019; Accepted 13 February 2019; Published 3 March 2019

Guest Editor: Hong Fang

Copyright © 2019 Enue Barrios-Salgado et al. This is an open access article distributed under the Creative Commons Attribution License, which permits unrestricted use, distribution, and reproduction in any medium, provided the original work is properly cited.

PbS thin films with thickness between 100 and 150 nm were grown for the first time by microwave-assisted chemical bath deposition in a commercial automated system with deposition times not exceeding 5 min. X-ray diffraction analysis shows that the thin films have cubic rock salt type structure with good crystallinity. The grain size increased from 18 to 20 nm, as the deposition time increased. Energy dispersive X-ray results confirm that the films are stoichiometric. Optical measurements show that thin films have relatively high absorption coefficients between 10^4 and 10^5 cm⁻¹ in the visible range. In addition, the films exhibit a direct gap, within the energy range from 1.0 to 1.35 eV. The electrical properties, such as conductivity, the Seebeck coefficient, carrier concentration, and carrier mobility, are discussed.

1. Introduction

Lead sulfide (PbS) is an important IV–VI semiconductor material with technological applications including infrared detectors [1] and absorbers in thin film solar cells [2, 3]. Different methods have been used to synthesize PbS; they include chemical bath deposition (CBD) [4, 5], spray pyrolysis [6], pulsed laser deposition [7], vacuum evaporation [8], chemical vapor deposition (CVD) [9], ultrasound [10], and electrodeposition [11].

Studies of PbS thin films obtained by CBD showed that this compound has a band gap (E_g) within the range of energies from around 1.39–1.55 to 2.38–2.75 eV, an electrical resistivity of $10^5 \Omega$ cm, and a preference orientation along

the (111) or (200) planes with grain sizes about 20 or 34 nm depending on the temperature and/or formulation used [5, 12, 13]. The authors in [14] prepared PbS films by CBD at room temperature for different deposition times (from 60 to 300 min) using lead acetate as a source of Pb ions, thiourea to produce S ions, and triethanolamine as the complexing agent in water. As a result, grown films showed that E_g decreases from 0.52 to 0.38 eV, as deposition time increases.

Besides the traditional set-up for CBD, PbS thin films have been also deposited by CBD under the influence of UV radiation [14] and microwave radiation [15–19]. Nanocrystalline PbS thin films have been reported using a microwave-assisted chemical bath deposition method with deposition times from 30 to 120 min showing a p-type conductivity

[15]. X-ray diffraction patterns show cubic rock salt (NaCl) structure with preference crystalline orientation along (111) or (200) depending on the deposition time. Moreover, as the deposition time increases, the particle size increases from 13 to 23 nm, while both the electrical resistivity and the band gap E_g decrease from 380 to 347 Ω cm and from 2.7 to 1.6 eV, respectively. The synthesis of PbS nanocrystals in an ethanol solvent for 20 min by microwave heating was reported in [16] with size around 10 nm approximately. Additionally, the pure cubic phase of PbS nanocrystals has been grown by applying a microwave radiation for 30 min using ethanol, distilled water, ethylene glycol, and polyethylene glycol-200 as solvents and lead acetate and thiourea as lead and sulfur sources, respectively [17]. These films show a direct transition with an optical band gap of 3.49 eV. The nanoparticles of PbS were prepared in a domestic microwave oven with different sulfur sources and $\text{Pb}(\text{NO}_3)_2$ as lead source [18].

The microwave-assisted chemical bath deposition (MA-CBD) is a simple, quite fast, and energy-efficient method to obtain thin films [20]. The heating is generated from inside the solution through microwave irradiation, which causes a homogenous distribution of temperature within the solution and accelerates the growth rate by accelerating the film's reaction kinetics [21, 22].

As far as we know, this is the first time that thin films of PbS are reported to be grown by MA-CBD with deposition times not exceeding 5 min in a commercial automated system. In this work, the PbS thin films were synthesized using thioacetamide as sulfur source at different deposition times. The structural, optical, and electrical properties of the thin films were analyzed.

2. Materials and Methods

2.1. Thin Film Deposition. PbS thin films were grown by microwave-assisted chemical bath deposition, following the chemical formulation reported previously [23]. A solution containing 5 ml of $\text{Pb}(\text{NO}_3)_2$ 1 M, 20 ml of NaOH 1 M, 6 ml of CH_3CSNH_2 1 M, 4 ml of $(\text{HOCH}_2\text{CH}_2)_3\text{N}$ 1 M, and distilled water was prepared. Typical microscope glass slides were cut to obtain 75 x 8 x 2 mm substrates. One substrate was introduced each time into the vial containing the chemical solution. Then, the vial was placed in the Anton Paar Microwave Synthesis Reactor Monowave 300 (2.4 GHz). The deposition was carried out at 40°C for 2, 3, and 4 min. Finally, the samples were taken out of the solution and washed with distilled water. The thicknesses of the films were 100, 130, and 150 nm for 2, 3, and 4 min, respectively.

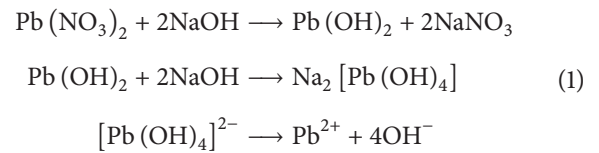
2.2. Characterization. Films' thickness was measured on an XP-200 Ambios Technology profilometer. X-ray diffraction (XRD) patterns were recorded with Cu-K_α radiation on a Rigaku Ultima IV diffractometer with grazing incidence of 1.0° with the sample plane. A field effect scanning electron microscope, Hitachi-FESEM S-5500, was used to analyze the surface morphology of the films. Chemical composition was analyzed in an Oxford x-act energy dispersive X-ray spectrum (EDX) analyzer attached to a Hitachi-SEM SU1510.

Optical transmittance and specular reflectance spectra were measured in a JASCO V-670 spectrometer using air or an aluminized mirror as reference, respectively. For the electrical measurements we used a Keithley 230 programmable voltage source and a Keithley 619 electrometer. A pair of carbon electrodes (5 mm length and 5 mm separation) were painted on the film surface, at which the I-V characteristics have ohmic behavior. Photocurrent response curves were done with a bias (V) of 10 V applied across the electrodes. The current (I) in the sample is recorded at each 0.5 s for the first 20 s in the dark, the next 20 s under 1000 W/m^2 provided by a tungsten halogen lamp, and the last 20 s after switching off the illumination. Thermoelectric measurements were done by a microvoltmeter/scanning thermometer Keithley 740 and the DC power supply with two Peltier elements to establish a difference of temperature. The activation energy for the electrical conductivity was evaluated in the temperature range between 298 and 363 K.

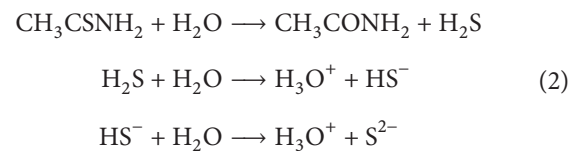
3. Results and Discussion

3.1. Reaction Mechanism. The reaction mechanism for forming PbS thin films is as follows:

Pb^{2+} ions result from $\text{Pb}(\text{NO}_3)_2$, through the reactions shown below [24]:



Additionally, the hydrolysis of thioacetamide, CH_3CSNH_2 , takes place in the solution which releases S^{2-} ions as follows [25]:



When the ionic product of Pb^{2+} and S^{2-} ions exceeds the solubility product of PbS (1.1×10^{-29}), the insoluble solid PbS precipitate is produced:



Microwave radiation used for the MA-CBD provides the necessary energy for the PbS formation. While describing the kinetics of the reaction, it is worth noticing that the heating is due to the interaction of the microwave radiation with the solution through two mechanisms [26, 27]. These mechanisms are related to the interaction of the microwave radiation with the ionic medium and with the polar solvent, that is, the water, which leads to a homogeneous distribution of the temperature inside the solution, not only accelerating the formation of the nuclei of PbS but also stimulating the growth of the crystals.

TABLE 1: Structural parameters as a function of deposition time.

Sample	2θ (deg)	FWHM (deg)	Grain size (nm)	Lattice constant (Å)	Interplanar spacing (Å)
2 min	30.01	0.4757	18.0	5.95	2.967
3 min	30.08	0.4303	19.9	5.94	2.970
4 min	30.05	0.4213	20.3	5.94	2.973

TABLE 2: Atomic percent of PbS thin films.

Sample	Atomic %	
	Pb	S
2 min	49.82	50.18
3 min	49.09	50.91
4 min	49.25	50.75

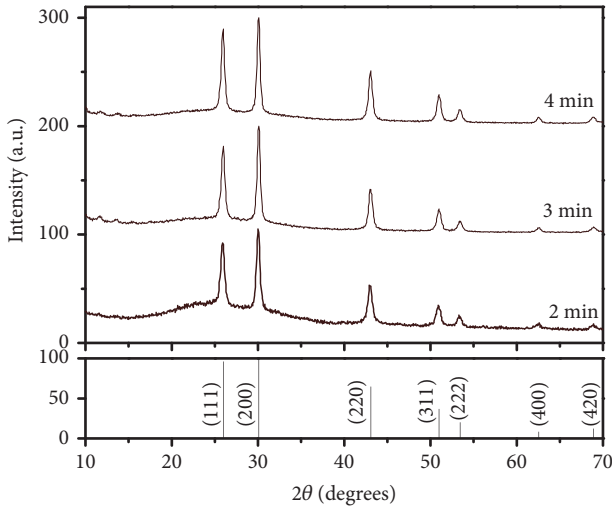


FIGURE 1: XRD patterns of PbS thin film as a function of deposition time.

3.2. Structural Properties. Figure 1 shows the X-ray diffraction patterns of the PbS thin films deposited by the MA-CBD technique at 40°C on glass substrates during 2, 3, and 4 min. XRD patterns clearly have diffraction peaks at 25.96° , 30.06° , 43.01° , 50.90° , 53.37° , 62.54° , and 68.90° which correspond to the (111), (200), (220), (311), (222), (400), and (420) Miller planes of cubic structure (Galena) PbS (PDF# 077-0244), respectively. These results indicate that the films are crystalline with cubic rock salt (NaCl) type structure.

The crystallite size (D) was calculated from the XRD spectrum using Scherrer's equation [28]:

$$D = \frac{0.94\lambda}{\beta \cos \theta}, \quad (4)$$

where θ is the Bragg diffraction angle, λ is the wavelength of X-ray radiation, and β is the full-width at half-maximum (FWHM) of the main peak (200) in the XRD pattern.

An increase in the grain size is observed as the deposition time increases. This leads to an improvement in the crystallinity of the samples. In addition, the FWHM of PbS

thin films decreases with increasing deposition time, which supports the observed increase in crystallinity. These results are presented in Table 1.

The interplanar spacing (d) was taken from the (200) plane using the XRD equipment software. As can be seen in Table 1, the calculated interplanar spacing values are in good agreement with the 2.967 Å reported in the standard PDF# 077-0244.

The lattice constant, a , of the films for the cubic structure was calculated using the equation [29]

$$\frac{1}{d^2} = \frac{h^2 + k^2 + l^2}{a^2}, \quad (5)$$

where h , k , and l are the Miller indices and d is the interplanar spacing. The values of lattice constant are shown in Table 1. It is found that the lattice constant values obtained are in agreement with $a = 5.934$ Å as reported in PDF# 077-0244.

3.3. Surface Morphology and Chemical Composition. Figure 2 shows the SEM images of PbS thin films grown for 2, 3, and 4 min. The micrographs show granular structure with well-defined grain boundaries. Additionally, the films display homogenous surface morphology without microcracks and pinholes.

The characteristic peaks of S- K_α at 2.307 keV, Pb-M at 2.342 keV, and Pb-L $_\alpha$ at 10.550 keV are identified in the EDX spectra of the thin films along with those arising from the substrate (Na- K_α at 1.04 keV, Mg- K_α at 1.253 keV, Al- K_α at 1.486 keV, Si- K_α at 1.74 keV, and Ca- K_α at 3.69 keV).

According to the elemental analysis obtained by EDX, the films are close to the stoichiometric formula of PbS, where the Pb:S ratio is 1:1. The composition of PbS films is shown in Table 2. Figure 3 shows the EDX spectrum of a thin PbS film grown for 2 min.

3.4. Optical Properties. Figure 4 shows the optical transmittance (T) and specular reflectance (R) for PbS thin films. The optical absorption coefficient (α) as a function of the photon energy ($h\nu$) was estimated from the transmittance and reflectance spectra data and film thickness (d) by considering

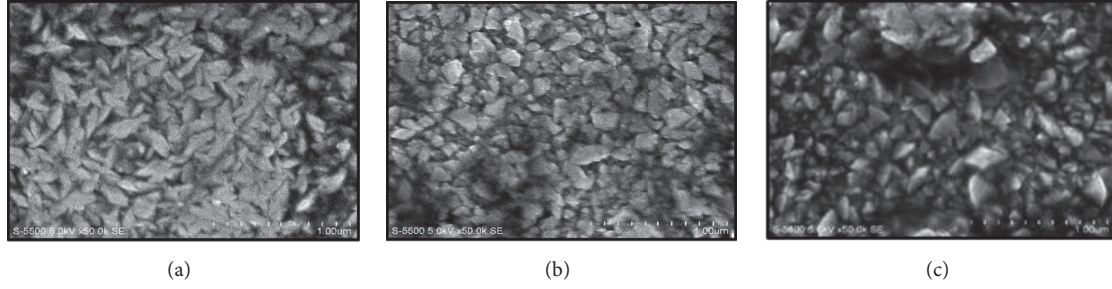


FIGURE 2: SEM images of PbS thin film grown for (a) 2 min, (b) 3 min, and (c) 4 min.

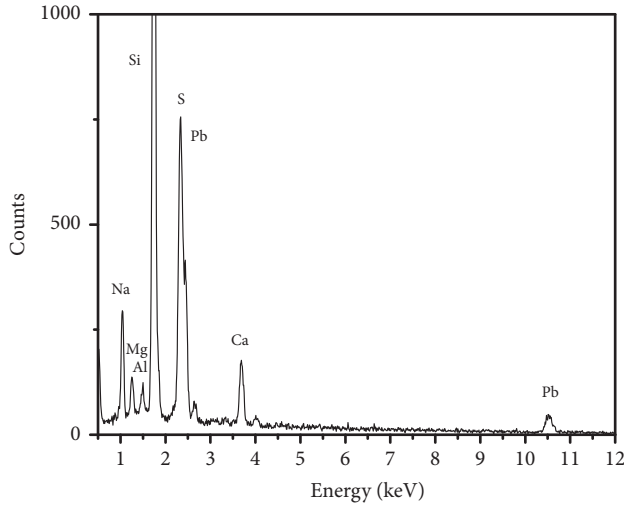


FIGURE 3: EDX spectrum of the PbS thin film grown for 2 min.

multiple reflections within the thin film, according to the following equation [30]:

$$\alpha = \frac{1}{d} \ln \left\{ \frac{(1-R)^2}{2T} + \left[\left(\frac{(1-R)^2}{2T} \right)^2 + R^2 \right]^{1/2} \right\}. \quad (6)$$

Figure 5 shows the optical absorption coefficient (α) of the PbS thin films. Plots of $(\alpha h\nu)^{2/3}$ versus $h\nu$ were used to calculate the energy values of the band gap by the linear fitting of the experimental data, as shown in the inset of Figure 4. The straight line region in this plot indicates that the absorption edge corresponds to a direct forbidden electronic transition as reported for PbS thin films grown by chemical bath deposition [31]. To understand the type of electronic transition which occurs during the optical absorption, $(\alpha h\nu)^2$ versus $h\nu$ was also plotted. The best fit is obtained for $(\alpha h\nu)^{2/3}$ versus $h\nu$ with a correlation factor of 0.99, while for plots of $(\alpha h\nu)^2$ versus $h\nu$ the correlation factor decreases to 0.92 or less. Hence our experimental results suggest that optical band gap in PbS thin films has a direct band gap and forbidden electronic transitions taking place during the optical absorption [32].

The value of E_g was obtained when the adjusting line tends to zero ($\alpha \rightarrow 0$). Values of $\alpha > 10^4 \text{ cm}^{-1}$ were obtained

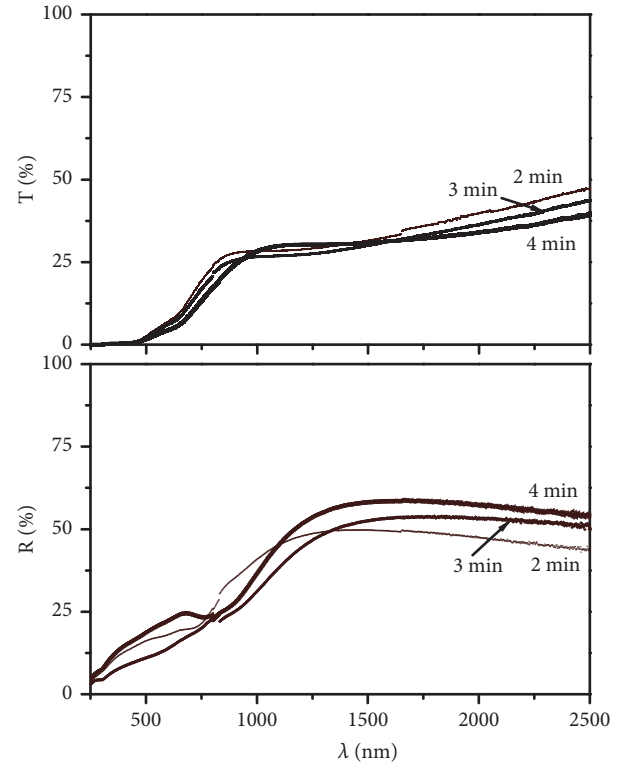


FIGURE 4: Transmittance (T) and reflectance (R) spectra for the PbS thin films at different thicknesses.

for the thin films, as displayed in Figure 4. The optical band gap values of the PbS thin films calculated were 1.35, 1.16, and 1.0 eV for 2, 3, and 4 min, respectively. The E_g value decreases with an increase in time deposition and this is likely to be attributed to an increase in crystal size, as is displayed in Table 1. Band gap values are in agreement with the values reported in the literature [5, 14].

3.5. Electrical Properties. Photoconductivity response curves of the films are shown in Figure 6. All the samples are slightly photoconductive. Electrical conductivity (σ) was estimated from the current and voltage values, the electrode geometry, and the film thickness. PbS thin films show a decrease in dark conductivity with an increase in time deposition. In polycrystalline semiconductors, the conductivity depends on

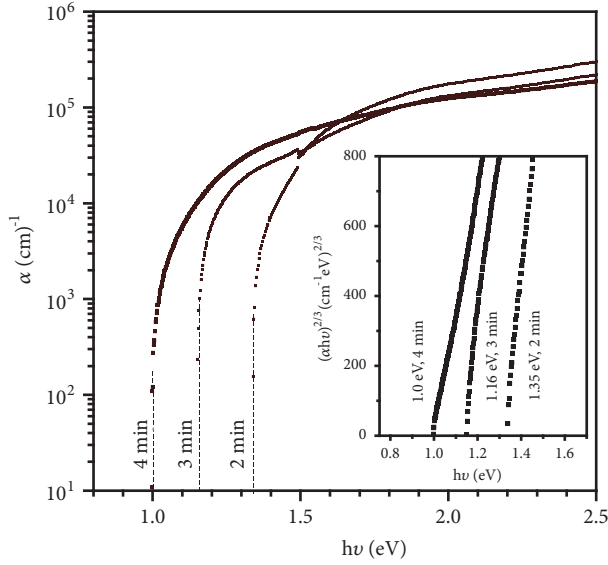


FIGURE 5: Optical absorption coefficient (α) of PbS thin films. Inset shows optical band gap values.

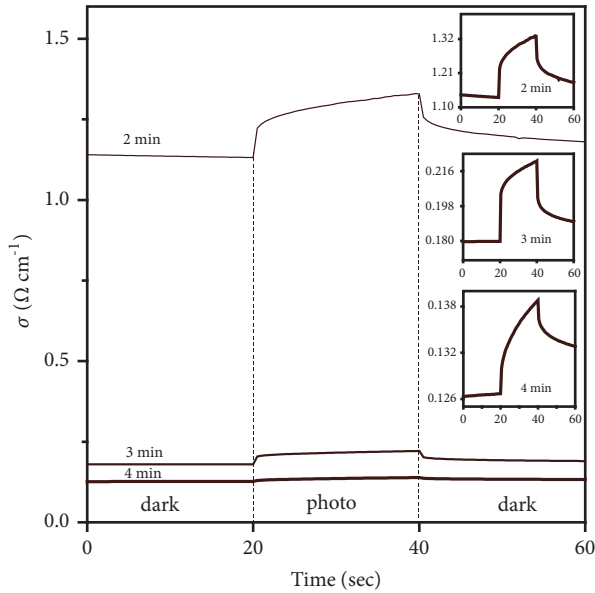


FIGURE 6: Electrical conductivity of PbS thin films. Inset shows the photoconductivity rise and decay.

three factors: (i) density of carriers, (ii) mobility, and (iii) potential barrier at the grain boundaries [33, 34]. Despite the absence of Kelvin probe force microscopy (KPFM) measurements of the films in this current communication, a comparison with other semiconducting polycrystalline systems led us to elaborate on potential causes behind the drop in conductivity [35–38]. The carrier conductivity of the samples might be analyzed assuming the “polycrystalline model,” where carriers pass over back-to-back Schottky barriers that are generated by traps at grain boundaries (GB) via thermionic emission. These traps (charged defect states at GB) might result from impurities segregated during the thin

film growth process. Moreover, for small grains, the mean free path of carriers is expected to be smaller than the width of barriers, and effects of carrier diffusion should play out also. Table 3 displays the values of electrical conductivity.

The Seebeck coefficients, S ($\mu\text{V K}^{-1}$), calculated from the thermoelectric measurements, are presented in Table 3. For all samples S is positive, indicating p-type conductivity. The Seebeck coefficient and the electrical conductivity are linked through an inverse relation [39]; i.e., the lower σ , the higher its S .

Hole concentration (p) was calculated through the following relation [40]:

$$S = \frac{k_B}{e} \left[\frac{5}{2} - s + \ln \frac{N_V}{p} \right], \quad (7)$$

where S is the Seebeck coefficient, s is the parameter which describes the scattering processes in the semiconductors, N_V is related to the density of states in the valence band, k_B is the Boltzmann constant, and e is the electron charge. According to the literature we assume the values of s as $5/2$ and N_V as 10^{24} m^{-3} [39, 41]. Additionally, hole mobility (μ_p) was calculated from the relation between the conductivity and the hole concentration. Table 3 presents these results. The obtained results of μ_p for PbS thin films are in agreement with the value of $0.03 \times 10^{-2} \text{ m}^2 \text{ V}^{-1} \text{ s}^{-1}$ reported previously [31].

The relationship between the electrical conductivity and temperature is governed by the following equation [30]:

$$\sigma(T) = \sigma_o \exp\left(-\frac{E_a}{k_B T}\right), \quad (8)$$

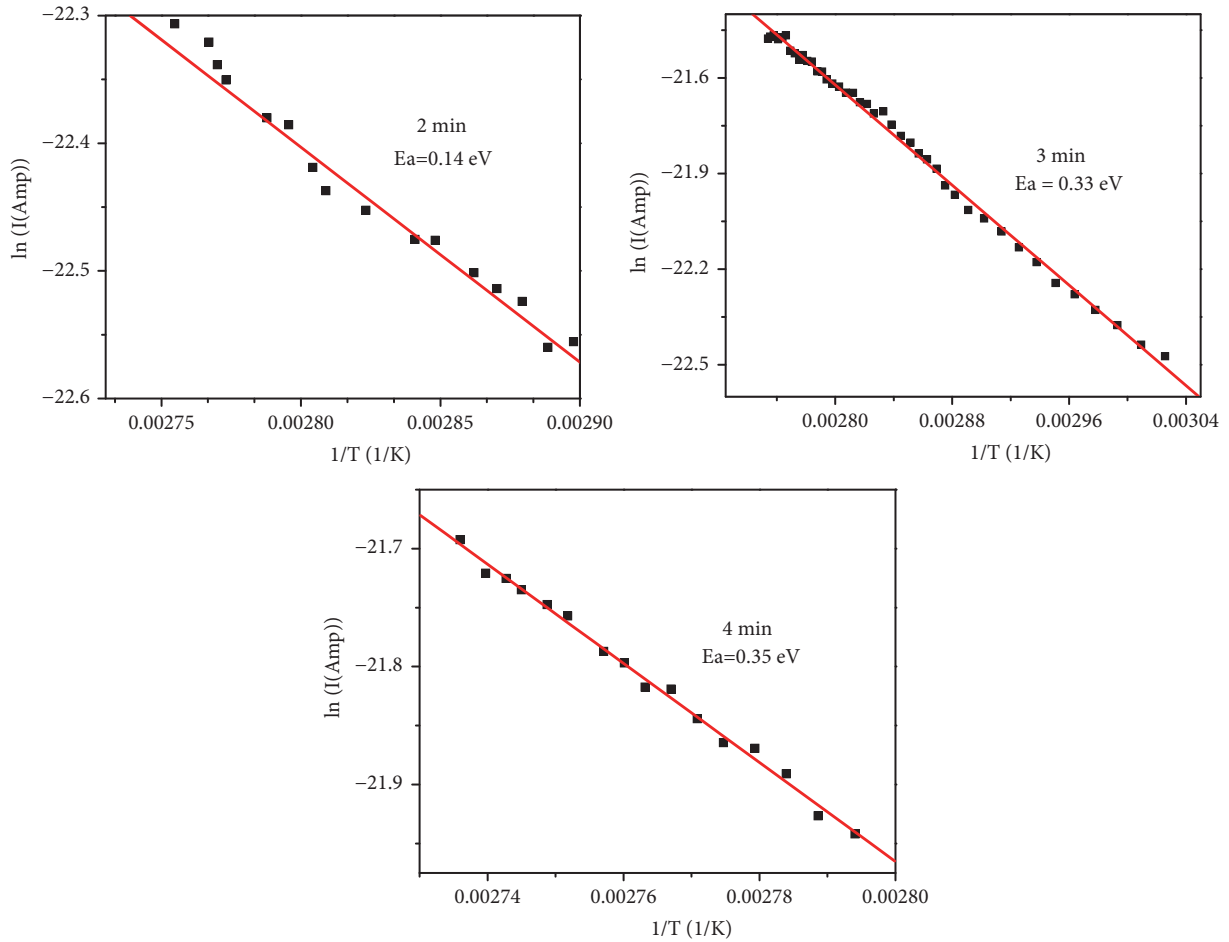
where σ_o is a parameter whose value depends on the semiconducting material, E_a is the thermal activation energy, and k_B is the Boltzmann constant. In Figure 7 the dependence of $\ln(I)$ as a function of the inverse of the temperature (T) is plotted for PbS thin films. The Arrhenius plot yields a straight line, with the slope corresponding to the value of activation energy. The activation energies for the interval between 330 and 360 K are 0.14, 0.33, and 0.35 eV for deposition times of 2, 3, and 4 min, respectively. It is worth noticing that in polycrystalline materials the activation energy provides a measure of the Fermi energy (E_F), the maximum of the energy for the valence band (E_V), and the energy of the potential barrier of the grain boundaries (E_B), through the relationship $E_a = E_F - E_V + E_B$ [33].

4. Conclusions

The thin films of PbS were grown by the microwave-assisted chemical bath deposition (MA-CBD) technique in a commercial automated system. We were able to reduce the deposition times to less than 5 minutes and obtain films with good adhesion and homogeneousness throughout the surface of the substrate with thickness from 100 to 150 nm. The XRD analysis confirmed the polycrystalline cubic rock salt (NaCl) type structure with crystallite size between 18 and 20 nm as the deposition time was varied from 2 to 4 min. The EDX analysis indicates that the thin films were stoichiometric. All

TABLE 3: Electrical parameters of PbS thin films.

Sample	σ ($10^2 \Omega^{-1} \text{ m}^{-1}$)		S ($\mu\text{V K}^{-1}$)	P (10^{23} m^{-3})	μ_p ($10^{-2} \text{ m}^2 \text{ V}^{-1} \text{ s}^{-1}$)
	Dark	Illumination			
2 min	1.13	1.30	15	8.5	0.13
3 min	0.18	0.23	18	8.1	0.03
4 min	0.13	0.14	19	8.0	0.02

FIGURE 7: Plots of $\ln(I)$ vs $(1/T)$ of PbS thin film as a function of deposition time.

the PbS films exhibit a direct band gap which varies from 1.0 to 1.35 eV. The films are of p-type conductivity with electrical conductivity in the range from 13 to $113 \Omega^{-1} \text{ m}^{-1}$. Besides, hole mobility decreases from 0.13×10^{-2} to $0.02 \times 10^{-2} \text{ m}^2 \text{ V}^{-1} \text{ s}^{-1}$ with increasing deposition time. On the basis of the results, these thin films may be considered as potential candidates for optoelectronic applications.

Data Availability

The data used to support the findings of this study are available from the corresponding author upon request.

Conflicts of Interest

The authors declare that there are no conflicts of interest regarding the publication of this article.

Acknowledgments

We appreciate Yareli Colin Garcia's assistance in the optical measurements. We thank IER-UNAM through CONACYT-LIFYCS 123122 for infrastructure support. This work was supported by PRODEP (UAN-PTC-065 and UAN-PTC-062), CeMIE-Sol project 35, and Patronato UAN through the projects "Impulso a la Investigación."

References

- [1] X. Liu and M. Zhang, "Studies on PbS and PbSe detectors for IR system," *Journal of Infrared, Millimeter, and Terahertz Waves*, vol. 21, p. 1697, 2000.
- [2] S. Gunes, K. P. Fritz, H. Neugebauer, N. S. Sariciftci, S. Kumar, and G. D. Scholes, "Hybrid solar cells using PbS nanoparticles," *Solar Energy Materials and Solar Cells*, vol. 91, p. 420, 2007.
- [3] J. Hernández-Borja, Y. V. Vorobiev, and R. Ramírez-Bon, "Thin film solar cells of CdS/PbS chemically deposited by an ammonia-free process," *Solar Energy Materials and Solar Cells*, vol. 9, p. 1882, 2011.
- [4] S. M. Pawar, B. S. Pawar, J. H. Kim, O.-S. Joo, and C. D. Lokhande, "Recent status of chemical bath deposited metal chalcogenide and metal oxide thin films," *Current Applied Physics*, vol. 11, p. 117, 2011.
- [5] T. Tohidi, K. Jamshidi-Ghaleh, A. Namdar, and R. Abdi-Ghaleh, "Comparative studies on the structural, morphological, optical, and electrical properties of nanocrystalline PbS thin films grown by chemical bath deposition using two different bath compositions," *Materials Science in Semiconductor Processing*, vol. 25, p. 197, 2014.
- [6] B. Thangaraju and P. Kaliannan, "Spray pyrolytically deposited PbS thin films," *Semiconductor Science and Technology*, vol. 15, p. 849, 2000.
- [7] A. Bednarkiewicz, D. Wawrzynczyk, M. Nyk, and W. Strek, "Optical, structural and optoelectronic properties of pulsed laser deposition PbS thin film," *Applied Physics B*, vol. 103, p. 161, 2011.
- [8] S. Kumar, T. P. Sharma, M. Zulfeqar, and M. Husain, "Characterization of vacuum evaporated PbS thin films," *Physica B: Condensed Matter*, vol. 325, pp. 8–16, 2003.
- [9] J. P. Ge, J. Wang, H. X. Zhang, X. Wang, Q. Peng, and Y. D. Li, "Orthogonal PbS nanowire arrays and networks and their raman scattering behavior," *Chrmistry A European Journal*, vol. 11, p. 1889, 2005.
- [10] P. T. Zhao, G. Chen, Y. Hu et al., "Preparation of dendritic PbS nanostructures by ultrasonic method," *Journal of Crystal Growth*, vol. 303, p. 632, 2007.
- [11] K. K. Nanda and S. N. Sahu, "One-dimensional quantum confinement in electrodeposited PbS nanocrystalline semiconductors," *Advanced Materials*, vol. 13, p. 280, 2001.
- [12] M. A. Barote, A. A. Yadav, T. V. Chavan, and E. U. Masumdar, "Characterization and photoelectrochemical properties of chemical bath deposited n-PbS thin films," *Digest Journal of Nanomaterial Biostructures*, vol. 6, p. 979, 2011.
- [13] H. A. Pineda-Leon, G. Gutierrez-Heredia, A. De Leon et al., "Comparative study of PbS thin films growth by two different formulations using chemical bath deposition," *Chalcogenide Letters*, vol. 13, no. 4, pp. 161–168, 2016.
- [14] C. E. Pérez-García, R. Ramírez-Bon, and Y. V. Vorobiev, "PbS thin films growth with CBD and PCBD techniques: a comparative study," *Chalcogenide Letters*, vol. 12, p. 579, 2015.
- [15] A. S. Obaid, Z. Hassan, M. A. Mahdi, and M. Bououdina, "Characterization of nanocrystalline PbS thin films prepared using microwave-assisted chemical bath deposition," *Materials Science in Semiconductor Processing*, vol. 15, p. 564, 2012.
- [16] T. Ding and J. Zhu, "Microwave heating synthesis of HgS and PbS nanocrystals in ethanol solvent," *Materials Science and Engineering: B Advanced Functional Solid-State Materials*, vol. 100, no. 3, pp. 307–313, 2003.
- [17] Y. Zhao, X. H. Liao, J. M. Hong, and J. J. Zhu, "Synthesis of lead sulfide nanocrystals via microwave and sonochemical methods," *Materials Chemistry and Physics*, vol. 87, p. 149, 2004.
- [18] M. Yousefi, M. Sabet, M. Salavati-Niasari, and H. Emadi, "Synthesis and characterization PbS and Bi₂S₃ nanostructures via microwave approach and investigation of their behaviors in solar cell," *Journal of Cluster Science*, vol. 23, p. 511, 2012.
- [19] A. S. Obaid, Z. Hassan, M. A. Mahdi, and M. Bououdina, "Fabrication and characterisations of n-CdS/p-PbS heterojunction solar cells using microwave-assisted chemical bath deposition," *Solar Energy*, vol. 89, p. 143, 2013.
- [20] H. Wang, J.-R. Zhang, and J.-J. Zhu, "A microwave assisted heating method for the rapid synthesis of sphalerite-type mercury sulfide nanocrystals with different sizes," *Journal of Crystal Growth*, vol. 233, p. 829, 2001.
- [21] M. Xin, K. Li, and H. Wang, "Synthesis of CuS thin films by microwave assisted chemical bath deposition," *Applied Surface Science*, vol. 256, p. 1436, 2009.
- [22] W. Tu and H. Liu, "Rapid synthesis of nanoscale colloidal metal clusters by microwave irradiation," *Journal of Materials Chemistry*, vol. 10, no. 9, pp. 2207–2211, 2000.
- [23] S. Messina, M. T. S. Nair, and P. K. Nair, "Solar cells with Sb₂S₃ absorber films," *Thin Solid Films*, vol. 517, no. 7, pp. 2503–2507, 2009.
- [24] B. Altiokka, M. C. Baykul, and M. R. Altiokka, "Some physical effects of reaction rate on PbS thin films obtained by chemical bath deposition," *Journal of Crystal Growth*, vol. 384, p. 50, 2013.
- [25] E. Pentia, L. Pintilie, T. Botila, I. Pintilie, A. Chaparro, and C. Maffiotte, "Bi influence on growth and physical properties of chemical deposited PbS films," *Thin Solid Films*, vol. 434, no. 1-2, pp. 162–170, 2003.
- [26] M. A. Mahdi, Z. Hassan, S. S. Ng, J. J. Hassan, and S. K. M. Bakhori, "Structural and optical properties of nanocrystalline CdS thin films prepared using microwave-assisted chemical bath deposition," *Thin Solid Films*, vol. 520, no. 9, pp. 3477–3484, 2012.
- [27] R. M. Palou, "Microwave-assisted synthesis using ionic liquids," *Molecular Diversity*, vol. 14, no. 1, pp. 3–25, 2010.
- [28] E. Yücel, N. Güler, and Y. Yücel, "Optimization of deposition conditions of CdS thin films using response surface methodology," *Journal of Alloys and Compounds*, vol. 589, p. 207, 2014.
- [29] M. M. Abbas, A. A.-M. Shehabb, N.-A. Hassanb, and A.-K. Al-Samuraee, "Effect of temperature and deposition time on the optical properties of chemically deposited nanostructure PbS thin films," *Thin Solid Films*, vol. 519, p. 4917, 2011.
- [30] D. K. Schroder, *Semiconductor Materials and Device Characterization*, Wiley, New York, NY, USA, 2nd edition, 1990.
- [31] H. Moreno-García, M. T. S. Nair, and P. K. Nair, "Chemically deposited lead sulfide and bismuth sulfide thin films and Bi₂S₃/PbS solar cells," *Thin Solid Films*, vol. 519, no. 7, pp. 2287–2295, 2011.
- [32] J. I. Pankove, *Optical Processes in Semiconductors*, Dover, New York, NY, USA, 2nd edition, 1975.
- [33] J. W. Orton, B. J. Goldsmith, J. A. Chapman, and M. J. Powell, "The mechanism of photoconductivity in polycrystalline cadmium sulphide layers," *Journal of Applied Physics*, vol. 53, no. 3, pp. 1602–1614, 1982.
- [34] J. Y. W. Seto, "The electrical properties of polycrystalline silicon films," *Journal of Applied Physics*, vol. 46, no. 12, pp. 5247–5254, 1975.

- [35] E. Canessa and V. L. Nguyen, "Non-linear I–V characteristics of double Schottky barriers and polycrystalline semiconductors," *Physica B: Condensed Matter*, vol. 179, no. 4, pp. 335–341, 1992.
- [36] R. Matsubara, N. Ohashi, M. Sakai, K. Kudo, and M. Nakamura, "Analysis of barrier height at crystalline domain boundary and in-domain mobility in pentacene polycrystalline films on SiO₂," *Applied Physics Letters*, vol. 92, no. 24, p. 242108, 2008.
- [37] R. Baier, C. Leendertz, D. Abou-Ras, M. C. Lux-Steiner, and S. Sadewasser, "Properties of electronic potential barriers at grain boundaries in Cu(In,Ga)Se₂ thin films," *Solar Energy Materials and Solar Cells*, vol. 130, pp. 124–131, 2014.
- [38] T. Kamiya, Z. A. K. Durrani, and H. Ahmed, "Reduction of grain-boundary potential barrier height in polycrystalline silicon with hot H₂O-vapor annealing probed using point-contact devices," *Journal of Vacuum Science & Technology B*, vol. 21, p. 1000, 2003.
- [39] S. M. Sze, *Physics of Semiconductors Devices*, Wiley, New York, NY, USA, 2nd edition, 1981.
- [40] R. A. Smith, *Semiconductors*, Cambridge University Press, Cambridge, UK, 2nd edition, 1978.
- [41] K. Bindu, J. Campos, M. T. S. Nair, A. Sanchez, and P. K. Nair, "Semiconducting AgSbSe₂ thin film and its application in a photovoltaic structure," *Semiconductor Science and Technology*, vol. 20, p. 496, 2005.

Research Article

Effect of Adding Co on Crystallization Behavior and Magnetoimpedance Effect of Amorphous/Nanocrystalline FeCuNbSiB Alloy Strips

Da-guo Jiang,¹ Yuan-xiu Ye,¹ and Bin Guo ²

¹College of Mathematics and Physics, Jingtangshan University, Jinan 343009, China

²Network Information Center, Jingtangshan University, Jilan 343009, China

Correspondence should be addressed to Bin Guo; 105120398@qq.com

Received 19 November 2018; Accepted 6 January 2019; Published 3 February 2019

Guest Editor: Jun-Cheng Zhang

Copyright © 2019 Da-guo Jiang et al. This is an open access article distributed under the Creative Commons Attribution License, which permits unrestricted use, distribution, and reproduction in any medium, provided the original work is properly cited.

After one of the B atoms in $\text{Fe}_{73.5}\text{Cu}_1\text{Nb}_3\text{Si}_{13.5}\text{B}_9$ alloy was replaced by both 0.7 Si and 0.3 Co, $\text{Fe}_{73.5}\text{Co}_{0.3}\text{Cu}_1\text{Nb}_3\text{Si}_{14.2}\text{B}_8$ alloy ribbons were prepared by single roll fast quenching method. The obtained alloy ribbons were subsequently wound into ring magnetic cores, and then these magnetic cores were annealed at different temperatures in air. The effects of adding Co on the crystallization behavior and soft magnetic properties of the as-quenched alloy ribbons with and without heat treatment were studied. The results show that the amorphous structure of the prepared $\text{Fe}_{73.5}\text{Co}_{0.3}\text{Cu}_1\text{Nb}_3\text{Si}_{14.2}\text{B}_8$ alloy ribbons is transformed into the coexistence of amorphous and nanocrystalline structures after heat treatment at 550°C. Comparing with $\text{Fe}_{73.5}\text{Cu}_1\text{Nb}_3\text{Si}_{13.5}\text{B}_9$ alloy ribbons, the first initial crystallization temperature (T_{x1}) and crystallization peak temperature (T_{p1}) of $\text{Fe}_{73.5}\text{Co}_{0.3}\text{Cu}_1\text{Nb}_3\text{Si}_{14.2}\text{B}_8$ alloy ribbons were reduced by 1.6 and 1.7°C, respectively, while the second initial crystallization temperature (T_{x2}) and crystallization peak temperature (T_{p2}) were increased by 6.5 and 5.7°C, respectively, resulting in that the difference between the first and the second initial crystallization temperatures (ΔT_x) are increased by 8.1°C; the initial permeability (μ_i) and saturation induction density (B_s) of the amorphous/nanocrystalline $\text{Fe}_{73.5}\text{Co}_{0.3}\text{Cu}_1\text{Nb}_3\text{Si}_{14.2}\text{B}_8$ magnetic cores were reduced by 0.15 H/m and 0.39 T, respectively, while the coercivity (H_c) is increased by 0.34 A/m.

1. Introduction

Since a fast quenching process was employed to prepare the amorphous alloys by Klement et al. in 1960 [1], it has been attracting more and more attention of researchers because of its unique structure, efficient preparation process, excellent material properties, and wide application prospects [2]. The amorphous soft magnetic alloy is mainly composed of Fe, Co, and Ni belonging to ferromagnetic metal elements, as well as Si, B, P, and C belonging to amorphous metal elements. Generally, a small amount of transitional elements or rare-earth elements is usually added into the amorphous soft magnetic alloy [3, 4], to improve the ability and thermal stability of the amorphous alloy. Yashizawa et al. found that the iron-based alloy with an amorphous and nanocrystalline dual-phase structure can be conveniently obtained by adding a small amount of Cu and M (M=Nb, Ta, Mo and W, etc.) into

the amorphous Fe-Si-B alloy family and annealing them at an appropriate temperature [5].

Panina and Mohrifirstly noticed the giant magnetoimpedance (GMI) effect in the amorphous CoFeSiB soft magnetic alloy wire in 1994, where the impedance value changes with the applied magnetic field along the axis of the wire when the amorphous wire is excited by alternating current [6]. Afterwards, the GMI were also observed in Fe-based nanocrystalline ribbons, films, and wires with high permeability [7, 8]. The various miniature sensors based on GMI have been applied in measurement of weak magnetic fields, detection of azimuth, and magnetic recording technology due to the advantages of this effect such as high sensitivity, small size, and fast response [9].

Both the high temperature properties and high frequency performance of the alloys can be improved by replacing Fe in finemet soft magnetic alloy with Co [10–12]. In this work,

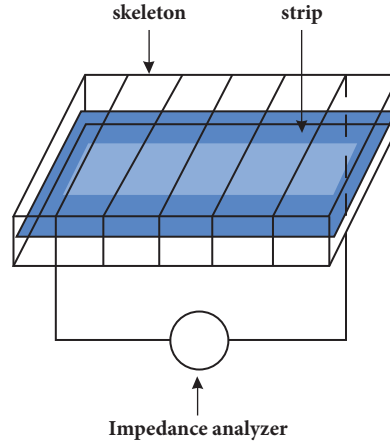


FIGURE 1: Scheme of testing principle of magnetoimpedance effect.

the $\text{Fe}_{73.5}\text{Co}_{0.3}\text{Cu}_1\text{Nb}_3\text{Si}_{14.2}\text{B}_8$ (Alloy-II (Co)) alloy strip is successfully prepared by signal roll quenching method by adjusting the composition of $\text{Fe}_{73.5}\text{Cu}_1\text{Nb}_3\text{Si}_{13.5}\text{B}_9$ (Alloy-I). The annealing of the alloy strip at different temperatures is conducted to study the effect of adding Co on the crystallization behavior of the alloy strip. The direct-current (DC) soft magnetic properties of the amorphous/nanocrystalline cores, as well as the magnetic impedance effect of the amorphous/nanocrystalline strips, are also investigated.

2. Sample Preparation and Test Method

The signal roll quenching is employed to prepare the alloy strip of Alloy-I and Alloy-II (Co) with the width 20 mm and thickness 25 μm , respectively. Firstly, the alloy strip is wound into a ring core with an outer diameter of 40 mm and inner diameter of 25 mm by a tape winding machine. Then the end of the strip is welded with amorphous spot welder. Afterwards, the ring core is annealed in a nonmagnetic stainless steel tubular atmosphere resistance furnace in nitrogen atmosphere at the temperature of 350, 400, 450, 500, and 550°C, respectively, and, at each temperature, the duration is 100 min. Finally, the annealed strip is air cooled.

The X-ray diffractometer (XRD) Bruker D-9 is employed to conduct phase analysis. In detail, the copper target K_α rays with wavelength of 0.154 nm, diffraction angle 2θ range of 20~90°, and step size of 0.02° is utilized. The working current and voltage are 40 kV and 40 mA, respectively. The differential thermal analysis is carried on with synchronous thermal analyzer SDT Q600 instrument (TA, America), and the heating rate is 10°C·min⁻¹. The Argon atmosphere with purity of 99.99% is put to use for protection. Besides, the soft magnetic DC tester MATS-2010SD is employed to test the DC soft magnetic performance. During the process, the amorphous/nanocrystalline cores annealed at 550°C are loaded into the tray in the first place, and then 10 turns of primary coil and 3-turn secondary coil are wound on the guard plate with enameled wires. The effective magnetic path length of amorphous/nanocrystalline cores is 98.44 mm and the effective cross-sectional area is 127.3 mm². In addition, the

impedance meter 4284A is employed to test the impedance of amorphous/nanocrystalline, and the current amplitude and alternating current frequency are set as 10 mA and 0.1~1 MHz, respectively. The magnetic field drawing instrument is employed to generate magnetic field and the intensity is 0~2800 A/m. Both the DC magnetic field and the current direction are along the length direction of the strip and perpendicular to the geomagnetic field.

As shown in Figure 1, it is the scheme of testing principle of magnetoimpedance effect. The 200-turn copper enameled wire ($\Phi = 0.21$ mm) is layered and evenly wound around the induction coil skeleton (plastic rectangular hollow tube with a section of 7.76 mm in length and 2.15 mm in width and 8.23 mm in length and 3.05 mm in width, respectively). Afterwards, a 2 cm long amorphous/nanocrystalline strip annealed at 550°C is placed in the middle of the inductor skeleton. Finally, the inductor is placed in the center of the magnetic field, and the axial direction of the inductance coil is set to be parallel to the magnetic field.

The effect of impedance is defined as amplitude of impedance variation like

$$\Delta Z = |Z_H - Z_0|, \quad (1)$$

where Z_0 is impedance of inductance coil without magnetic field and Z_H is impedance of inductance coil after axial magnetic field applied.

In Figure 2, the equivalent circuit model is displayed to reveal the magnetoimpedance effect. The impedance of alloy strip can be equivalent to the series circuit model of resistance R and inductance L , and the impedance is

$$Z = \sqrt{R^2 + (2\pi fL)^2}, \quad (2)$$

$$L = \frac{\mu N^2 S}{l}, \quad (3)$$

where, in (2), f is the frequency for testing and R and L are the resistance and inductance of the coil, respectively. In (3), N and l stand for the round and length (which is equal to the length of amorphous/nanocrystalline strip) of the coil,

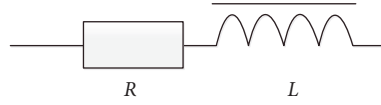


FIGURE 2: The equivalent circuit model of magnetoimpedance effect.

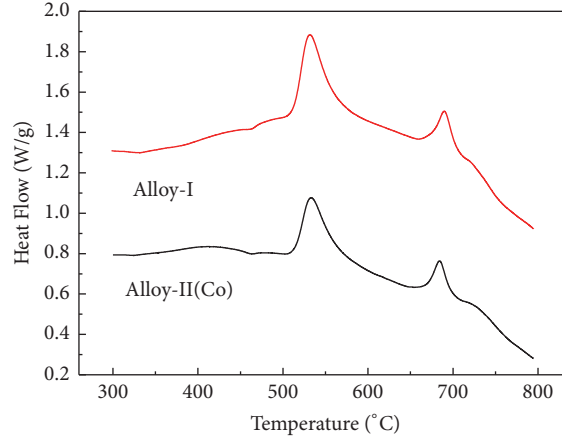


FIGURE 3: DSC curves of as-quenched alloy strips.

respectively. μ and S represent the magnetic permeability of the amorphous/nanocrystalline strip and cross section area of coil, respectively.

From (1), (2), and (3), the impedance of amorphous/nanocrystalline strip can be calculated by

$$\Delta Z = |Z_H - Z_0| = \left| \sqrt{R^2 + \left(\frac{2\pi f \mu_h N^2 S}{l} \right)^2} - \sqrt{R^2 + \left(\frac{2\pi f \mu_0 N^2 S}{l} \right)^2} \right|, \quad (4)$$

where μ_0 is the permeability of amorphous/nanocrystalline strip without magnetic field, while μ_h denotes the permeability of amorphous/nanocrystalline strip after axial magnetic field is applied.

3. Result and Analysis

3.1. Effect of Adding Co on Amorphous and Crystallization Behavior of Alloy Strip. As can be seen from Figure 3, both quenched alloy strips have a two-stage crystallization process. In the first stage, the starting crystallization temperatures are 514.4 and 512.8°C, respectively, while the crystallization peak temperatures are 533.4 and 531.7°C, respectively. Regarding the second stage, the starting crystallization temperatures are 665.4 and 671.9°C, respectively, and the crystallization peak temperatures are 684.1 and 689.8°C, respectively. The differences of the starting crystallization temperature of the two stages are 151 and 159.1°C, respectively.

As shown in Figure 4, the diffraction spectra of two kinds of alloy strip with different quenched states perform typical diffuse peak characteristics of amorphous structure, and there are no sharp diffraction peaks in the crystalline phase. It

indicates that both of the alloy strips with different quenched states possess noncrystalline structure. The strength of the diffuse peaks of the two alloy strips increases but the diffuse peak width is gradually narrowed at 2θ of $\approx 45^\circ$ along with the increasing of annealing temperature. When the annealing temperature reaches 500°C, the sharp diffraction peaks appear at 2θ with $\approx 44.7^\circ$, 65° , and 82° for the both alloy strips. With comparison to the PDF card (35-0519), the crystal surfaces including (110), (200), and (211) belonging to the Fe_3Si phase with body centered cubic (BCC) structure can be clearly identified. On the other hand, when the annealing temperature comes to 550°C, the diffraction peak intensity of Alloy-II (Co) alloy strip gets stronger, and the width of the peak is narrower compared to Alloy-I alloy strip. Judged from Scherrer equation, the grain sizes of Alloy-I and Alloy-II (Co) alloy strips can be calculated to be about 11.044 and 12.734 nm at 2θ of $\approx 44.7^\circ$, respectively. It reveals that both alloy strips can form a composite structure with the coexistence of the amorphous and nanocrystalline phases superior to heat treatment at 550°C.

From the results in Figures 3 and 4, we find that the first crystallization peak corresponds to the precipitation of soft magnetic solid solution (precipitation of α -Fe phase). And the second crystallization peak is the crystallization of the remaining amorphous phase, which is mainly related to the precipitation of Co-B, Fe-B, and Nb-Co compounds [13–15]. Compared to the Alloy-I alloy strip, the Alloy-II (Co) one possesses lower starting crystallization temperature and crystallization peak temperature, which indicates that the Co addition will lead to worse thermal stability of amorphous alloy [16, 17]. However, the addition of Co increases the difference between the one- and two-stage crystallization temperature of the alloy strip, which is conducive to the precipitation of a single Fe-Si phase and the precipitation of

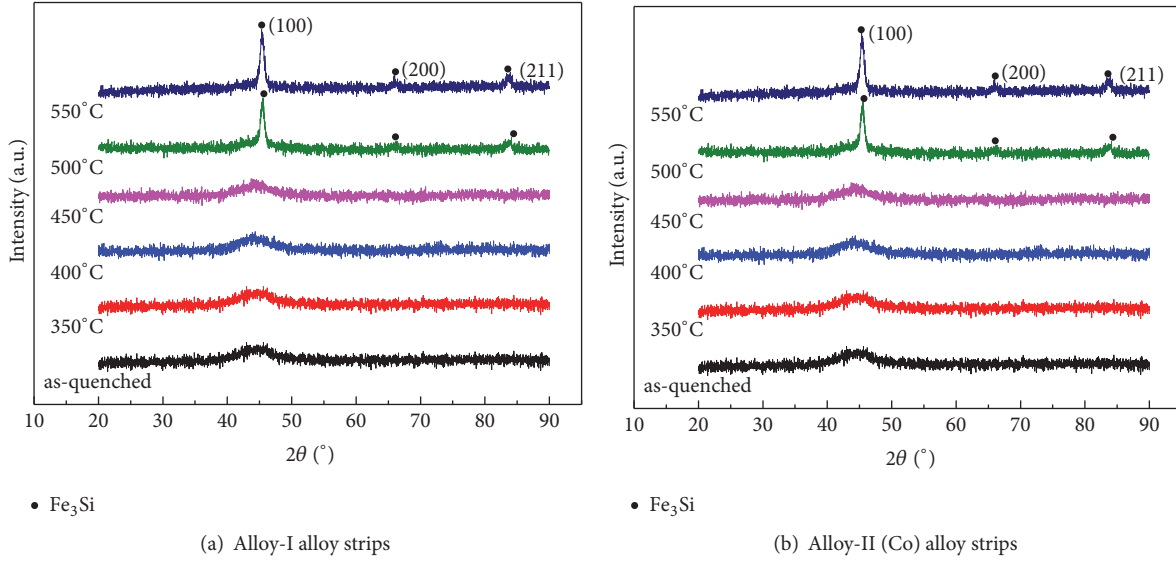


FIGURE 4: XRD patterns of as-quenched and annealing alloy strips.

Fe-B phase which affects the magnetic properties of the alloy. Actually, Co element possesses similar chemical property to Fe, and if Co element is added to the amorphous alloy system, solid solution will be formed. In this process, Co atoms increase the chaos of the alloy melt by occupying the spatial lattice position of the Fe atoms, resulting in formation of amorphous phase. Besides, the addition of Co element can delay the occurrence of crystallization reaction and restrict the precipitation of amorphous phase, which also promotes the formation of amorphous phase.

3.2. Effect of Adding Co on DC Soft Magnetic Properties of Amorphous/Nanocrystalline Crystalline Cores. The effect of adding Co on DC soft magnetic properties of amorphous/nanocrystalline cores is displayed in Table 1, where μ_i and μ_m mark the initial and maximum permeability, respectively; B_s and B_r represent the saturation magnetic induction intensity and residual magnetism, respectively. The hysteresis loss and coercive force are denoted by P_u and H_c , respectively. Compared with the amorphous/nanocrystalline Alloy-I core, the amorphous/nanocrystalline Alloy-II (Co) magnetic cores possesses lower initial permeability, maximum magnetic permeability, hysteresis loss, saturation magnetic induction, and residual magnetism, but it yields to coercive force. This trend shows that adding Co element reduces the DC soft magnetic properties of amorphous/nanocrystalline cores. The decrease of initial permeability can improve the antisaturation ability and antibiasing ability of amorphous/nanocrystalline magnetic core under DC bias, to some extent. In particular, the stability of the amorphous/nanocrystalline core can be greatly improved in the electromagnetic application environment with DC component.

3.3. Effect of Adding Co on Magnetic Impedance of FeCuNbSiB Amorphous/Nanocrystalline Strip. The magnetoimpedance effect of the amorphous/nanocrystalline Alloy-I strip annealed at 550°C is shown in Figure 5. The results indicate

that the impedance Z and amplitude of the impedance ΔZ increase as the test frequency f increases when the magnetic field strength H is fixed at constant. On the other side, when the test frequency f remains unchanged, the impedance Z will decrease but the amplitude of the impedance ΔZ is just the opposite along with the increase of H which is the magnetic field strength. In fact, given a coil with resistance R , number of turns N , cross section area S , and length l , the permeability μ of amorphous/nanocrystalline strip is constant if the magnetic field intensity H remains unchanged, leading to increase of impedance Z as the increase of test frequency f from (2) and (3). However, the permeability μ of the amorphous/nanocrystalline strip decreases with the increase of magnetic field intensity H when the test frequency f is constant [8], following decrease of the impedance Z as the increase of magnetic field strength H according to (2) and (3).

In addition to the above discussion, Z_H will decrease along with the increase of magnetic strength H since Z_0 is a constant if the test frequency f remains to be unchanged, resulting in the increase of ΔZ as the increase of H according to (4), while μ_H is constant if the magnetic strength H stays in the same condition, with the increase of ΔZ as increase of f from (4).

In Figure 6, the magnetoimpedance effect of the amorphous/nanocrystalline Alloy-I and Alloy-II (Co) strips annealed at 550°C is tested and shown, where the test frequency is 1.0MHz. The results show that the impedance variation amplitude ΔZ of the amorphous/nanocrystalline Alloy-II (Co) strip increases compared to the Alloy-I one.

4. Conclusion

In conclusion, the following two aspects can be attributed in this work:

(1). The amorphous $\text{Fe}_{73.5}\text{Co}_{0.3}\text{Cu}_1\text{Nb}_3\text{Si}_{14.2}\text{B}_8$ strip is successfully prepared by single roll quenching method by

TABLE 1: DC soft magnetic properties of the amorphous/nanocrystalline cores heat treatment at 550°C.

Magnetic core	$\mu_i/(\text{H}\cdot\text{m}^{-1})$	$\mu_m/(\text{H}\cdot\text{m}^{-1})$	$P_u/(\text{T}\cdot\text{A}\cdot\text{m}^{-1})$	B_s/T	B_r/T	$H_c/(\text{A}\cdot\text{m}^{-1})$
Alloy-I	0.39	0.99	2.77	1.52	0.76	0.40
Alloy-II (Co)	0.24	0.61	1.9	1.13	0.64	0.74

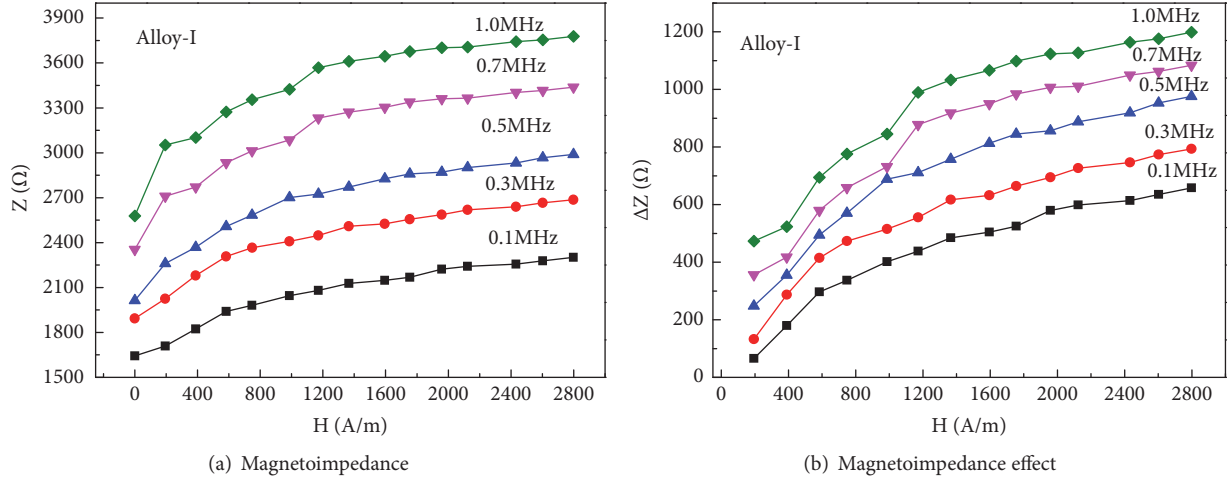


FIGURE 5: The magneto impedance effect of the Alloy-I amorphous/nanocrystalline strips after heat treatment at 550°C.

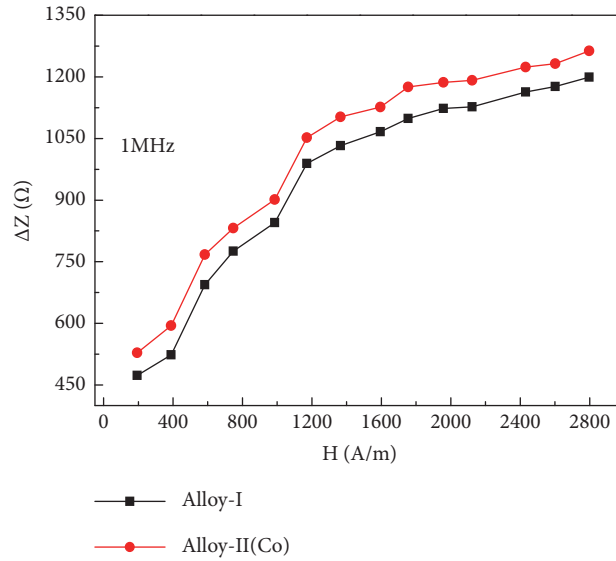


FIGURE 6: The magnetoimpedance effect of Alloy-I and Alloy-II(Co) amorphous/nanocrystalline strips after heat treatment at 550°C.

replacing one B atom with 0.7 Si and 0.3 Co based on the $\text{Fe}_{73.5}\text{Cu}_1\text{Nb}_3\text{Si}_{13.5}\text{B}_9$ alloy. Both amorphous strips can be formed, the amorphous/nanocrystals dual-phase structure after heat treatment at 550°C. Compared to the amorphous $\text{Fe}_{73.5}\text{Cu}_1\text{Nb}_3\text{Si}_{13.5}\text{B}_9$ strip, both the first-stage initial crystallization temperature and crystallization peak temperature of the amorphous $\text{Fe}_{73.5}\text{Co}_{0.3}\text{Cu}_1\text{Nb}_3\text{Si}_{14.2}\text{B}_8$ ribbon get lower, but both the initial crystallization temperature and the crystallization peak temperature are higher in the second

stage, and the difference of initial crystallization temperatures increases between the two stages.

(2). The initial magnetic permeability, saturation magnetic induction, and the DC soft magnetic properties of the amorphous/nanocrystalline $\text{Fe}_{73.5}\text{Co}_{0.3}\text{Cu}_1\text{Nb}_3\text{Si}_{14.2}\text{B}_8$ magnetic core are all reduced, but it yields to the coercive force compared with the amorphous/nanocrystalline $\text{Fe}_{73.5}\text{Cu}_1\text{Nb}_3\text{Si}_{13.5}\text{B}_9$ magnetic core. In addition, the impedance amplitude of the amorphous/nanocrystalline

$\text{Fe}_{73.5}\text{Co}_{0.3}\text{Cu}_1\text{Nb}_3\text{Si}_{14.2}\text{B}_8$ strip increases compared to the amorphous/nanocrystalline $\text{Fe}_{73.5}\text{Cu}_1\text{Nb}_3\text{Si}_{13.5}\text{B}_9$ strip.

Data Availability

The data used to support the findings of this study are included within the article. And the shared data allows both the Hindawi publisher and other researchers to verify the results of an article, replicate the analysis, and conduct secondary analyses.

Conflicts of Interest

The authors declare that they have no conflicts of interest.

References

- [1] W. Klement, R. H. Willens, and P. Duwez, "Non-crystalline structure in solidified Gold-Silicon alloys," *Nature*, vol. 187, no. 31, pp. 869-870, 1960.
- [2] R. Hasegawa, "Applications of amorphous magnetic alloys in electronic devices," *Journal of Non-Crystalline Solids*, vol. 287, no. 1/2/3, pp. 405-412, 2001.
- [3] J. Daguo, Y. Yuanxiu, and Y. Caobing, "Magnetic induction effect of rare-earth La modified $\text{Fe}_{78}\text{Si}_9\text{B}_{13}$ amorphous ribbons," *Material for Mechanical Engineering*, vol. 38, no. 3, pp. 66-69, 2014.
- [4] G. Bin, Y. Yuanxiu, J. Daguo, A. Hui, and W. Zhihui, "Glass forming ability and magneto impedance effect of FeCuNbSiB-La alloy strips," *Ordinance Material Science and Engineering*, vol. 38, no. 4, pp. 22-25, 2015.
- [5] Y. Yoshizawa, S. Oguma, and K. Yamauchi, "New Fe-based soft magnetic alloys composed of ultrafine grain structure," *Journal of Applied Physics*, vol. 64, no. 10, pp. 6044-6046, 1988.
- [6] K. Mohri, T. Kohzawa, k. Kawashima et al., "Magnetor induced effect in amorphous wires," *IEEE Trans Magn*, vol. 28, no. 2, pp. 3150-3152, 1992.
- [7] H. Qin, J. Hu, B. Li, and R. Zhang, "Giant magnetoimpedance effect in Fe-Cu-Nb-Si-B as-cast ribbons," *Rare Metal Materials and Engineering*, vol. 35, no. 2, pp. 270-272, 2006.
- [8] J. Daguo, F. Yuan, Z. Zhenghou, S. Hui et al., "Magneto impedance effect of FeSiB amorphous alloy ribbons," *Hot Working Technology*, vol. 39, no. 10, pp. 37-39, 2010.
- [9] J. Daguo, Z. Zhenghou, S. Hui et al., "Influence factors of Magnet-inductive effect of $\text{Fe}_{73.5}\text{Cu}_1\text{Nb}_3\text{Si}_{13.5}\text{B}_9$ amorphous alloy ribbons," *Materials for Mechanical Engineering*, vol. 33, no. 4, pp. 29-34, 2009.
- [10] B. K. Aleksandra, K. Roman, K. Tadeusz et al., "Magnetic properties of Co doped finemet at elevated temperature," *Reviews on Advanced Materials Science*, vol. 18, no. 6, pp. 545-548, 2008.
- [11] M. Danning, Y. Changlin, and W. Xiaowei, "Research development of FeCoalloy soft magnetic materials," *Rare Metal Materials and Engineering*, vol. 42, no. 6, pp. 1316-1319, 2013.
- [12] L. Liya, Y. Jianghong, G. Yicheng et al., "Nanocrystallization and microstructure of $(\text{FeCo})_{73.5}\text{Cu}_1\text{Nb}_3\text{Si}_{13.5}\text{B}_9$," *Journal of Central South University (Science and Technology)*, vol. 39, no. 3, pp. 522-526, 2008.
- [13] D. Yanhong, *Investigation on Magnetic Properties of Nanocrystalline Fe-Co-Cu-Nb-Si-B Soft Magnetic Alloys [M. S. thesis]*, Tianjin University of Technology (Tian Jin), 2004.
- [14] M. Xiaohua, W. Zhi, and W. Guangjian, "Microstructures and high-frequency magnetic properties of nanocrystalline $(\text{Fe}_{1-x}\text{Co}_x)_{78.4}\text{Nb}_{2.6}\text{Si}_9\text{B}_9\text{Cu}_1$ soft magnetic alloys," *Acta Metallurgica Sinica*, vol. 43, no. 3, pp. 281-285, 2007.
- [15] D. Yanhong, L. Mingji, Y. Baohe et al., "AC magnetic properties of $\text{Fe}_{15.38}\text{Co}_{61.52}\text{Cu}_{0.6}\text{Nb}_{2.5}\text{Si}_{11}\text{B}_9$ nanocrystalline soft magnetic alloy," *Acta Physica Sinica*, vol. 69, no. 9, pp. 0975021-0975025, 2011.
- [16] Y. Jia, Z.-J. Wei, M.-Z. Ma, S.-Y. Zeng, and W.-K. Wang, "Thermal stability and crystallization process of FeCoNbSiBCu bulk metallic glasses," *Journal of Materials Engineering*, vol. 36, no. 6, pp. 33-35, 2008.
- [17] Y. Wanqiu, L. Dong, S. Yaming et al., "Effect of Co content on thermal stability and microstructure of $\text{Fe}_{80-x}\text{Co}_x\text{Zr}_8\text{Mo}_2\text{B}_9\text{Cu}_1$ alloys," *Transactions of Materials and Heat Treatment*, vol. 35, no. 12, pp. 146-149, 2014.

Research Article

Mechanical Characterization of Reduced Graphene Oxide Using AFM

Alem Teklu , Canyon Barry, Matthew Palumbo, Collin Weiwadel, Narayanan Kuthirummal, and Jason Flagg

Department of Physics and Astronomy, College of Charleston, Charleston, SC, USA

Correspondence should be addressed to Alem Teklu; teklua@cofc.edu

Received 20 August 2018; Revised 21 November 2018; Accepted 6 December 2018; Published 2 January 2019

Guest Editor: Hong Fang

Copyright © 2019 Alem Teklu et al. This is an open access article distributed under the Creative Commons Attribution License, which permits unrestricted use, distribution, and reproduction in any medium, provided the original work is properly cited.

Nanoindentation coupled with Atomic Force Microscopy was used to study stiffness, hardness, and the reduced Young's modulus of reduced graphene oxide. Oxygen reduction on the graphene oxide sample was performed via LightScribe DVD burner reduction, a cost-effective approach with potential for large scale graphene production. The reduction of oxygen in the graphene oxide sample was estimated to about 10 percent using FTIR spectroscopic analysis. Images of the various samples were captured after each reduction cycle using Atomic Force Microscopy. Elastic and spectroscopic analyses were performed on the samples after each oxygen reduction cycle in the LightScribe, thus allowing for a comparison of stiffness, hardness, and the reduced Young's modulus based on the number of reduction cycles. The highest values obtained were after the fifth and final reduction cycle, yielding a stiffness of 22.4 N/m, a hardness of 0.55 GPa, and a reduced Young's modulus of 1.62 GPa as compared to a stiffness of 22.8 N/m, a hardness of 0.58 GPa, and a reduced Young's modulus of 1.84 GPa for a commercially purchased graphene film made by CVD. This data was then compared to the expected values of pristine single layer graphene. Furthermore, two RC circuits were built, one using a parallel plate capacitors made of light scribed graphene on a kapton substrate (LSGC) and a second one using a CVD deposited graphene on aluminum (CVDGC). Their RC time constants and surface charge densities were compared.

1. Introduction

The unique one-atom-thick two-dimensional structure of carbon nanomaterial graphene must continually be examined as it exhibits many desired mechanical, electrical, thermal, and optical properties [1]. These properties influence and affect surface area, conductivity, the quantum hall effect, electron scattering, band structure, and the Klein paradox [2].

Even though graphene is well studied, its large scale commercial production still proves challenging and expensive [3, 4]. Thus, there is a high likelihood that many scientists will attempt to develop new and cost-effective graphene fabricating techniques [5, 6]. As such, this work focuses on the importance of examining the properties of homemade reduced graphene oxide that proves to be significant for interpreting future scientific investigations. We used LightScribe DVD burner, a cost-effective approach with potential for large scale graphene production. Yet, not much work has been done on the elastic or mechanical

properties of such large size two-dimensional homemade films of reduced graphene oxide samples. Therefore, in this work, we used nanoindentation coupled with Atomic Force Microscopy (AFM) in order to obtain better understanding of the structure and the mechanical properties of both homemade reduced graphene oxide and commercially purchased graphene (made by chemical-vapor deposition). The main investigation surrounding homemade reduced graphene oxide revolves around measuring the difference in stiffness, hardness, and the reduced Young's modulus of samples based on the number of trips through a LightScribe DVD burner [7]. Images of each sample were captured after its oxygen reduction cycle in the LightScribe. These results were then compared to the experimentally determined values for the reduced Young's modulus of a commercially purchased sample, as well as the expected theoretical value for pristine graphene. Two properties of graphene that are important for its use in electrical applications (such as supercapacitors) is that it consists of a honeycomb arrangement of carbon atoms

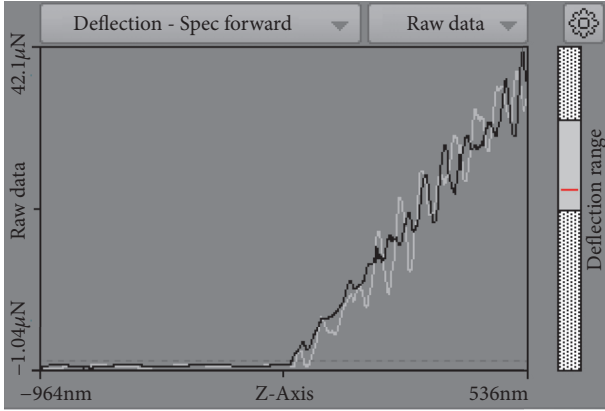


FIGURE 1: Force-distance curve for graphene oxide. The white line depicts the loading stage, while the black line represents the unloading stage.

that is one-atom thick allowing a high specific surface area and that it has a high electron mobility. Thus, two parallel plate capacitors were built using laser-scribed graphene on a kapton substrate as the electrodes for one (LSGC), and chemical-vapor deposited graphene on an aluminum foil substrate as the electrodes for the other (CVDGC).

2. Theory

Nanoindentation serves as one of the most common means of testing mechanical properties of materials. Once calibrated, the Atomic Force Microscope (AFM) measures the intensity of interactions between a probe and the sample during the loading stage (indentation) and the unloading stage (while the probe is retracted). The small area of the probe tip, which comes in various shapes, allows for a high sensitivity to minuscule forces. The probe tips are placed on soft springs (cantilevers), which are often made of silicon, allowing for detection of forces in the range of a few nN [8]. These subtle interactions are recorded on a force-distance curve as shown in Figure 1. From this curve, numerous mechanical properties of thin-films and characteristics can be derived.

2.1. Imaging. The Nanosurf Flex Atomic Force Microscope and AFMs in general are widely used to create both two and three-dimensional surface images [10]. These images are accurate on a nanometer scale and can be taken using both contact and noncontact probes.

Along with high resolution imaging, the Nanosurf can also be used for various spectroscopic investigations, in this instance, nanoindentation. The calibration of the AFM allows the indentation measurements to be taken in nano-Newtons based on the cantilever spring constant instead of voltage based on the scan head calibration. This allows for derivations of stiffness, hardness, and the reduced Young's modulus based on the force-distance curve.

2.2. Force Spectroscopy and Nanoindentation. In force spectroscopy mode the AFM probe is used as an indenter.

Depending on the spring constant and strength of the indenting probe, vertical forces are applied ranging from μN to tens of pN. When indenting a surface on a nanometric scale, many atomic forces interact with the attraction and separation of the probe leading to distinct stages of the cantilever deflection and force-distance curve. As the cantilever approaches the sample with just nanometers of separation, atomic van der Waals forces attract the probe to jump-to-contact resulting in a negative vertical force measurement. After physical contact, continued vertical force is applied to the sample causing elastic and plastic deformation; this is the loading stage. Subsequently, once the max force P_{max} is reached the cantilever is retracted. The release of pressure is measured and visualized in the unloading stage. In the last phase of cantilever retraction, adhesion forces between the probe and sample cause a jump-off-contact point where, again, negative vertical forces are measured. Though these adhesive and attractive forces give insight into the electrostatic properties of the sample, nanomechanical and structural characteristics are extracted from the contour of the unloading stage in the force-distance curve. Figure 2 shows an idea force-distance curve with respective loading and unloading stages. The nanometric contact nature between the AFM probe and sample makes the accurate measurement of necessary parameters, such as the area of probe contact (A_c), challenging. Thus, many methods have been introduced to accurately model the tip-sample interaction while enabling a derivation of relevant structural characteristics. Our analysis used AtomicJ [11] for determining the stiffness and reduced Young's modulus and the widely accepted method proposed by Oliver and Pharr for determining the hardness. This relationship is given in Equation (4).

Using the Oliver and Pharr model, three main characteristics must be measured from the force-distance curve: the maximum applied load, P_{max} (N), the displacement at P_{max} , $h_{max}(m)$, and the contact stiffness, S . Once these quantities are measured, the projected cross sectional area of the indenter, $A(h_c)(m^2)$, is calculated using h_c , the residual contact depth, and a conical approximation of the probes dimensions using the manufacturer's specifications. Figure 3 shows the probe manufacturers tetrahedral tip dimensions used for calculating the conical cross section.

Figure 4 shows an ideal indentation to visualize the contact depth, h_c [see (1)], and subsequent projected cross-sectional area equation [see (2)]. The contact depth is written as

$$h_c = h_{max} - \epsilon \left(\frac{P_{max}}{S} \right) \quad (1)$$

where $\epsilon = 0.75$, constant for conical tip indenter. Similarly, the projected area is given by

$$A(h_c) = (\pi) [\tan(18^\circ)(h_c)]^2 \quad (2)$$

As seen in Figure 2, contact stiffness, S , is calculated to be the slope of the unloading curve. Because the upper portion of the unloading curve corresponds to the linear stage of the probe retraction before tapering off, the most

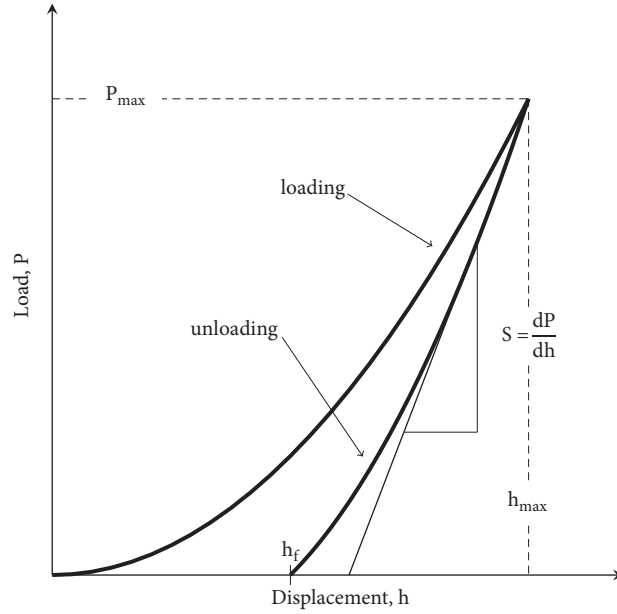


FIGURE 2: Force-distance curve for graphene oxide. The white line depicts the loading stage, while the black line represents the unloading stage.

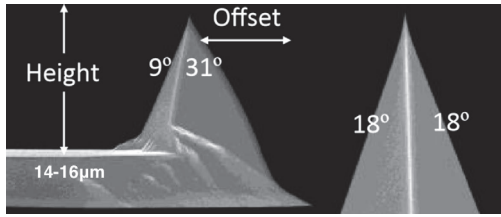


FIGURE 3: This figure, provided by AppNano, shows the dimensions of the tetrahedral tip.

accurate stiffness measurements are calculated from this initial gradient. Mathematically,

$$S = \left(\frac{\partial P}{\partial h} \right). \quad (3)$$

Once contact area is determined, the hardness, H , defined as the mean pressure a substance can support across that area, is calculated using the equation

$$H = \frac{P_{max}}{A(h_c)} \quad (4)$$

where P_{max} is the max load (N) and A is the contact area during indentation (m^2) [12].

Young's modulus is a measure of elasticity or the stress and strain ratio of a substance. Because of elastic nature of the unloading curve, the reduced or effective Young's modulus was calculated [13]. Using the stiffness from Equation (3) and the contact area from Equation (2), the reduced elastic

modulus takes elastic deformations in both the probe and sample into account and is given by

$$E_r = \frac{S\sqrt{\pi}}{2\sqrt{A}(h_c)}, \quad (5)$$

where E_r is the reduced Young's modulus (Pa).

3. Methodology

3.1. Production of Graphene. For large scale top-down synthesis of graphene, it begins with a block of graphite. Because graphite is simply billions of graphene sheets stacked together, the introduction of strong acids oxidize the substance into graphene oxide. Oxidation weakens the chemical bonding thus creating a greater interlayer spacing between them. A final thermal shock of the graphene oxide at high temperature enables an opening of the structure creating graphene platelets with a thickness of 1-2 nm. Homemade graphene specimens were produced with a similar top-down approach using a commercially purchased 60 ml aqueous solution of graphene oxide (GO). Comprised of 5 g/L of graphene oxide, this highly concentrated solvent enables samples to be prepared of varying sizes and shapes. The graphene oxide used in the solution was approximately 79% carbon and 20% oxygen [14]. Ensuring that the graphene oxide mixture was uniformly and consistently spread over the entire sample area, the solution was placed in an ultrasonic cleaner. The uniformly mixed solvent was siphoned on to a polytetrafluoroethylene (PTFE) substrate and was dried using two methods: standard air-drying, as well as curing in a vacuum oven for 24 hours at 100°C and 70 mmHg below standard atmospheric pressure. (Air-dried samples developed a nonuniform profile with enclosed air bubbles

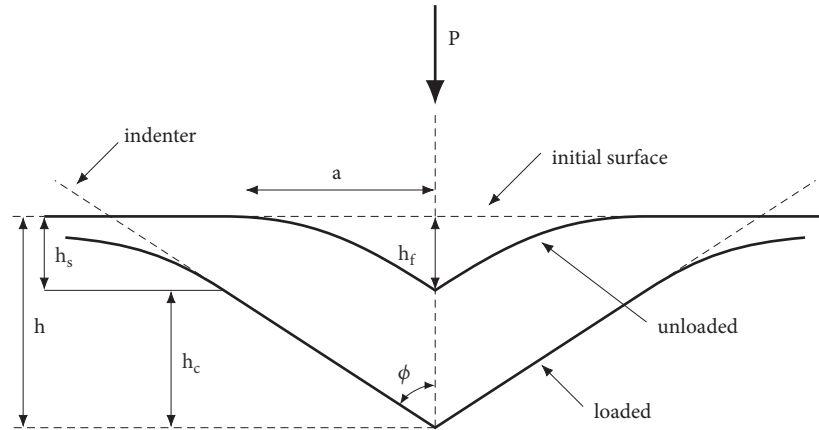


FIGURE 4: Ideal indentation depicting h_c and the initial linear portion of the unloading stage where stiffness is calculated.

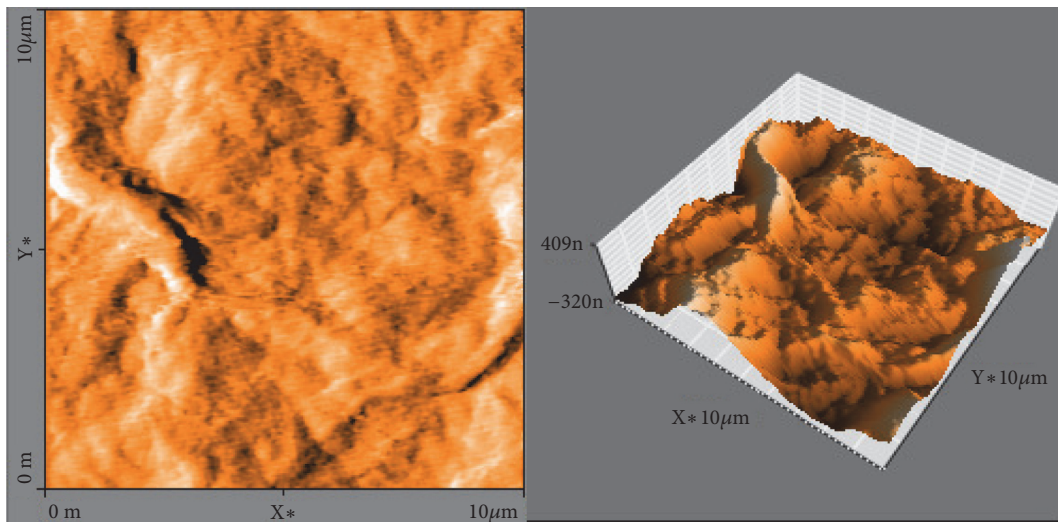


FIGURE 5: AFM image and three-dimensional topography of **air-dried graphene oxide solution** taken using the DD-ACTA probe. The sample shows a region of elevated height with crater structure seen in the upper left hand corner of the three-dimensional topography scan.

leading to vast deviations in topography and indentation characteristics.) Once cured the samples were adhered to a standard, writable compact disk in order to perform a thermal shock via the high intensity laser in a LightScribe drive resulting in oxygen reduction [15]. Producing graphene on PTFE substrates do not alter their composition and enable samples be easily transferred to the CD for oxygen reduction cycles or to glass slides for examination. AFM images of air-dried and vacuum-dried graphene oxide samples are shown in Figures 5 and 6, respectively.

Conversely, the commercially purchased graphene used for comparison was fabricated through chemical-vapor deposition (CVD), a bottom-up procedure. Though this process can grow graphene on various substrates such as copper or nickel, our samples were coated a sheet of aluminum foil. The graphene coating had an average thickness of 3.5 nm, and the lateral size of the individual graphene flakes were between 5-10 μm [9]. These flakes coated the surface to form a conductive layer. SEM images taken by the manufacturer

and AFM images showing similar flake patterns taken by our group are compared in Figures 7 and 8, respectively.

3.2. AFM Calibration. The first step in setting up the AFM for imaging and spectroscopic analysis involved mounting a probe. For this experiment, noncontact AppNano ACLA [16], contact AppNano SHOCON probes [17], and AppNano Diamond Doped ACTA probes (DD-ACTA) [18] were used. Mounting the probe on the cantilever holder was usually done with forceps, while vacuum tweezers were utilized when removing the probe for storage. Proper mounting proved crucial for ideal laser alignment and accurate measurements.

Once a probe had been mounted, the laser must be aligned on the probe tip. Alignment was achieved by adjusting the laser's position through a viewing port on the AFM. Course X/Y direction adjustments were performed first, while examining the laser working point meter provided in the Nanosurf EasyScan 2 software.

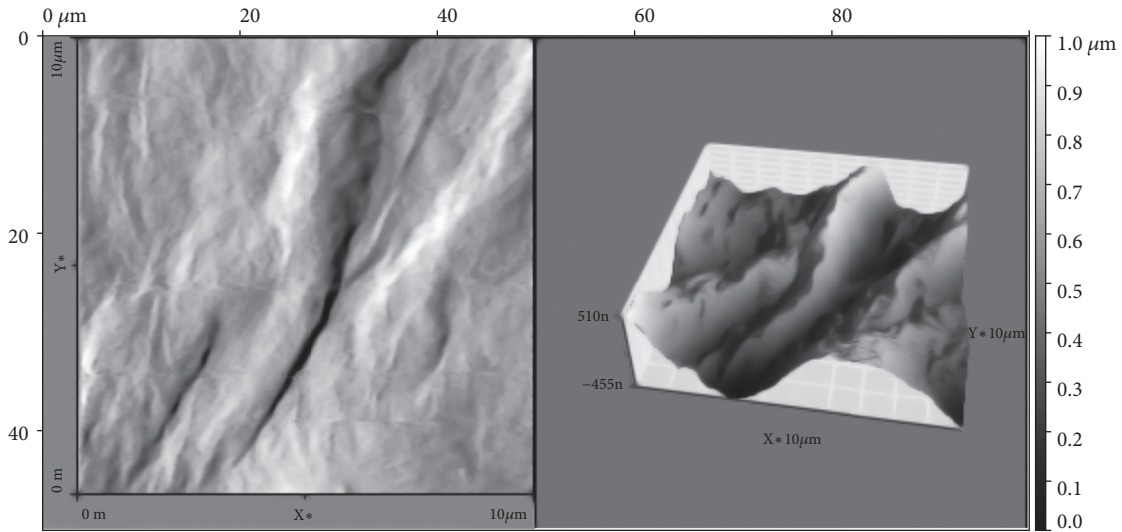


FIGURE 6: AFM image and three-dimensional topography of **vacuum oven-dried graphene oxide solution** taken using the DD-ACTA probe. A crevasse region runs through the center of the sample, with elevated regions on either side.

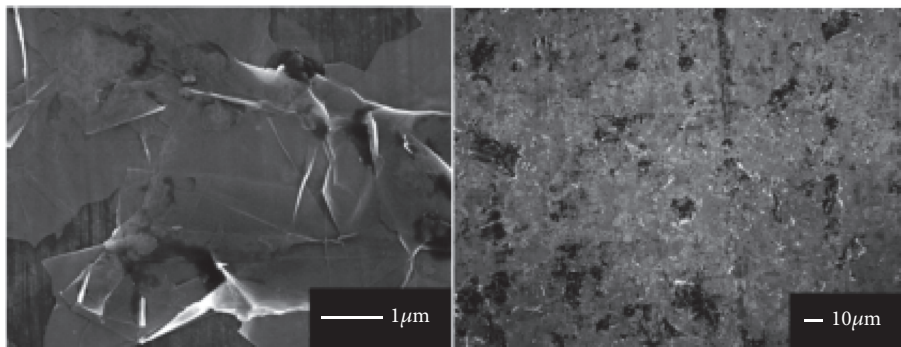


FIGURE 7: SEM images taken by the supplier of the graphene coated aluminum [9]. Although the $1\ \mu\text{m}$ resolution of one the suppliers images is greater than what the AFM can accurately image, the flake-like structures clearly resemble each other.

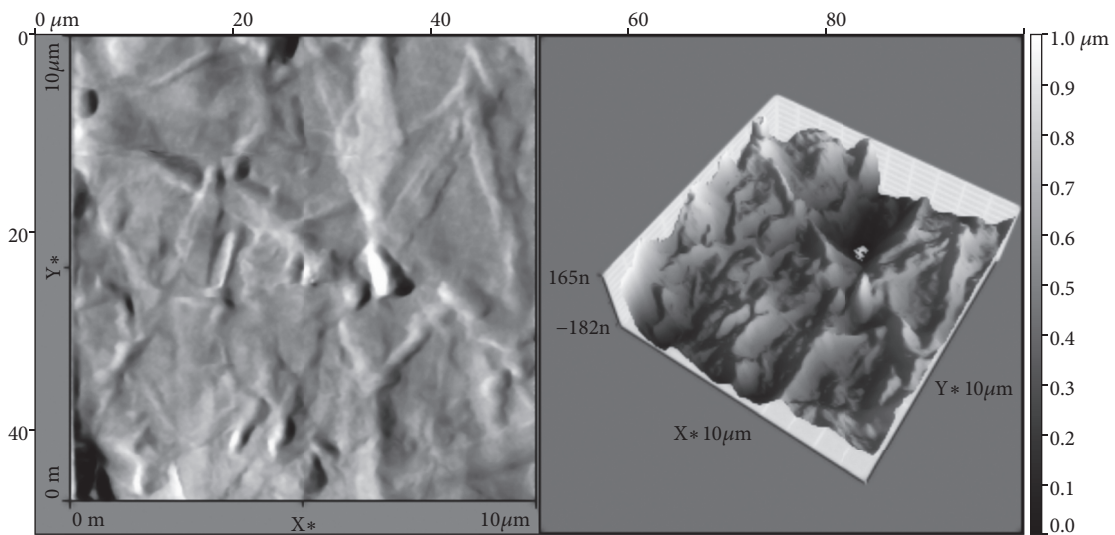


FIGURE 8: AFM image and three-dimensional topography of **commercially purchased graphene coated aluminum**. Again, graphene flakes are easily seen in the two-dimensional AFM image on the left. These images were taken using the DD-ACTA probe.

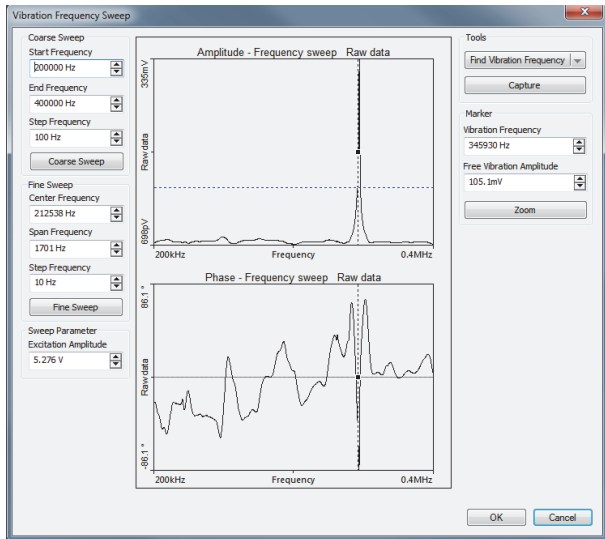


FIGURE 9: This figure shows the Vibration Frequency Search Dialogue for the Nanosurf EasyScan 2 software using the DD-ACTA probe. The frequency range was set between 200 and 400 kHz, with the peak frequency occurring at 346 kHz.

A coarse frequency sweep was then performed, again utilizing the Nanosurf EasyScan 2 software. Depending on the probe used, the frequency range was set (see the Start Frequency and End Frequency entries in the upper left corner of Figure 9) and a course sweep was performed to determine the free resonant frequency. This graph was then exported as a .plt file to the program *springconstant.exe*, which determines the experimental spring constant of the probe. In our experiment, the spring constant of the SHOCON contact probe was 0.148 N/m and that of the DD-ACTA probe was 40 N/m. Finding the experimental spring constant proved significant, as the manufacturer's specifications displayed a wide range with significant error. This value also allowed for force-distance curve measurements to be converted to Newtons rather than left as voltage based on the scan head calibration.

One final step before data could be collected involved determining the deflection sensitivity of the instrument. For this test, a hard sapphire crystal was used as a calibration tool. An indentation was performed and a force-distance graph was obtained. The slope of the unloading portion of the graph was determined using the measure length feature of the Nanosurf EasyScan 2 software. This value was given in units of Volts per meter. Based on these calibration measurements, the deflection sensitivity for the DD-ACTA probe was calculated to be 984 nm.

3.3. Images and Topography. Once calibrated, the AFM was used to image the samples as well as measure the stiffness, hardness, and reduced Young's modulus. Numerous images, as well as a total of thirty data points were taken for each sample after each trip through the LightScribe. At each data point, an indentation occurred, where the force of the loading and unloading phases were recorded on a

force-distance curve. This curve was then used to derive the above values as outlined in the Theory section. Ten different data points were selected on a $10\ \mu\text{m}$ by $10\ \mu\text{m}$ area on the sample before physically moving the sample to test another area. This process was repeated two additional times to obtain the thirty points, which were then averaged to obtain the final values. These values were recorded for the homemade samples after each trip through a LightScribe oxygen reduction cycle, as well as for the commercially purchased graphene. It is important to note, that the same sample could not be used throughout experimentation. After performing nanoindentation at thirty different points on the sample, the structure and hence the surface mechanical properties of the sample could be compromised. Because all the samples were made in the same way under the same circumstances, it was practical to use a different sample after each nanoindentation measurements without any loose of generality. As a result, a total of 7 samples were produced and tested: untreated air-dried graphene oxide, untreated vacuum oven-dried graphene oxide, 1 reduction cycle graphene oxide, 2 reduction cycle graphene oxide, 3 reduction cycle graphene oxide, 4 reduction cycle graphene oxide, and 5 reduction cycle graphene oxide.

3.4. RC Measurement. The laser-scribed graphene capacitor (LSGC) was built by first cutting kapton into two $2.5\ \text{cm} \times 2.5\ \text{cm}$ squares with $1\ \text{cm} \times 1\ \text{cm}$ leads attached to them. These squares were then adhered to the top of a LightScribe enabled DVD disc. A graphene oxide dispersion of $5\ \text{g/L}$ of water was then drop casted onto the adhered kapton substrates. The sample was then allowed to dry at ambient conditions. Once dried the disc was then inserted into the LightScribe DVD burner upside down allowing the laser to etch the surface. This process has then reduced the oxygen content in the graphene oxide, leaving us two graphene electrodes for our capacitor. After removing the electrodes from the disc they were sandwiched together with a Mylar dielectric in between them, which has a dielectric constant of 3.1 and a thickness of 25.4 microns. The graphene samples were also measured for their thickness using the Nanosurf EasyScan2 AFM. The LSG was shown to have a thickness of around 3-3.5 microns. As with the CVD made graphene capacitor, the aluminum substrate with the CVD graphene deposited onto it was cut into two $2.5\ \text{cm} \times 2.5\ \text{cm}$ squares with $1\ \text{cm} \times 1\ \text{cm}$ squares leads attached to them. The same Mylar substrate was used as a separator for this capacitor and constructed identically, but with aluminum instead of kapton.

4. Results and Discussion

4.1. AFM Images. Images were taken using the ACLA non-contact probe, the SHOCON contact probe, and the Diamond Doped ACTA probe. Image size varied between $10\ \mu\text{m}$ to $40\ \mu\text{m} \times 40\ \mu\text{m}$, with the time per line set between 0.6-0.8 seconds (1024 lines per image). Images of graphene oxide were taken before attempted reduction to graphene occurred, as well as after each trip through a LightScribe reduction cycle. Figure 10 shows an image of a graphene oxide

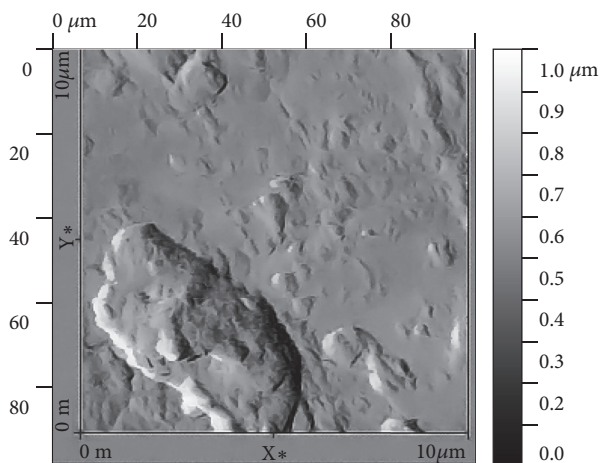


FIGURE 10: Image of a graphene oxide flake via SHOCON contact probe, taken prior to mixing into a solution to be reduced by the LightScribe. This is the only image taken of a graphene oxide flake that did not come purchased in premade solution.

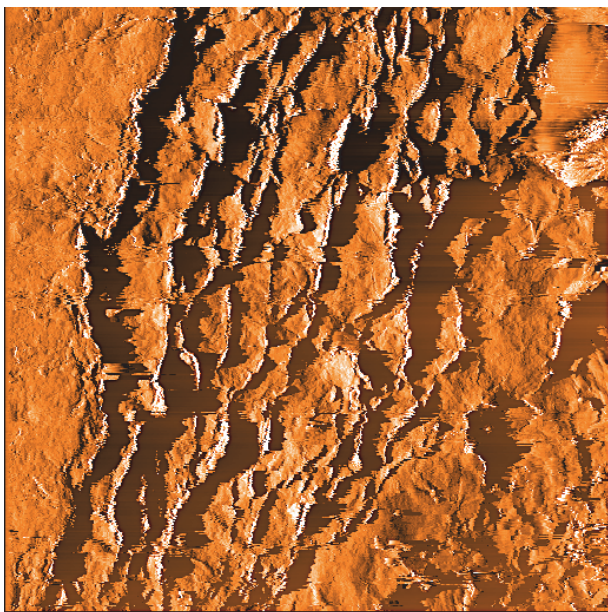


FIGURE 11: This image, taken with the SHOCON contact probe, clearly depicts the stratified nature of the graphene oxide sample. The scale length is $40\ \mu\text{m}$ by $40\ \mu\text{m}$ and the sample underwent 4 reduction cycles with the LightScribe.

flake before mixing it into a solution to be reduced by a LightScribe.

Images were then taken and were paired with their corresponding three-dimensional topography scan after each consecutive LightScribe reduction cycles. Representative images after the fourth and fifth oxygen reduction cycles are shown in Figures 11 and 12, respectively. Using this scan to perform three-dimensional analysis, it was possible to approximate both the number of layers of stacked graphene in the sample as well as an approximate height of the sample. Figure 11 represents AFM image of the graphene oxide sample after the

fourth reduction cycle with the LightScribe. Measurements of the various depths of the topography and edge positioning of the sample allowed for an approximation of the number of layers of stacked graphene to 5 layers. Figure 12 shows a two and three-dimensional images of AFM images after the fifth LightScribe reduction cycles of graphene oxide sample. Similar measurements of the various depths of the three-dimensional topography and edge positioning of the sample allowed for an approximation of the number of stacked graphene layers to 4-5 layers. As can be seen from these images, our group was able to produce high quality graphene oxide films with a simple cost-effective technique such as a LightScribe.

4.2. SEM Images. Towards the end of experiment, a scanning electron microscope (SEM) became available to image a 5 LightScribe reduction cycle sample. Figure 13 depicts flakes of graphene and stratified layers of the sample. The SEM was used to examine the sample from a larger scale. The image scales shown in the figure range from $100\text{--}500\ \mu\text{m}$. Attempts were made to take images on the same scale as the AFM ($10\text{--}40\ \mu\text{m}$) but the resolution of the table-top SEM was not clear enough.

4.3. Fourier Transform Infrared (FT-IR) Spectroscopy. Fourier transform infrared (FTIR) photoacoustic spectra in the $400\text{--}4000\ \text{cm}^{-1}$ were acquired by coadding 256 scans at a resolution of $8\ \text{cm}^{-1}$ using a Varian 7000 FTIR spectrometer equipped with a MTS300 photoacoustic module from MTEC Photoacoustics, Inc. USA. Rapid scan was used to obtain the spectra of graphene samples in the solid state. The final spectra were light intensity normalized using photoacoustic signals from a carbon black pellet under the same experimental conditions. A typical spectrum of untreated graphene oxide sample and after it has undergone one to five oxygen reductions cycles via LightScribe is shown in Figure 14. Detailed analysis of the spectra revealed that there is a decrease in intensity of those bands involving oxygen in the $1000\text{--}1800\ \text{cm}^{-1}$ (C-O stretching, C=O stretching, C-OH stretching, etc.) and $3500\ \text{cm}^{-1}$ (O-H stretching) regions upon reducing the graphene oxide samples [19]. The largest oxygen reduction has been observed after the second reduction cycle. There were not significant changes after the third reduction cycle because the LightScribe reached its maximum reduction capabilities after this cycle. This result is consistent with the mechanical properties changes observed in nanoindentation measurements as shown in Figures 16–18.

4.4. RC Analysis. Each capacitor was connected in series with a resistor with an input $60\ \text{kHz}$ AC square wave at $10\ \text{V}$ peak to peak. The output waveform was analyzed using the cursor function of an oscilloscope to find the RC time constants. This process was repeated for ten different resistors for each capacitor. The maintained voltage, the RC time constant, the capacitance, and the average surface charge density where all

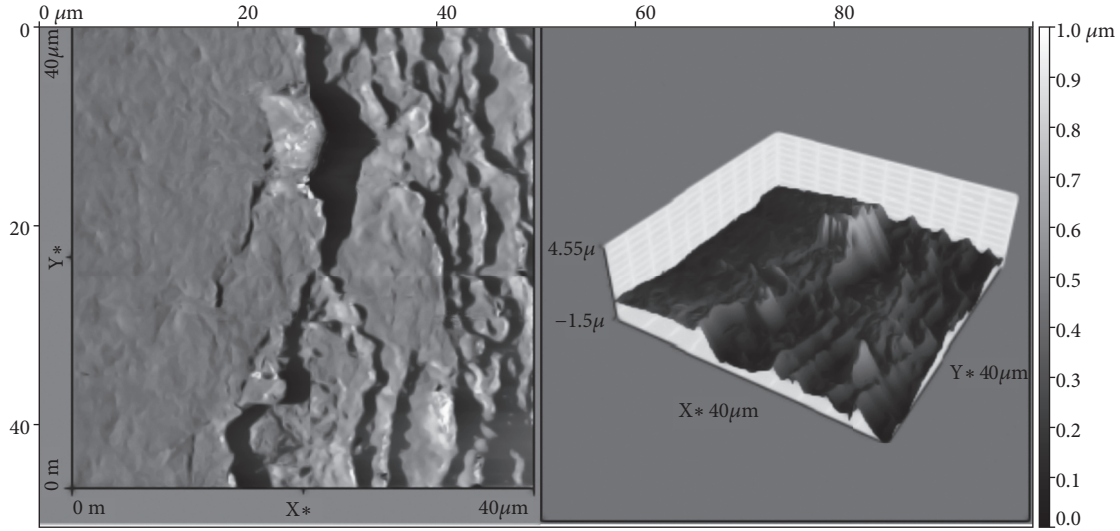


FIGURE 12: This image shows the edge of a sample of 5 LightScribe reduction cycle graphene oxide taken using the SHOCON contact probe. The three-dimensional topography and edge positioning of the sample allow for an approximation of the number of layers of stacked graphene. This sample contains 4-5 layers seen in the various height differentials.

TABLE 1: Data for the LightScribe graphene capacitor.

Resistance (kΩ)	Voltage Stored (V)	RC Time Constant (μ s)	Capacitance (pF)
22	9.75	1.00	45.54
66	9.40	1.60	24.24
100	8.55	2.05	20.50
200	6.40	3.95	19.75
300	4.73	4.30	14.33
400	3.72	4.60	11.50
470	3.22	4.20	8.94
500	3.08	4.70	9.40
600	2.68	5.02	8.33
700	2.16	5.10	7.14

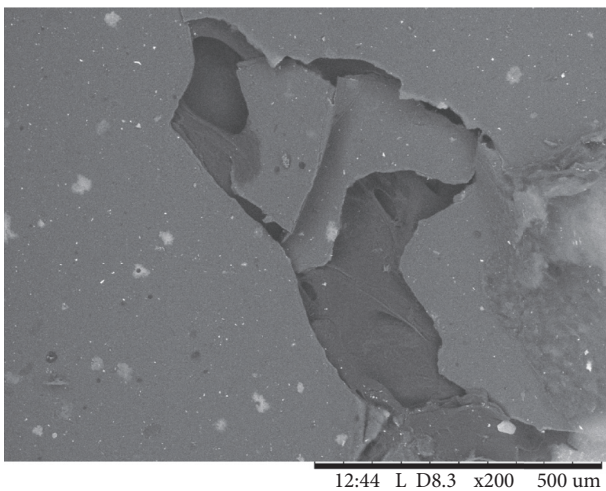


FIGURE 13: SEM image of graphene with stratified layers from 5 LightScribe reduction cycle sample.

measured. The surface charge density and RC time constants were calculated, respectively, with the equations

$$\sigma = \frac{Vk\epsilon_0}{d} \quad (6)$$

and

$$\tau = RC \quad (7)$$

where V is the average maintained voltage, k is the dielectric constant of Mylar, ϵ_0 is the permittivity of free space, d is the thickness of the Mylar separator, and σ is the surface charge density. A picture of one of the output waveforms can be seen in Figure 15 and the results are summarized in Tables 1 and 2.

The LSGC maintained a voltage of 24.5 times more than that of the CVDGC and had a surface charge density of 25.3 times more than that of the CVDGC. However the CVDGC had an RC time constant that was 29.12 times faster than the LSGC, and an average capacitance of 2.5 times more than the

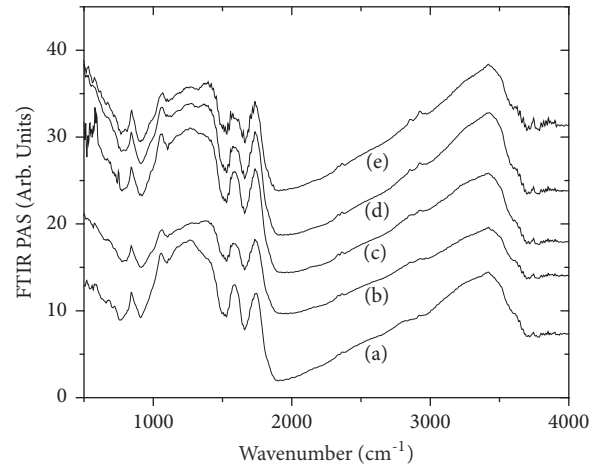


FIGURE 14: FTIR spectrum of homemade graphene oxide after one, two, and five oxygen reduction cycle.

TABLE 2: Data for the commercially purchased CVD graphene capacitor.

Resistance (k Ω)	Voltage Stored (V)	RC Time Constant (μ s)	Capacitance (pF)
22	9.75	1.00	45.54
66	9.40	1.60	24.24
100	8.55	2.05	20.50
200	6.40	3.95	19.75
300	4.73	4.30	14.33
400	3.72	4.60	11.50
470	3.22	4.20	8.94
500	3.08	4.70	9.40
600	2.68	5.02	8.33
700	2.16	5.10	7.14



FIGURE 15: Output waveform of the LSGC connected in series with a 100 k Ω resistor with an input 10V peak to peak square wave.

LSGC. These results may perhaps show a correlation between the graphene sample thickness and the electron mobility. For instance the LSGC graphene was almost 1000 times thicker than the CVDGC graphene, therefore having more surface

area and maintained a much higher voltage. On the other hand, the thinner CVDGC graphene was allowed to charge and discharge faster, showing higher electron mobility. From these findings we may be able to postulate that perhaps there is a correlation to the thickness of a graphene sample, and its ability to maintain and store more voltage at the cost of electron mobility.

4.5. Spectroscopic Analysis. Nanoindentation was performed on the various graphene oxide samples in order to calculate stiffness, hardness, reduced Young's modulus, and the max load applied. This process was done after two and three-dimensional imaging was performed to visualize the topography of the samples after each reduction cycle. A 15 μ m by 15 μ m grid of indentations were performed in three separate locations on each sample. Each grid was comprised of 10 indentations yielding a total of 30 spectroscopic points. Table 3 shows the average stiffness, hardness, P_{max} , and reduced Young's modulus of each sample across the 30 indentations. Therefore, all data discussed hereafter in this section reflects the average values of the data points.

The first samples tested were the unreduced graphene oxide. Although the oven-dried graphene oxide had slightly higher values in every category, the measurements were close

TABLE 3: The statistical analysis results for spectroscopic investigation of various samples. The values displayed are the averages of the thirty data points taken for each sample.

Sample	Stiffness (N/m)	Hardness (GPa)	E_r (GPa)	P_{max} (μ N)
0 Reduction Cycle	16.00	3.09	0.81	12.00
1 Reduction Cycle	16.48	3.70	1.18	9.77
2 Reduction Cycles	24.31	4.80	1.50	7.35
3 Reduction Cycles	23.64	5.02	1.61	11.50
4 Reduction Cycles	20.81	5.38	1.62	11.10
5 Reduction Cycles	22.39	5.52	1.61	10.40
Commercial Graphene Oxide	22.80	5.83	1.84	14.10

enough to determine that oven-drying the sample versus air-drying the sample did not significantly affect its material properties or the nanoindentation process.

The first reduction cycle, as expected, led to an increase in the stiffness, hardness, and reduced Young's modulus. The stiffness increased by 2.96% the hardness increased by 17.97%, and the reduced Young's modulus increased by 37.19%, compared to the unreduced graphene oxide.

The second LightScribe reduction cycle generated additional increases in values from a previous reduction cycle, the stiffness increased to 24.31 N/m, a 38.39% increase from the first reduction cycle. The hardness, now 4.80 GPa, showed a 25.88% increase from the previous reduction cycle and a 43.35% increase from the unreduced vacuum-dried graphene oxide sample. Lastly, 23.88% and 59.74% increases in the reduced Young's moduli were seen from the first reduction cycle and the unreduced vacuum-dried samples, respectively, bringing the value of the reduced Young's modulus to 1.50 GPa.

The third reduction cycle showed the first signs that the LightScribe DVD burner was reaching its maximum reduction capabilities. The stiffness decreases by 2.79%, while the hardness and the reduced Young's modulus only increased 4.48% and 7.07%, respectively, from the second reduction cycle. The overall percent increases from the unreduced graphene oxide after the third reduction cycle were 38.55% for the stiffness, 47.6% for the hardness, and 66.12% for Young's modulus.

The fourth and fifth LightScribe reduction cycles signify the maximum reduction capabilities of the DVD burner being reached, with minimal improvement from the third to fourth cycles and almost identical measurements from the fourth to the fifth cycles. The percent increases for the stiffness, hardness, and reduced Young's modulus from the third to the fourth reduction cycles were 12.73%, 6.92%, and 0.62%, respectively. Overall, the increases from the unreduced graphene oxide sample after the fourth reduction cycle were 26.13% for the stiffness, 54.07% for the hardness, and 66.7% for the reduced Young's modulus.

After the fifth and final LightScribe reduction cycle, the stiffness rose to a final value of 22.39 N/m, a 7.31% increase from the fourth cycle. The hardness topped out at 5.52 GPa, only a 2.57% increase from the previous cycle. Lastly, the reduced Young's modulus slightly decreased by 0.62% to a final value of 1.61 GPa. At this point in experimentation, the

maximum effectiveness of the LightScribe DVD burner had been reached, and further reduction cycles would not have altered the material properties a significant amount.

The LightScribe DVD burner was ultimately able to increase the stiffness, hardness, and reduced Young's modulus of the graphene oxide samples. The total percent increases from the unreduced graphene oxide sample to the fifth reduction cycle sample were 33.29% for the stiffness, 56.45% for the hardness, and 66.12% for the reduced Young's modulus.

After testing the final homemade sample, the commercially purchased graphene sample was then spectroscopically investigated via nanoindentation. As expected, the stiffness, hardness, and reduced Young's modulus were all greater than the highest values of the homemade samples (the 5 reduction cycle sample). The stiffness was 22.80 N/m, 1.81% greater than the stiffness of the 5 reduction cycle sample. The hardness was 5.83 GPa, 5.46% greater than the 5.52 GPa hardness of the 5 reduction cycle sample. Lastly, the reduced Young's modulus of the commercial graphene was 1.84 GPa, 13.33% greater than the 5 reduction cycle sample. Although the increase in stiffness, hardness, and the reduced Young's modulus were significant, the measurements were on the same order of magnitude as the 5 reduction cycle homemade graphene sample. This shows the potential for homemade graphene synthesis via DVD burner for reducing the amount of oxygen in graphene oxide.

4.6. Statistical Analysis. Examining Figures 16–18 allows for insight into the trends and range of the data, as well as some statistical analysis. First, discussing the stiffness, Figure 16 shows the black standard deviation bars. All of the samples have sections where the error bars, and thus the values overlap. This means that the stiffness between the unreduced sample and the 1 reduction cycle sample, for example, were within one standard deviation of each other. The same holds true for the difference in stiffness between the 1 reduction cycle sample and the 2 reduction cycle sample, the 2 reduction cycle and the 3 reduction cycle sample, etc. However, the second and third reduction cycle samples showed slight increase from the rest. This could be attributed to sample thickness that these two samples could be thicker than the rest. Nonetheless, after the second reduction cycle, we can again say with higher certainty that the graphene oxide sample increased in stiffness from the unreduced sample.

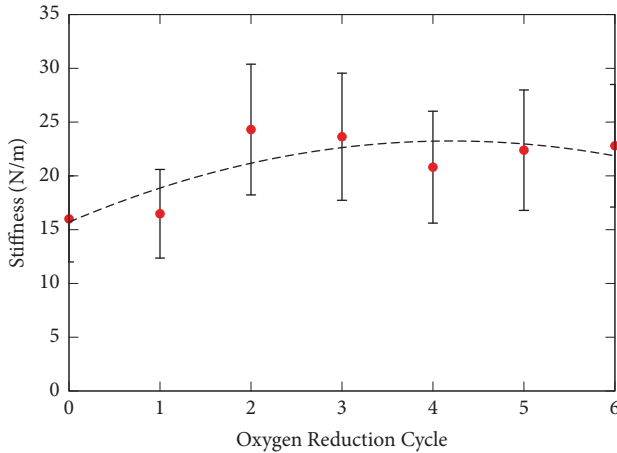


FIGURE 16: This plot compares the stiffness of the sample based on the number of LightScribe reduction cycles. The red points are the average values for the thirty data points taken after each cycle. In order to depict the changing nature of the stiffness, these points were fit using a polynomial function shown above. The error bars depict the standard deviation of the stiffness for the thirty data points taken after each reduction cycle.

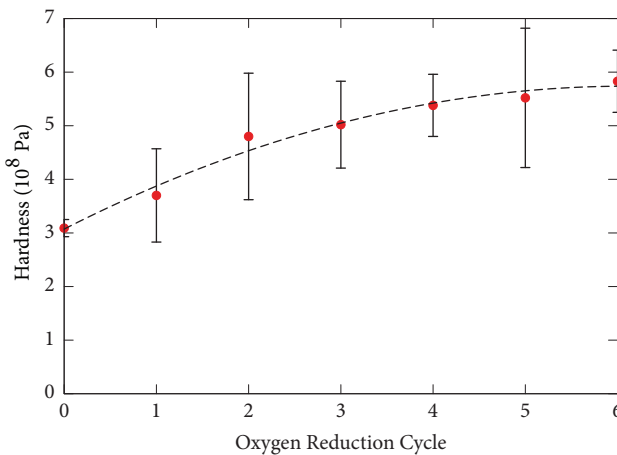


FIGURE 17: This plot compares the hardness of the sample based on the number of LightScribe reduction cycles. The red points are the average values for the thirty data points taken after each cycle. In order to depict the changing nature of the hardness, these points were fit using a polynomial function shown above. The hardness increased for the three reduction cycles before leveling off during the fourth and fifth cycles. The error bars depict the standard deviation of the hardness for the thirty data points taken after each reduction cycle.

The average values and the standard deviations of the hardness shown in Figure 17 must also be investigated. Unlike the stiffness, the standard deviation values of the hardness show greater overlapping regions. It was not until the fourth reduction cycle sample that we can be certain the hardness value increased as it differed from the unreduced sample by more than one standard deviation.

Lastly, Young's modulus data, Figure 18, more clearly exhibited that its value increased during the first and second

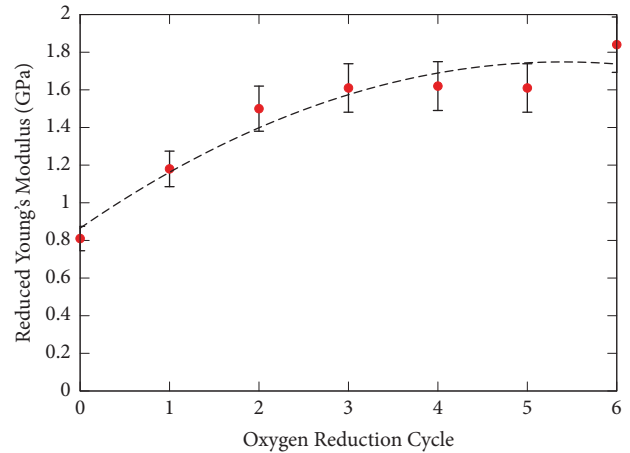


FIGURE 18: This plot compares the reduced Young's modulus of the sample based on the number of LightScribe reduction cycles. The red points are the average values for the thirty data points taken after each cycle. In order to depict the changing nature of the elastic modulus, these points were fit using a polynomial function shown above. The reduced Young's modulus increased for the first three reduction cycles before leveling off during the fourth and fifth cycles. The error bars depict the standard deviation of the reduced Young's modulus for the thirty data points taken after each reduction cycle.

cycles but leveled off after the third cycle. The reduced Young's modulus between the unreduced sample and the 2,3,4 and 5 reduction cycle samples were less than one standard deviation apart. Thus, the increase in the reduced Young's modulus was statistically significant after the first reduction cycle and required one more cycle until the increase in the elastic modulus was certain. Further, similar to the stiffness, the next statistically significant jump in the reduced Young's modulus occurred after the third, fourth, and fifth LightScribe reduction cycles. Thus, after the third reduction cycle, we can again say with higher statistical certainty that the graphene oxide sample's reduced Young's modulus increased from the first reduction cycle. Note that, the values of stiffness, hardness, and reduced Young's modulus for the homemade samples approached that of the commercially purchased sample (shown as the 6th Oxygen Reduction Cycle in Figures 16–18) but none of these values was greater than that of the commercial sample.

5. Conclusion

Although significant increases in the stiffness, hardness, and reduced Young's modulus were made via LightScribe reduction, the values obtained in this experiment differ drastically from those of pristine single layer graphene. The values of stiffness and hardness of graphene are not easily standardizable as they depend on the sample's thickness. Young's modulus of pristine graphene, however, is generally accepted to be around 1 TPa [20]. Our sample was definitely not pristine, thus accounting for the dramatically lower reduced Young's modulus. Our results, however, were

still much lower than other nonpristine samples. Work done by Gmez-Navarro [21] revealed Young's modulus of chemically derived single graphene sheets to be approximately 0.25 TPa. Here, the discrepancy in results can be attributed to the fact that our samples generally consisted of 3-5 layer graphene sheets. Also, it is possible that the LightScribe reduction process was not able to convert all of the layers to graphene, thus further lowering the elastic modulus. Importantly, one should note that although our homemade sample differed from the expected Young's modulus of single layer nonpristine graphene by a factor of 100, the commercially purchased sample also differed by the same factor of 100. This speaks to the current and prevalent issue of producing high quality graphene on a large scale. Production of single layer, defect free, pristine graphene proves incredibly challenging, even on a small scale. Improvements in large scale graphene production could usher in a new era of exciting technological and scientific advancements.

In future experiments, these results could be refined and improved. There were numerous sources of error throughout experimentation, one of the largest dealt with the determination of the contact area of the probe. An approximate contact area was determined using manufacturer specifications and force-distance curves, yet the probe tips were all slightly different and the error range in the specifications could vastly affect calculations. Further, the need to use a different sample for each reduction cycle added extra inconsistency to the nanoindentation. The nature of vacuum-drying the samples led to uneven thicknesses, thus every sample was different and comparisons of the mechanical properties across samples became more challenging and less precise. In the future, repeating these tests with different diamond tipped probes could also be beneficial. The DD-ACTA probes used were noncontact mode when imaging, thus using diamond tipped contact probes would be a good way to confirm the results of this project.

Lastly, various conditions in the lab affected the results. Noise arising from light sources, vibrations caused by air conditioning, and a not perfect mechanical vibrations isolation system all reduced the accuracy of the measurements. These factors also affected the images taken, which can be seen via the lines and blurred sections that appear in some images. This problem could be addressed in future experimentation by enclosing the AFM in a vibrationally isolated chamber to reduce these interference factors.

The findings of this research show that DVD burner reduction does show promise in converting graphene oxide to graphene. Using this technique, we have built, as a proof-of-concept, a graphene capacitor exhibiting the great potential of graphene as a supercapacitor for renewable wind and solar energy storages as well as electric cars. The values of stiffness, hardness, and reduced Young's modulus of homemade graphene were on the same order of magnitude as the commercially purchased samples. However, this method is not ideal for attempting to create pristine graphene, which still proves incredibly challenging and will continually be investigated for years to come.

Data Availability

The data used to support the findings of this study are available from the corresponding author upon request.

Conflicts of Interest

The authors declare that they have no conflicts of interest.

Acknowledgments

This work was partially supported by the Department of Physics and Astronomy and the School of Sciences and Mathematics at the College of Charleston. The work was also supported by NSF/EPSCoR: SC EPSCoR/IDeA, Award no. 0IA-1655740.

References

- [1] "A Short History of AFM," <http://hansmalab.physics.ucsb.edu/afmhistory.html#history>.
- [2] D. A. C. Brownson, D. K. Kampouris, and C. E. Banks, "An overview of graphene in energy production and storage applications," *Journal of Power Sources*, vol. 196, no. 11, pp. 4873–4885, 2011.
- [3] A. K. Geim and A. H. MacDonald, "Graphene: Exploring carbon flatland," *Physics Today*, vol. 60, no. 8, pp. 35–41, 2007.
- [4] V. C. Tung, M. J. Allen, Y. Yang, and R. B. Kaner, "High-throughput solution processing of large-scale graphene," *Nature Nanotechnology*, vol. 4, no. 1, pp. 25–29, 2009.
- [5] S. Bae, H. Kim, Y. Lee et al., "Roll-to-roll production of 30-inch graphene films for transparent electrodes," *Nature Nanotechnology*, vol. 5, no. 8, pp. 574–578, 2010.
- [6] K. S. Kim, Y. Zhao, and H. Jang, "Large-scale pattern growth of graphene films for stretchable transparent electrodes," *Nature*, vol. 457, no. 7230, pp. 706–710, 2009.
- [7] "Slim External Aluminum Slot-Loading BDXL Blu-Ray Writer," <http://www.pawtec.com/lightscribe/>.
- [8] JPK Instruments, "A Practical Guide to AFM Force Spectroscopy," 2008.
- [9] "Graphene Coated Aluminum," <https://graphene-supermarket.com/Graphene-on-Aluminum-Foil.html>.
- [10] Atomic Force Microscope, <http://www.nanosurf.com/?content=040230>.
- [11] P. Hermanowicz, M. Sarna, K. Burda, and H. Gabrys, "AtomicJ: An open source software for analysis of force curves," *Review of Scientific Instruments*, vol. 85, no. 6, Article ID 063703, 2014.
- [12] X. Li, H. Gao, C. J. Murphy, and K. K. Caswell, "Nanoindentation of Silver Nanowires," *Nano Letters*, vol. 3, no. 11, pp. 1495–1498, 2003.
- [13] W. D. Nix, *Materials Science and Engineering: A Structural Materials: Properties, Microstructure and Processing*, Stanford University, Department of Materials Science and Engineering, Stanjbrd CA, USA, 1997.
- [14] "Graphene Oxide Solution," https://graphene-supermarket.com/Highly_Concentrated_Graphene_Oxide_60-ml.html.
- [15] M. F. El-Kady and R. B. Kaner, "Scalable fabrication of high-power graphene micro-supercapacitors for flexible and on-chip energy storage," *Nature Communications*, vol. 4, article 1475, 2013.

- [16] “AppNano ACLA Probe,” <http://www.appnano.com/>.
- [17] “AppNano SHOCON Probe,” <http://www.appnano.com/>.
- [18] AppNano DD-ACTA Probe, <http://www.appnano.com/download/DD-ACTA.pdf>.
- [19] K. Krishnamoorthy, M. Veerapandian, K. Yun, and S.-J. Kim, “The chemical and structural analysis of graphene oxide with different degrees of oxidation,” *Carbon*, vol. 53, pp. 38–49, 2013.
- [20] K. S. Novoselov, V. I. Fal’ko, L. Colombo, P. R. Gellert, M. G. Schwab, and K. Kim, “A roadmap for graphene,” *Nature*, vol. 490, no. 7419, pp. 192–200, 2012.
- [21] C. Gómez-Navarro, M. Burghard, and K. Kern, “Elastic properties of chemically derived single graphene sheets,” *Nano Letters*, vol. 8, no. 7, pp. 2045–2049, 2008.

Research Article

Influence of Crystallization Time on Energy-Storage Density and Efficiency of Lead-Free $\text{Bi}_{0.5}(\text{Na}_{0.8}\text{K}_{0.2})_{0.5}\text{TiO}_3$ Thin Films

Ngo Duc Quan ^{1,2}, Tran Quoc Toan,^{3,4} and Vu Ngoc Hung²

¹School of Engineering Physics, Ha Noi University of Science and Technology, 1 Dai Co Viet Road, Hanoi 100000, Vietnam

²International Training Institute for Materials Science, Hanoi University of Science and Technology, 1 Dai Co Viet Road, Hanoi 100000, Vietnam

³Graduate University of Science and Technology, Vietnam Academy of Science and Technology, 18 Hoang Quoc Viet Road, Hanoi 100000, Vietnam

⁴Institute of Natural Products Chemistry, Vietnam Academy of Science and Technology, 18 Hoang Quoc Viet Road, Hanoi 100000, Vietnam

Correspondence should be addressed to Ngo Duc Quan; quan.ngoduc@hust.edu.vn

Received 7 September 2018; Revised 4 November 2018; Accepted 16 December 2018; Published 1 January 2019

Guest Editor: Hong Fang

Copyright © 2019 Ngo Duc Quan et al. This is an open access article distributed under the Creative Commons Attribution License, which permits unrestricted use, distribution, and reproduction in any medium, provided the original work is properly cited.

Lead-free $\text{Bi}_{0.5}(\text{Na}_{0.80}\text{K}_{0.20})_{0.5}\text{TiO}_3$ (BNKT) ferroelectric films were synthesized on Pt/Ti/SiO₂/Si substrates via chemical solution deposition. The influence of crystallization time on the microstructures and ferroelectric and energy-storage properties of the films was investigated in detail. The XRD analysis showed that the BNKT films have well crystallized corresponding to the single-phase perovskite structure at 700°C. Ferroelectric and energy-storage properties of the films were significantly enhanced by increasing crystallization time. With crystallization time of 60 min, the remnant polarization (P_r), maximum polarization (P_m), and $P_m - P_r$ values reached the highest values of 7.9 $\mu\text{C}/\text{cm}^2$, 28.9 $\mu\text{C}/\text{cm}^2$, and 21.0 $\mu\text{C}/\text{cm}^2$, respectively, under the electric field of 400 kV/cm. Thanks to the strong enhancement in P_m and the large $P_m - P_r$ value, the highest recoverable energy-storage density (J_{reco}) gets the value of 2.9 J/cm³. The obtained results indicate that the BNKT films have application potentials in advanced capacitors.

1. Introduction

Recently, people have faced big global challenges such as the air pollution, climate change, and the energy scarcity. For the sustainable development, the traditional fossil fuel energy resources should be replaced by new energy generation technologies, such as wind and solar and thermal energy with cleaner renewable sources. Hence, the development of the high energy-storage materials and devices has been paid increasing attention. The dielectric capacitors owning numerous good properties such as ultrafast charge-discharge rate, high energy-storage density (J_{reco}), good temperature stability, and low cost have been widely studied in the past decades. They have been used in a lot of modern electrical equipment, such as high power microwaves and electromagnetic armor. [1–5]. Because of the integrating and miniaturizing tendency of electronic devices, an ideal capacitor needs

to possess high energy-storage density, rapid discharge, and high energy-storage efficiency (η) [1, 6, 7]. Theoretically, the dielectric materials having the small remnant polarization (P_r), high saturated polarization (P_m), and high breakdown strength (BDS) are the most potential candidates [1]. By far, majority of studies on film capacitors have been just focused on lead-based materials (PZT) [5, 8–12]. However, owing to containing high Pb content, PZT-based materials are not environmentally friendly and likely harm the human health. Hence, the developments of lead-free materials with high J_{reco} and η are an urgent demand for the applications of pulsed power capacitors. Currently, lead-free ceramics, such as $(\text{K}_{0.5}\text{Na}_{0.5})\text{NbO}_3$ (KNN)-based [13], BaTiO_3 (BT)-based [14], SrTiO_3 (ST)-based [3], and $(\text{Bi}_{0.5}\text{Na}_{0.5})\text{TiO}_3$ (BNT)-based [15], have attracted much attention because of their good energy-storage properties. Among them, lead-free $(\text{Na}_{0.5}\text{Bi}_{0.5})\text{TiO}_3$ (NBT) ferroelectric materials have been

extensively investigated for mainly the past 10 years [16]. Smolenski and his coworkers [17] revealed NBT as typical perovskite-type ferroelectrics in 1961. When modified by other ABO_3 phases, the critical temperature at which the AF-AFE phase transition occurs could be reduced with an increase of ferroelectric properties. For example, NBT- x BT lead-free thick films [18] were studied on the temperature-dependence of the J_{reco} and leakage current performance. Authors attained the enhancement of the BDS and the $P_m - P_r$ value for NBT-0.06BT, resulting in the improvements of energy-storage properties (the maximum J_{reco} and η of 2.3 J/cm^3 and 45%, respectively at under 550 kV/cm). Xu and his coworkers [19] obtained the solid solubility of BNTBT with NBN and optimized energy-storage properties with $J_{\text{reco}} = 1.36 \text{ J}/\text{cm}^3$ and $\eta = 73.9\%$ at NBN content of 0.02. For the same system, Lu et al. [20], thanks to the La and Zr codoping, enhanced the energy-storage capacity of the BNTBT (the maximum J_{reco} was 1.21 J/cm^3 at 100 kV/cm). In the report [20], the energy-storage density of BNBT- x KN ceramics was explored with the rise of KN addition. Authors indicated that the energy-storage density is increased radically and reached the maximum value of 0.89 J/cm^3 at 100 kV/cm for BNBT-0.06KN. $(1-x)$ BNTBT- x NN ceramics [15], prepared via the conventional solid state reaction method, exhibit more slim $P-E$ loops with increasing the NN amount. Therefore, the J_{reco} was enhanced significantly and reached the highest value of 0.71 J/cm^3 for $x = 0.10$ at 7 kV/mm . Being similar AFE ceramic, $(1-x)(\text{Na}_{0.5}\text{Bi}_{0.5})\text{TiO}_3-x\text{SrTiO}_3$ (NBT-ST) system was reported by Cao et al. [21]. The 0.7NBT-0.3ST exhibited excellent temperature stability in its energy-storage density from the room temperature to 120°C with the maximum J_{reco} value of 0.65 J/cm^3 obtained at 65 kV/cm . Via a solid-solid state route, 0.475BNT-0.525BCTZ- x wt% MgO ceramics [22] were prepared and we investigated their phase structure, microstructure and dielectric and energy-storage properties with the focus on optimizing properties for capacitor applications. Thanks to significant enhancement of the dielectric breakdown strength in these ceramics with the addition of MgO, their discharge energy density was strongly improved. With a high dielectric breakdown strength of 15.67 kV/mm , the sample with $x = 5$ showed the highest maximum J_{reco} of 1.04 J/cm^3 . Comparing to bulk ceramics, the ferroelectric films having the higher BDS could release the drawbacks of bulk ceramics and be suitable for the high energy-storage applications. NBT films [23] synthesized on LNO/Si (100) substrates by using a sol-gel technique show the excellent energy-storage properties with the J_{reco} of 12.4 J/cm^3 and η of 43% at 1200 kV/cm . Zhang et al. [24] markedly enhanced the energy-storage properties of 0.7NBT-0.3ST relaxor films by the Mn^{2+} substitution for Ti^{4+} . With appropriate Mn doping (1mol. %), the highest J_{reco} value of 27 J/cm^3 was gained thanks to the high BDS value of 1894 kV/cm .

The above studies indicated that the energy-storage density was significantly improved by enlarging the difference value between P_m and P_r and/or increasing the value of breakdown strength (BDS). Enhancement of J_{reco} value in lead-free thin films has gained the progress, but their performances were still far inferior to those of lead-based

materials. The processing conditions of NBT-based films (such as the annealing temperature and crystallization time), which contribute closely to the quality and cost of products, were rarely studied. In the present study, we fabricated lead-free $\text{Bi}_{0.5}(\text{Na}_{0.8}\text{K}_{0.2})_{0.5}\text{TiO}_3$ (abbreviated as BNKT) films via a sol-gel method on Pt/Ti/SiO₂/Si substrates and investigated the energy-storage properties of BNKT films annealed at 700°C as a function of annealing time (10 min, 20 min, 40 min, and 60 min). We found that ferroelectric and energy-storage properties were enhanced when the annealing time was increased.

2. Materials and Methods

The $\text{Bi}_{0.5}(\text{Na}_{0.80}\text{K}_{0.20})_{0.5}\text{TiO}_3$ (BNKT) thin films were formed on Pt/Ti/SiO₂/Si substrates by a sol-gel technique. Here, the BNKT precursor solutions are derived from sodium nitrate (NaNO_3 , $\geq 99\%$, Sigma-Aldrich), potassium nitrate (KNO_3 , $\geq 99\%$, Sigma-Aldrich), bismuth nitrate ($\text{Bi}(\text{NO}_3)_3 \cdot 5\text{H}_2\text{O}$, $\geq 98\%$, Sigma-Aldrich), and titanium isopropoxide ($\text{Ti}[\text{i-OPr}]_4$, 99%, Sigma-Aldrich). Acetic acid and 2-methoxyethanol were chosen as cosolvent, and acetylacetones were chosen as ligands. During the process, titanium isopropoxide was at first dissolved in acetylacetone to prevent its hydrolysis. In order to compensate the possible Na and K loss during high temperature annealing, we added their excess amounts of 30% and 20%, respectively. The mixture was stirred at 70°C for 6 hours constantly to form the final solution until a 0.4 M transparent and stable yellow precursor solution was obtained. Each layer of the BNKT films was formed by spin coating 0.4 M precursor on substrates at 4000 rpm for 30 s, followed by pyrolysis at 400°C for 10 min. The process was repeated until the BNKT thin films with the required coating layers were obtained. Finally, BNKT thin films were annealed at 700°C in different periods (10 min, 20 min, 40 min, and 60 min) to obtain the ferroelectric phase. For the convenience, these films were named as T10, T20, T40, and T60, respectively.

Characteristics of the films as the cross-sectional and surface morphologies were detected by a field emission scanning electron microscope (FE-SEM, Hitachi S4800) and atomic force microscopy (AFM, Bruker Dimension ICON). The crystal structures of BNKT thin films were characterized by a Bruker D5005 diffractometer using Cu-K α radiation ($\lambda = 1.5406 \text{ \AA}$). $P-E$ hysteresis loops were measured under the applied voltages ranging from -25 V to 25 V, frequency of 1000 Hz by using a TF Analyzer 2000 ferroelectric tester (aixACCT Systems GmbH, Germany).

3. Results and Discussion

The BNKT films, after a synthesis, were investigated to check the surface morphology and roughness by using the SEM and AFM techniques. The two-dimensional (2D) and three-dimensional (3D) AFM images for the BNKT films scanned over a surface area of 40 $\mu\text{m} \times 40 \mu\text{m}$ were described in detail in Figures 1(a)-1(d). The AFM images revealed the densely packed, crack-free, uniform surfaces with the grains possessing columnar shape. The roots mean square

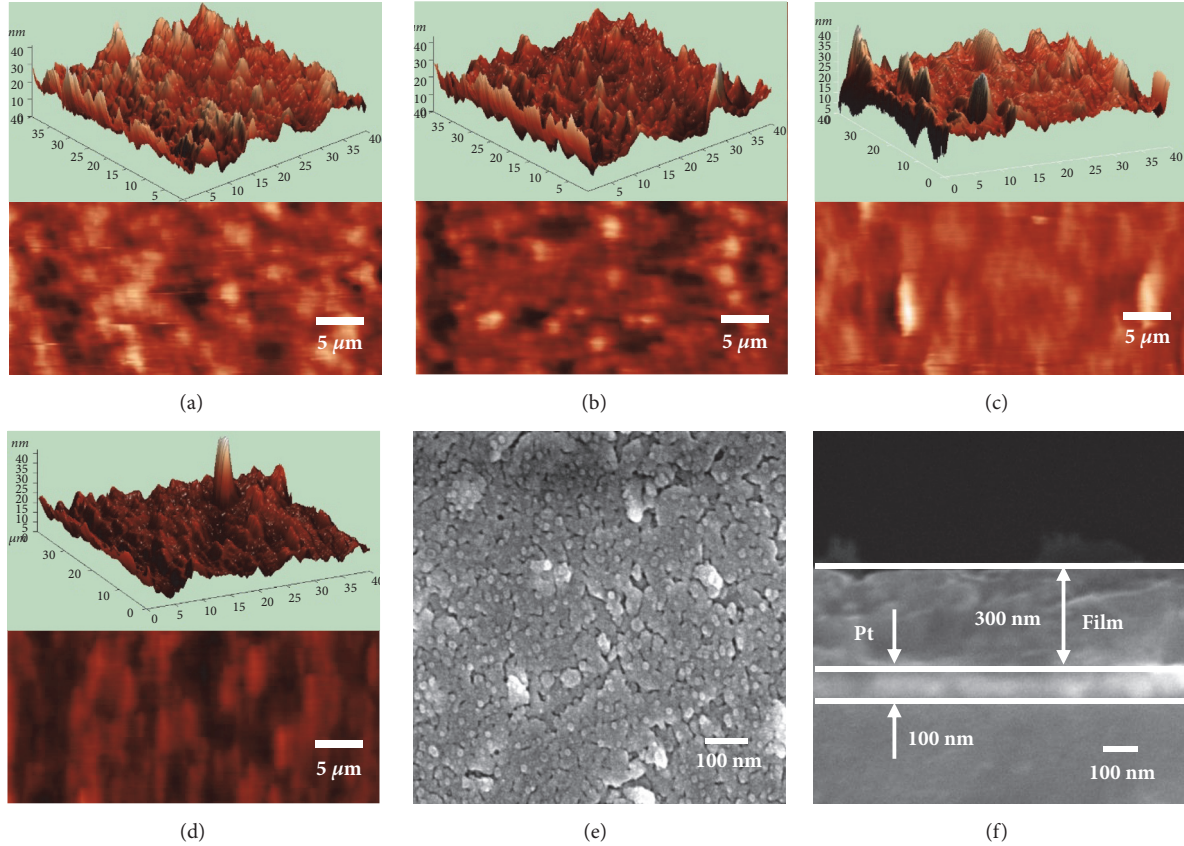


FIGURE 1: Two-dimensional (2D) and three-dimensional (3D) AFM images of BNKT films: (a) T10, (b) T20, (c) T40, (d) T60, (e) FE-SEM micrographs of sample T60, and (f) cross-sectional SEM image of sample T60.

surface roughness (R_{rms}) was calculated and shown in the Table 1. R_{rms} possesses the values of 5.5, 4.8, 4.6, and 3.8 nm corresponding to the BNKT films: T10, T20, T40, and T60. The low R_{rms} values of the film surfaces evidence a smooth morphology. The decrease of R_{rms} with annealing time is mainly due to the growth of BNKT crystallite with smaller grain boundaries merged into larger ones. The surface morphology of the BNKT thin films, therefore, becomes denser with an increase of the annealing time. This AFM result was also consistent with the analysis exposed by the XRD characterization and FE-SEM micrographs. In Figure 1(e), we demonstrated the FE-SEM micrograph of sample T60 annealed in 60 min. This thin film was shown to exhibit a dense and smooth surface consisting of tetragonal grain size particles without any traces of cracks detected. Figure 1(f) displayed the cross-sectional FE-SEM image of the T60 film. Based on this analysis, we can determine thicknesses of films, around 300 nm.

The BNKT thin film structure was measured with a θ - 2θ mode in steps of 0.02° . Figure 2(a) displays the XRD patterns of the BNKT films associated with the conditions of annealed at 700°C for different durations. The angular peak positions of the XRD signals are observed at around 2θ : 31.2° , 39.8° , 47.3° , and 58.0° corresponding to the BNKT bulk [24]. With the surpassed intensity, the (111) orientation located at $2\theta \sim 39.8^\circ$ is the mixture of orientations, deriving

from the Pt coated substrate. All other peaks belong to a single-phase perovskite structure with no other impurity phases detected, which agrees with our recent report [25] on influence of crystallization temperature on multiferroic behaviour of BNKT films. This observation also matches our previous works [26, 27] where they indicated that BNKT thin films possess simultaneously the rhombohedral and tetragonal symmetries. Among the typical orientations of the perovskite structure, the (110)/(200) peaks possess high intensity and therefore are the preferred orientations of the films. These intensity peaks were demonstrated in Figures 2(b) and 2(c) with the 2θ ranges: (b) 30.0° – 34.0° and (c) 46.0° – 48.5° . Analysed result shows that the (200) peak intensity of the BNKT films obviously tends to rise when annealing time increases from 10 min to 60 min. The full width at half maximum (FWHM) evaluated from the XRD patterns declines with increasing annealing time. This proved that the grain size enlarged as the annealing time was increased. To specify, we evaluated the grain size of films by using Scherrer equation [28]:

$$D = \frac{K \cdot \lambda}{\beta \cdot \cos \theta} \quad (1)$$

where D , K , λ , β , and θ are grain size, constant of crystallite shape (normally taken as 0.9), wave length, FWHM, and

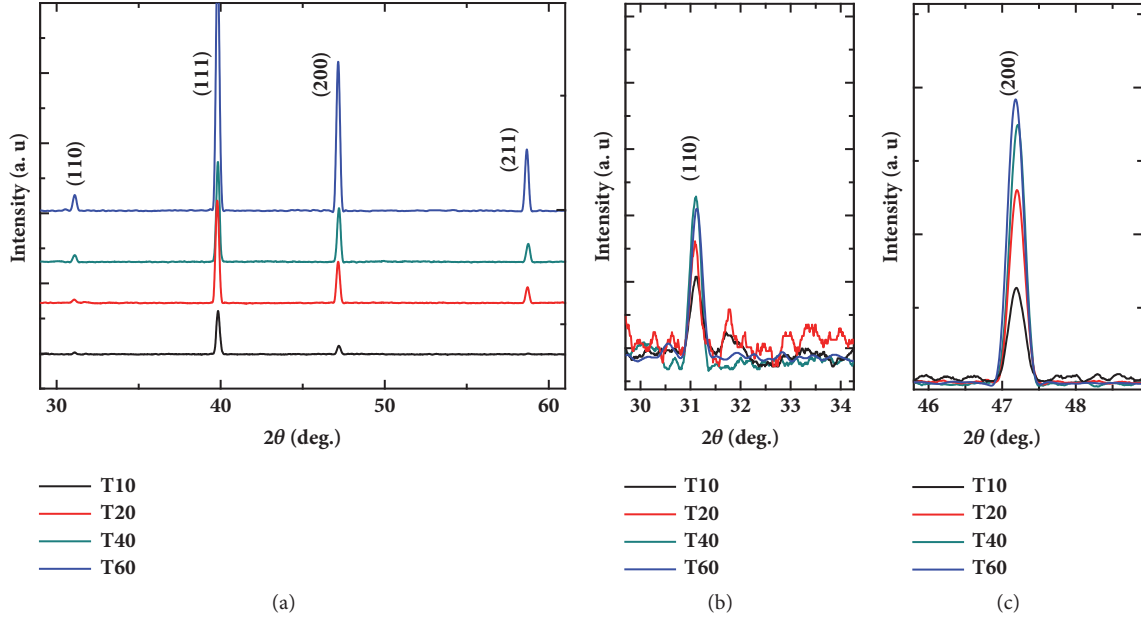


FIGURE 2: X-ray diffraction patterns of BNKT films in the 2θ ranges of (a) 28.0° – 62.0° , (b) 30.0° – 34.0° , and (c) 46.0° – 48.5° .

TABLE 1: The grain size and roots mean square roughness as a function of the annealing time.

Annealing time (min)	10	20	40	60
Grain size, D (nm)	44.9	47.2	49.1	49.7
Roots mean square roughness, R_{rms} (nm)	5.5	4.8	4.6	3.8

Bragg angle, respectively. The grain size was calculated and illustrated as a function of the annealing time in the Table 1. D value increased significantly from 44.9 nm for the film T10 to 49.7 nm for the film T60.

Furthermore, the XRD analysis about the film structure was confirmed by Raman technique with higher sensitivity. Figures 3(a)–3(d) show the Raman spectra of BNKT films as a function of crystallization time in the wavenumber ranges of 100 – 1000 cm^{-1} at room temperature. Lorentzian fitting technique was employed to expose the typical peaks of a perovskite structure. The Raman result is consistent with previous work on BNKTS ceramics [29], where it reported that $A_1(\text{TO1})$ mode at ~ 138 cm^{-1} is assigned to the A -site vibrations. For the film, this mode corresponds to the wavenumber of 118 cm^{-1} . We also observed the $B_1(\text{TO1})$ mode at 281 cm^{-1} , assigned to O-Ti-O bending motion [30]. Especially, Chen and his coworkers [29, 31] revealed the modes at higher wavenumbers, such as the $A_1(\text{TO3})$ at 525 cm^{-1} and $E(\text{LO})$ at 615 cm^{-1} characterizing for vibrations of TiO_6 oxygen octahedral. For our study, these modes are located at 514 cm^{-1} and 590 cm^{-1} , respectively. The wavenumber differences may be caused by the residual stress formed by film/substrate interface. Similar behaviour is also observed in our recent works [25, 32].

Ferroelectric properties of the BNKT films were examined by using a TF Analyzer 2000 ferroelectric tester at 1 kHz at room temperature. Figures 4(a)–4(d) illustrate the

P - E loops for the BNKT films with different crystallization times. In Figure 4, the P_m , P_r , and $P_m - P_r$ values of the films were evaluated and analysed. An obvious enhancement of the ferroelectricity can be observed as the annealing time increases. When being annealed in 10 min, BNKT films show a relatively poor ferroelectricity with small P_m , P_r , and $P_m - P_r$ values of around 18.9 $\mu\text{C}/\text{cm}^2$, 4.1 $\mu\text{C}/\text{cm}^2$, and 14.8 $\mu\text{C}/\text{cm}^2$, respectively. These values continuously increase as the annealing time is raised. Especially, at annealing time of 60 min, the P_m , P_r , and $P_m - P_r$ reach their highest values of around 28.9 $\mu\text{C}/\text{cm}^2$, 7.9 $\mu\text{C}/\text{cm}^2$, and 21.0 $\mu\text{C}/\text{cm}^2$, respectively. The increase in the ferroelectric properties matches up the grain size change and phase transition observed from the XRD analysis. With the annealing time ≥ 60 min, the intermediate pyrochlore phase completely transformed into the perovskite phase, and therefore the polarization in the film is improved. Furthermore, BNKT films revealed a great difference between the maximum polarization (P_m) and remnant polarization (P_r). Ahn and his coworkers [33] also reported similar behaviour, which resulted from the strong transform in the domain configuration between the states: (i) applying the electric field and (ii) removing the electric field. Because of the tensile stress at the film/substrate interface, domains may easily switch their original states as the electric field decreases to zero, leading to the small net polarization. By contrast, at a high electric field, BNKT films reach the spontaneous polarization of the bulk materials thanks to the

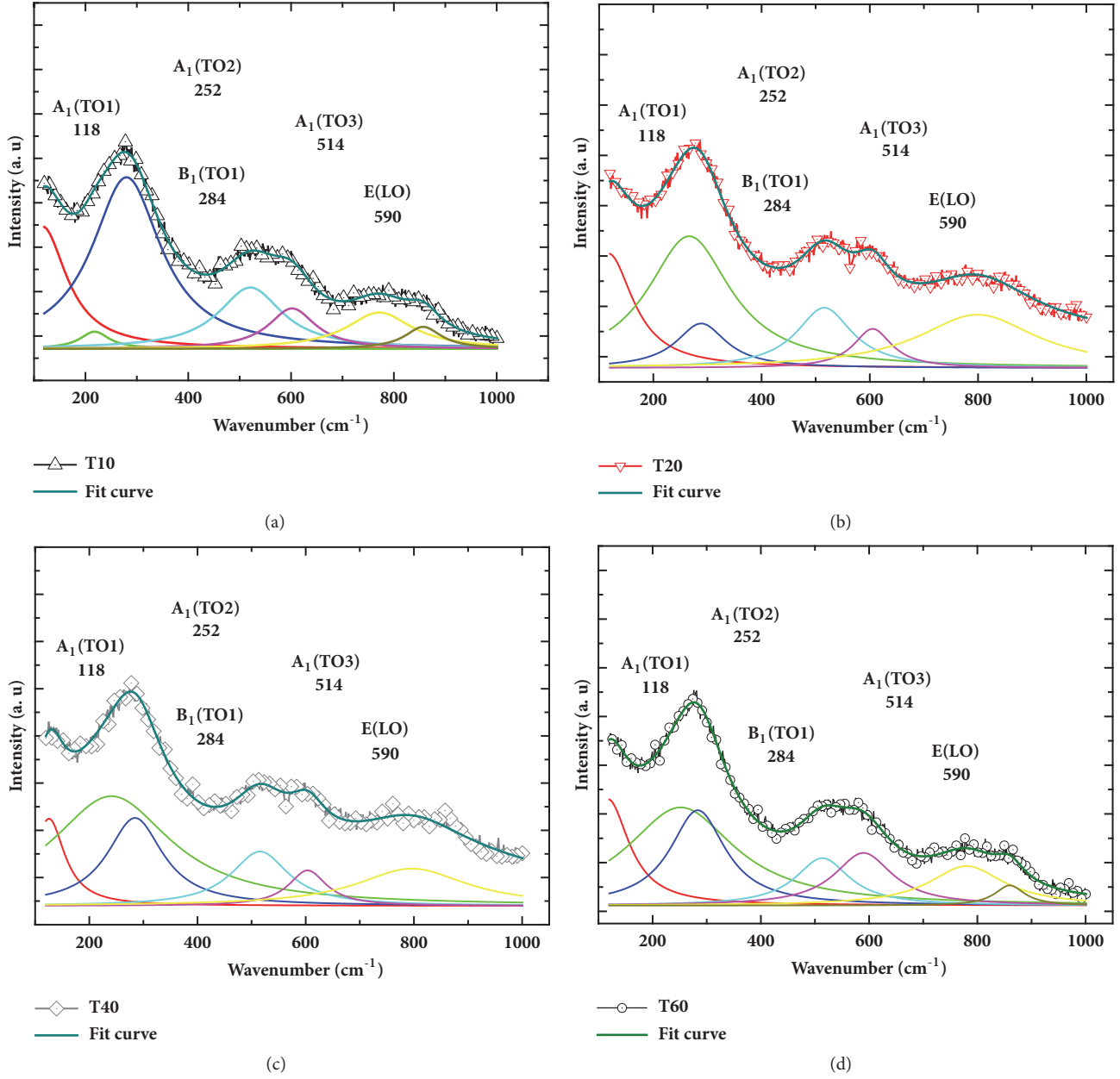


FIGURE 3: Raman spectra of BNKT films with different annealing times in the wavenumber ranges of 100–1000 cm^{-1} .

domain reorientation induced by the applied electric field. A high ($P_m - P_r$) value is a useful parameter for the energy-storage devices.

The energy-storage properties of the BNKT films were calculated based on the schematic diagram in Figure 5(a). J_{reco} is the recoverable electrical-energy density stored in the dielectric films and calculated from P - E hysteresis loops by the following expression [34]:

$$J_{\text{reco}} = \int_{P_r}^{P_m} EdP \quad (2)$$

where E refers to the applied electric field and P_m and P_r are the maximum and remnant polarization values, respectively. J_{loss} is the energy corresponding to the inherent hysteresis in the material. It is defined as numerical integration of closed area of the hysteresis loops (Figure 5(a)). The total energy (J_{total}) needs to charge a ferroelectric capacitor which is the sum of dielectric losses (J_{loss}) and recoverable (J_{reco}) energy. Thus, J_{loss} and J_{total} can be represented as

$$J_{\text{loss}} = \int_0^{P_r} EdP \quad (3)$$

and $J_{\text{total}} = J_{\text{reco}} + J_{\text{loss}}$

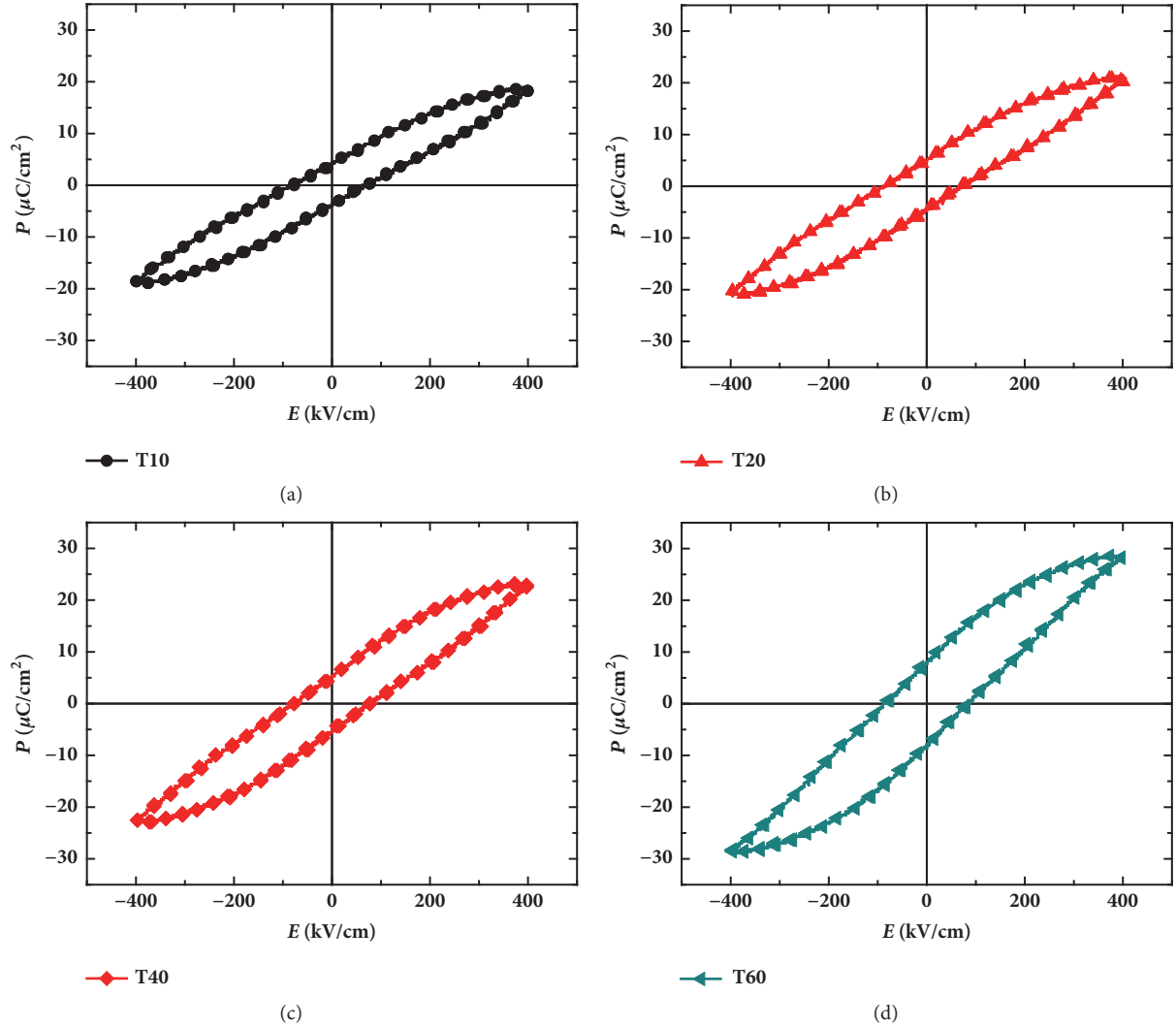


FIGURE 4: P-E ferroelectric hysteresis loops of BNKT films with different crystallization times at the same applied electric field of 400 kV/cm.

Based on (2) and (3), η value of the material can be calculated as follows:

$$\eta = \frac{J_{reco}}{J_{reco} + J_{loss}} \times 100 \quad (4)$$

Figure 5(b) demonstrates energy-storage density (J_{reco}), energy loss density (J_{loss}), and energy-storage efficiency (η) of the BNKT films as a function of crystallization time at applied electric field E_{appl} of 400 kV/cm. While J_{reco} and J_{loss} experience an increasing trend with a rise of crystallization time, the opposite is true of η . The BNKT films, annealed in 10 min, possess the small J_{reco} and J_{loss} values of 2.2 J/cm³ and 1.2 J/cm³, respectively. J_{reco} continuously increases from 2.2 J/cm³ to 2.9 J/cm³ as crystallization time rises from 10 min to 60 min. Similarly, J_{loss} reaches the highest value of about 2.0 J/cm³. J_{reco} is obviously enhanced with an increase of annealing time. This matches up the improved polarization as analysed in Figure 4. But η follows a downward trend from 65.0% to 59.3%. This behaviour is related to an increase of the coercive electric field, caused by oxygen vacancies.

When the BNKT films are annealed at high temperature, A-site metals (such as Bi³⁺, Na⁺, K⁺) are evaporated, forming oxygen vacancies. With such J_{reco} and η values, the BNKT films are comparable with other lead-free films in terms of energy-storage ability and have potential application for electrostatic energy-storage devices.

4. Conclusions

Lead-free Bi_{0.5}(Na_{0.80}K_{0.20})_{0.5}TiO₃ ferroelectric films have been successfully fabricated on Pt/Ti/SiO₂/Si substrates via a spin coating assisted sol-gel method. The experimental results showed that all the films have well crystallized corresponding to the single-phase perovskite structure and no other impurity phases are detected. BNKT thin films obtained a significant enhancement in ferroelectric properties and energy-storage density by increasing the crystallization time. P_m and P_r of films reached their highest values of around 28.9 $\mu\text{C}/\text{cm}^2$ and 7.9 $\mu\text{C}/\text{cm}^2$, respectively, thanks to rising the crystallization time from 10 min to 60 min. Because

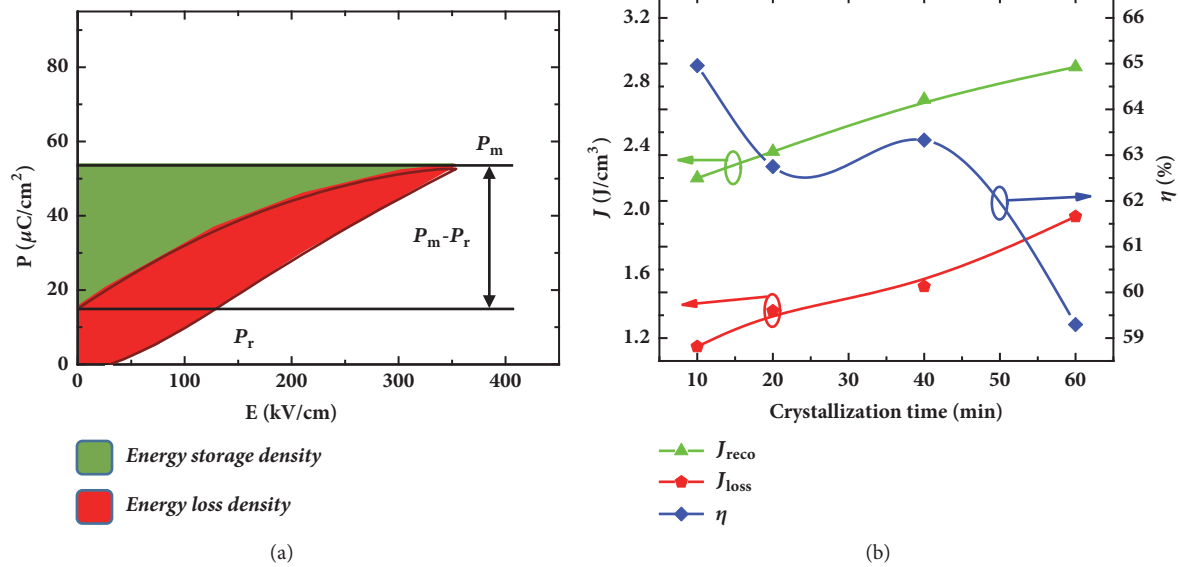


FIGURE 5: (a) Schematic diagram for the calculation of energy-storage properties of ferroelectric films, (b) energy-storage density (J_{reco}), energy loss density (J_{loss}), and energy-storage efficiency (η) of BNKT films at applied electric field E_{appl} of 400 kV/cm.

of large ($P_m - P_r$) polarization difference, J_{reco} got the maximum value of 2.9 J/cm³. The obtained advantages are due to the intermediate pyrochlore phase which is completely transformed into the perovskite phase.

Data Availability

The data used to support the findings of this study are included within the article.

Conflicts of Interest

The authors declare that they have no conflicts of interest.

Acknowledgments

This research is funded by Vietnam National Foundation for Science and Technology Development (NAFOSTED) under grant number 103.02-2017.21.

References

- [1] N. H. Fletcher, A. D. Hilton, and B. W. Ricketts, "Optimization of energy storage density in ceramic capacitors," *Journal of Physics D: Applied Physics*, vol. 29, no. 1, pp. 253–258, 1996.
- [2] Y. Hao, X. Wang, K. Bi et al., "Significantly enhanced energy storage performance promoted by ultimate sized ferroelectric BaTiO₃ fillers in nanocomposite films," *Nano Energy*, vol. 31, pp. 49–56, 2017.
- [3] H. Pan, Y. Zeng, Y. Shen et al., "BiFeO₃-SrTiO₃ thin film as a new lead-free relaxor-ferroelectric capacitor with ultrahigh energy storage performance," *Journal of Materials Chemistry A*, vol. 5, no. 12, pp. 5920–5926, 2017.
- [4] Y. Zhao, W. Yang, Y. Zhou et al., "Influence of molecular weight on the dielectric and energy storage properties of poly(vinylidene fluoride)," *Electronic Materials Letters*, vol. 12, no. 6, pp. 779–783, 2016.
- [5] M. D. Nguyen, E. P. Houwman, M. Dekkers, C. T. Q. Nguyen, H. N. Vu, and G. Rijnders, "Research Update: Enhanced energy storage density and energy efficiency of epitaxial Pb_{0.9}La_{0.1}(Zr_{0.52}Ti_{0.48})O₃ relaxor-ferroelectric thin-films deposited on silicon by pulsed laser deposition," *APL Materials*, vol. 4, no. 8, 2016.
- [6] I. Burn and D. M. Smyth, "Energy storage in ceramic dielectrics," *Journal of Materials Science*, vol. 7, no. 3, pp. 339–343, 1972.
- [7] G. R. Love, "Energy Storage in Ceramic Dielectrics," *Journal of the American Ceramic Society*, vol. 73, no. 2, pp. 323–328, 1990.
- [8] X. Hao, J. Zhai, and X. Yao, "Improved energy storage performance and fatigue endurance of Sr-Doped PbZrO₃ antiferroelectric thin films," *Journal of the American Ceramic Society*, vol. 92, no. 5, pp. 1133–1135, 2009.
- [9] M. Ye, Q. Sun, X. Chen, Z. Jiang, and F. Wang, "Effect of Eu doping on the electrical properties and energy storage performance of PbZrO₃ antiferroelectric thin films," *Journal of the American Ceramic Society*, vol. 94, no. 10, pp. 3234–3236, 2011.
- [10] S. Tong, B. Ma, M. Narayanan et al., "Lead lanthanum zirconate titanate ceramic thin films for energy storage," *ACS Applied Materials & Interfaces*, vol. 5, no. 4, pp. 1474–1480, 2013.
- [11] Z. Hu, B. Ma, S. Liu, M. Narayanan, and U. Balachandran, "Relaxor behavior and energy storage performance of ferroelectric PLZT thin films with different Zr/Ti ratios," *Ceramics International*, vol. 40, no. 1, pp. 557–562, 2014.
- [12] B. Peng, Q. Zhang, X. Li et al., "Large Energy Storage Density and High Thermal Stability in a Highly Textured (111)-Oriented Pb_{0.8}Ba_{0.2}ZrO₃ Relaxor Thin Film with the Coexistence of Antiferroelectric and Ferroelectric Phases," *ACS Applied Materials & Interfaces*, vol. 7, pp. 13512–13517, 2015.

- [13] A. Chauhan, S. Patel, and R. Vaish, "Mechanical confinement for improved energy storage density in BNT-BT-KNN lead-free ceramic capacitors," *AIP Advances*, vol. 4, no. 8, 2014.
- [14] P. Ge, X. Tang, Q. Liu, Y. Jiang, W. Li, and J. Luo, "Energy storage properties and electrocaloric effect of Ba_{0.65}Sr_{0.35}TiO₃ ceramics near room temperature," *Journal of Materials Science: Materials in Electronics*, vol. 29, no. 2, pp. 1075–1081, 2017.
- [15] Q. Xu, T. Li, H. Hao et al., "Enhanced energy storage properties of NaNbO₃ modified Bi_{0.5}Na_{0.5}TiO₃ based ceramics," *Journal of the European Ceramic Society*, vol. 35, no. 2, pp. 545–553, 2015.
- [16] N. D. Quan, L. Huu Bac, D. V. Thiet, V. N. Hung, and D. D. Dung, "Current development in lead-free Bi_{0.5}(Na,K)_{0.5}TiO₃-based piezoelectric materials," *Advances in Materials Science and Engineering*, vol. 2014, pp. 1–13, 2014.
- [17] G. Smolenskii, V. Isupov, A. Agranovskaya, and N. Krainik, "New ferroelectrics of complex composition," *Soviet Physics-Solid State*, vol. 2, pp. 2651–2654, 1961.
- [18] L. Zhang, X. Hao, and L. Zhang, "Enhanced energy-storage performances of Bi₂O₃-Li₂O added (1-x)(Na_{0.5}Bi_{0.5})TiO₃-xBaTiO₃ thick films," *Ceramics International*, vol. 40, no. 6, pp. 8847–8851, 2014.
- [19] Q. Xu, H. Liu, Z. Song et al., "A new energy-storage ceramic system based on Bi_{0.5}Na_{0.5}TiO₃ ternary solid solution," *Journal of Materials Science: Materials in Electronics*, vol. 27, no. 1, pp. 322–329, 2016.
- [20] X. Lu, J. Xu, L. Yang et al., "Energy storage properties of (Bi_{0.5}Na_{0.5})_{0.93}Ba_{0.07}TiO₃ lead-free ceramics modified by La and Zr co-doping," *Journal of Materiomics*, vol. 2, no. 1, pp. 87–93, 2016.
- [21] W. P. Cao, W. L. Li, X. F. Dai et al., "Large electrocaloric response and high energy-storage properties over a broad temperature range in lead-free NBT-ST ceramics," *Journal of the European Ceramic Society*, vol. 36, no. 3, pp. 593–600, 2016.
- [22] M. Yao, Y. Pu, H. Zheng, L. Zhang, M. Chen, and Y. Cui, "Improved energy storage density in 0.475BNT-0.525BCTZ with MgO addition," *Ceramics International*, vol. 42, no. 7, pp. 8974–8979, 2016.
- [23] Y. Zhao, X. Hao, and M. Li, "Dielectric properties and energy-storage performance of (Na_{0.5}Bi_{0.5})TiO₃ thick films," *Journal of Alloys and Compounds*, vol. 601, pp. 112–115, 2014.
- [24] N. D. Quan, V. N. Hung, I. W. Kim, and D. D. Dung, "Bipolar electric field induced strain in li substituted lead-free bi_{0.5}(na_{0.82}k_{0.18})_{0.5}ti_{0.95}sn_{0.05}o₃ piezoelectric ceramics," *Journal of Nanoscience and Nanotechnology*, vol. 16, no. 8, pp. 7978–7982, 2016.
- [25] N. D. Quan, T. Q. Toan, V. N. Hung, and M.-D. Nguyen, "ferroelectric and ferromagnetic properties of lead-free Bi_{0.5}(Na_{0.8}K_{0.2})_{0.5}TiO₃ multiferroic films," *Advances in Materials Science and Engineering*, vol. 2019, pp. 1–10, 2019.
- [26] N. D. Quan, V. N. Hung, and D. D. Dung, "Influence of film thickness on ferroelectric properties and leakage current density in lead-free Bi_{0.5}(Na_{0.8}K_{0.2})_{0.5}TiO₃ films," *Materials Research Express*, vol. 4, no. 8, 2017.
- [27] N. D. Quan, V. N. Hung, and D. D. Dung, "Effect of Zr Doping on Structural and Ferroelectric Properties of Lead-Free Bi_{0.5}(Na_{0.8}K_{0.2})_{0.5}TiO₃ Films," *Journal of Electronic Materials (JEM)*, vol. 46, no. 10, pp. 5814–5819, 2017.
- [28] A. Monshi, M. R. Foroughi, and M. R. Monshi, "Modified scherrer equation to estimate more accurately nano-crystallite size using XRD," *World Journal of Nanoscience and Engineering*, vol. 2, no. 3, pp. 154–160, 2012.
- [29] N. D. Quan, V. N. Hung, N. Van Quyet, H. V. Chung, and D. D. Dung, "Band gap modification and ferroelectric properties of Bi_{0.5}(Na,K)_{0.5}TiO₃-based by Li substitution," *AIP Advances*, vol. 4, no. 1, 2014.
- [30] J. Anthoniappen, C. S. Tu, P.-Y. Chen, C.-S. Chen, Y. U. Idzerda, and S.-J. Chiu, "Raman spectra and structural stability in B-site manganese doped (Bi_{0.5}Na_{0.5})_{0.925}Ba_{0.075}TiO₃ relaxor ferroelectric ceramics," *Journal of the European Ceramic Society*, vol. 35, no. 13, pp. 3495–3506, 2015.
- [31] P.-Y. Chen, C.-S. Chen, C.-S. Tu, P.-H. Chen, and J. Anthoniappen, "Effects of texture on microstructure, Raman vibration, and ferroelectric properties in 92.5%(Bi_{0.5}Na_{0.5})TiO₃-7.5%BaTiO₃ ceramics," *Journal of the European Ceramic Society*, vol. 36, no. 7, pp. 1613–1622, 2015.
- [32] N. D. Quan, N. V. Hong, T. Q. Toan, and V. N. Hung, "Enhanced ferroelectric properties and energy storage density in PLZT/BNKT heterolayered thin films prepared by sol-gel method," *The European Physical Journal B*, vol. 91, no. 12, p. 316, 2018.
- [33] C. W. Ahn, S. S. Won, A. Ullah et al., "Large piezoresponse of lead-free Bi_{0.5}(Na_{0.85}K_{0.15})_{0.5}TiO₃ thin film," *Current Applied Physics*, vol. 12, no. 3, pp. 903–907, 2012.
- [34] H. Borkar, V. N. Singh, B. P. Singh, M. Tomar, V. Gupta, and A. Kumar, "Room temperature lead-free relaxor-antiferroelectric electroceramics for energy storage applications," *RSC Advances*, vol. 4, no. 44, pp. 22840–22847, 2014.

Research Article

Improved Electrochemical Performance of $\text{Li}_{1.25}\text{Ni}_{0.2}\text{Co}_{0.333}\text{Fe}_{0.133}\text{Mn}_{0.333}\text{O}_2$ Cathode Material Synthesized by the Polyvinyl Alcohol Auxiliary Sol-Gel Process for Lithium-Ion Batteries

He Wang , Mingning Chang, Yonglei Zheng, Ningning Li, Siheng Chen, Yong Wan, Feng Yuan, Weiquan Shao, and Sheng Xu 

College of Physics, Qingdao University, Qingdao 266071, China

Correspondence should be addressed to Sheng Xu; shengxu@qdu.edu.cn

Received 26 October 2018; Revised 17 November 2018; Accepted 22 November 2018; Published 10 December 2018

Guest Editor: Hong Fang

Copyright © 2018 He Wang et al. This is an open access article distributed under the Creative Commons Attribution License, which permits unrestricted use, distribution, and reproduction in any medium, provided the original work is properly cited.

A lithium-rich manganese-based cathode material, $\text{Li}_{1.25}\text{Ni}_{0.2}\text{Co}_{0.333}\text{Fe}_{0.133}\text{Mn}_{0.333}\text{O}_2$, was prepared using a polyvinyl alcohol (PVA)-auxiliary sol-gel process using MnO_2 as a template. The effect of the PVA content (0.0–15.0 wt%) on the electrochemical properties and morphology of $\text{Li}_{1.25}\text{Ni}_{0.2}\text{Co}_{0.333}\text{Fe}_{0.133}\text{Mn}_{0.333}\text{O}_2$ was investigated. Analysis of $\text{Li}_{1.25}\text{Ni}_{0.2}\text{Co}_{0.333}\text{Fe}_{0.133}\text{Mn}_{0.333}\text{O}_2$ X-ray diffraction patterns by RIETAN-FP program confirmed the layered $\alpha\text{-NaFeO}_2$ structure. The discharge capacity and coulombic efficiency of $\text{Li}_{1.25}\text{Ni}_{0.2}\text{Co}_{0.333}\text{Fe}_{0.133}\text{Mn}_{0.333}\text{O}_2$ in the first cycle were improved with increasing PVA content. In particular, the best material reached a first discharge capacity of 206.0 mAhg^{-1} and best rate capability (74.8 mAhg^{-1} at 5 C). Meanwhile, the highest capacity retention was 87.7% for 50 cycles. Finally, electrochemical impedance spectroscopy shows that as the PVA content increases, the charge-transfer resistance decreases.

1. Introduction

Rapid development of lithium-ion battery technology and the environmental impact of traditional non-renewable energy sources are driving considerable interest in efficient “green” energy storage devices [1]. Currently, the energy storage devices of new energy vehicles and various electronic devices (laptops, cell phones, power tools, bluetooth devices, etc.) usually use lithium ion secondary batteries (LIBs). LiCoO_2 was the first cathode material used for commercial LIBs because of its high operating voltage and ease of preparation [2, 3]. But, the high cost, and toxicity of layered LiCoO_2 limit its use for large-scale high-power applications. Replaceable cathode materials, $\text{Li}_{1.2}\text{Ni}_{0.2}\text{Mn}_{0.6}\text{O}_2$, LiMn_2O_4 , LiFePO_4 , $\text{LiNi}_{1/3}\text{Co}_{1/3}\text{Mn}_{1/3}\text{O}_2$, and $\text{LiNi}_{0.8}\text{Co}_{0.15}\text{Mn}_{0.05}\text{O}_2$, have previously been synthesized [4–8]. Despite its unsatisfactory capacity (120–140 mAhg^{-1}), the layered-structure $\text{LiNi}_x\text{Co}_y\text{Mn}_{1-x-y}\text{O}_2$ is considered a promising cathode material because of its relatively low cost and reduced

toxicity [9, 10]. To address the capacity issue, researchers have launched a series of explorations to identify high-capacity lithium storage cathode materials.

The specific capacity and stability of LIBs can be effectively improved by doping or changing the surface morphology or through surface modification. Mohan et al. synthesized $\text{LiFe}_x\text{Ni}_{1-x}\text{O}_2$ ($0.00 \leq x \leq 0.20$) nanoparticles with a single-layer structure using a sol-gel approach. The particle size was reduced with the substitution of iron, thereby improving the electrochemical properties of the cathode material [11]. The surface-modified layer of the cathode improves the cycle efficiency and thermal stability for high-rate discharge and improves the conductivity of the material surface [12–14].

In this work, we used the well-known sol-gel process to synthesize the target material $\text{Li}_{1.25}\text{Ni}_{0.2}\text{Co}_{0.333}\text{Fe}_{0.133}\text{Mn}_{0.333}\text{O}_2$ by controlling the PVA content (0.0–15.0 wt%). Scanning electron microscopy (SEM), electrochemical tests, and X-ray diffraction (XRD)

were used to investigate the relationship between the PVA doping ratio and specific capacity of the synthesized cathode materials. Pretreatment can significantly improve the rate performance and initial coulomb efficiency and also help to improve cycle stability and suppress voltage attenuation. These properties are expected to improve the capacity utilization and rate capability of this material [15].

2. Experimental Section

2.1. Material Synthesis. Using a method previously reported in the literature, MnCO_3 microspheres were prepared. First, 1.183 g MnSO_4 was dissolved in a mixture of ultrapure water (conductivity of $0.05 \mu\text{Scm}^{-1}$) and alcohol labeled "A." Then, 5.53 g NH_4HCO_3 was dissolved in 490 ml of ultrapure water without alcohol labeled "B." When both A and B are fully dissolved, the two solutions A and B are mixed together to form a suspension. The suspension was stirred constantly at room temperature for 5 h. Then, the white precipitate in the suspension was separated by centrifugation; the precipitate was identified as MnCO_3 . Next, the MnCO_3 was washed with a mixed solution of alcohol and ultrapure water. After cleaning, place MnCO_3 on a drying table and dry it in a 60°C air atmosphere for 6 h.

Second, MnO_2 hollow microspheres were prepared by mixing the precursor MnCO_3 and an aqueous 0.033 M KMnO_4 solution. After removing the MnCO_3 core with 0.03 M HCl , MnO_2 hollow microspheres were obtained after centrifugation. The microspheres were cleaned 3 times with ultrapure water. Next, MnO_2 was dried using a drying oven under an air atmosphere.

Finally, $\text{Li}_{1.25}\text{Ni}_{0.2}\text{Co}_{0.333}\text{Fe}_{0.133}\text{Mn}_{0.333}\text{O}_2$ was prepared using the following PVA-auxiliary sol-gel process. Weigh a certain amount of $\text{LiOH}\cdot\text{H}_2\text{O}$, $\text{Fe}(\text{NO}_3)_3\cdot 9\text{H}_2\text{O}$, $\text{Ni}(\text{NO}_3)_2\cdot 6\text{H}_2\text{O}$, $\text{Co}(\text{NO}_3)_2\cdot 6\text{H}_2\text{O}$, the MnO_2 microspheres were dissolved in 60 ml of ultrapure water, and the lithium/metal (Ni, Mn, Fe) molar ratio is 1.25. Since lithium is depleted under high temperature conditions, it is necessary to add an excessive amount of lithium. In order to ensure sufficient reaction of raw materials, PVA and citric acid were added successively in different time. The mass fractions of PVA were $x = 0.0, 2.5, 5.0, 7.5, 9.0, 10.0, 11.0, 12.5, \text{ and } 15.0$ wt%. The molar ratio of citric acid to total metal ions was 1:1 [16]. The mixture was then stirred at 80°C until a viscous gel was obtained [17]. The treatment of the precursor was divided into two steps, first drying at 120°C for 12 h and then heating to 450°C for 6 h in air.

The final products were obtained by finely grinding the gel followed by heat treatment at 950°C under a non-rare gas atmosphere for 12 h.

3. Results and Discussion

3.1. Sample Characterization. We first investigated the structural features of the MnO_2 hollow microsphere samples and PVA-auxiliary lithium-rich manganese-based cathode samples using SEM. The spherical shell structure and broken hollow microspheres of the MnO_2 are shown in Figures

1(a) and 1(b), respectively. Both of their diameters were approximately $1 - 2 \mu\text{m}$. All of the samples exhibited a shell structure that was gradually destroyed with increasing x while the layered structure was aggregated together, which greatly increased the contact surface area in the scanned area. The tendency toward aggregation decreased with increasing x in Figures 1(c)–1(i). For $x = 10.0$ wt%, the sample has the smallest particle size and the most uniform distribution. It is well known that electrochemical lithium insertion/extraction is much easier in small particles, because of the reduction of diffusion pathways for Li^+ ions, which also enables faster electronic transport through the size effect [19].

4. Characterization

The X-ray diffraction (Rigaku SmArtlab-3KW) patterns were collected on a D8 Advance instrument with $\text{Cu K}\alpha$ radiation operated at 40 KV, 40 mA and scanning step 2 degrees per minute at room temperature from 10° to 80° . The XRD results were analyzed using the RIETAN-FP program. SEM (JEOL JSM-6390) was usually applied to analyze the morphology of the resulting materials.

Electrochemical Measurements. The electrochemical measurements of terrestrial CR2025 batteries were performed at room temperature using CR2025 coin cells. The active substances, acetylene black and poly (vinylidene fluoride) were dissolved in N-methyl-2-pyrrolidone (NMP) at a ratio of 8:1:1, and then the cathode compounds were evenly coated on the aluminium foil by a smearing machine. Firstly, the smear was dried in 50°C air for 6 hours, and then dried in 120°C vacuum for 12 hours. The coin cells were assembled in a glove box ($\text{H}_2\text{O} < 1\text{ppm}$, $\text{O}_2 < 1\text{ppm}$) using Li metal foil as the counter electrodes and 1 M LiPF_6 in a 1:1 v/v mixture of ethylene carbonate and diethyl carbonate as the electrolyte. The assembled battery was subjected to a charge and discharge cycle test at different magnifications, and the voltage range was controlled within 2.5 to 4.5 V. The electrochemical impedance spectroscopy spectra were obtained in the frequency range of 10^{-1} Hz to 10^5 Hz using a PARSTAT 2273 electrochemical work station [18].

Figure 2 presents a prototypical example of the XRD powder pattern of $\text{Li}_{1.25}\text{Ni}_{0.2}\text{Co}_{0.333}\text{Fe}_{0.133}\text{Mn}_{0.333}\text{O}_2$ ($x = 10.0$ wt%). The pattern was obtained using the RIETAN-FP program. The powder pattern reproduces well the typical features of the $\alpha\text{-NaFeO}_2$ structure and can be indexed as the R-3m space group, as indicated by the solid curve. The splitting of the (006), (012) and (018), (110) reflections suggests the formation of a highly ordered hexagonal layered structure [20]. We further performed a similar Rietveld analysis for other compounds, and software analysis results are shown in Table 1. The final refinements were satisfactory, with R_{WP} and R_1 (reliable factor based on the integrated intensity) being sufficiently small. The lattice parameters of all the samples differed slightly. Figure 3 shows the regularity of (a) lattice parameters a and c and (b) lattice volume V with the change of PVA mass fraction. The lattice parameters had minimum values at $x = 10.0$ wt%, indicating the stability of the lattice of these samples. Compared with $x = 0.0$ wt%, the lattice

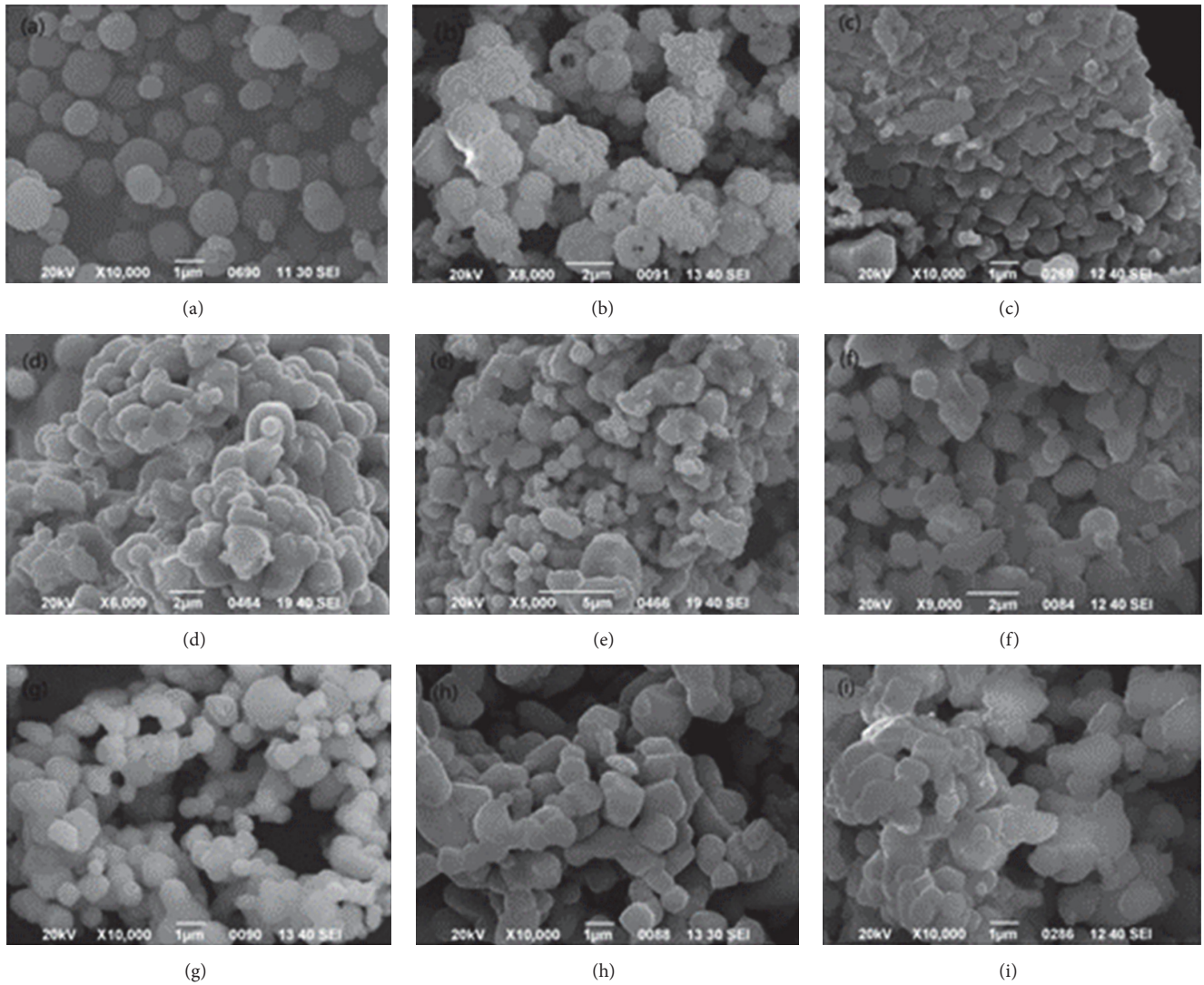


FIGURE 1: SEM images of (a) a complete spherical shell, (b) broken MnO₂ hollow microspheres, and Li_{1.25}Ni_{0.2}Co_{0.333}Fe_{0.133}Mn_{0.333}O₂ samples for (c) $x = 0.0$ wt%, (d) $x = 2.5$ wt%, (e) $x = 5.0$ wt%, (f) $x = 7.5$ wt%, (g) $x = 10.0$ wt%, (h) $x = 12.5$ wt%, and (i) $x = 15.0$ wt%.

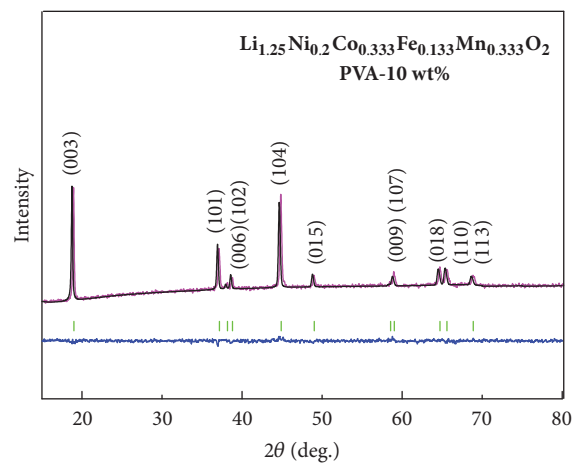
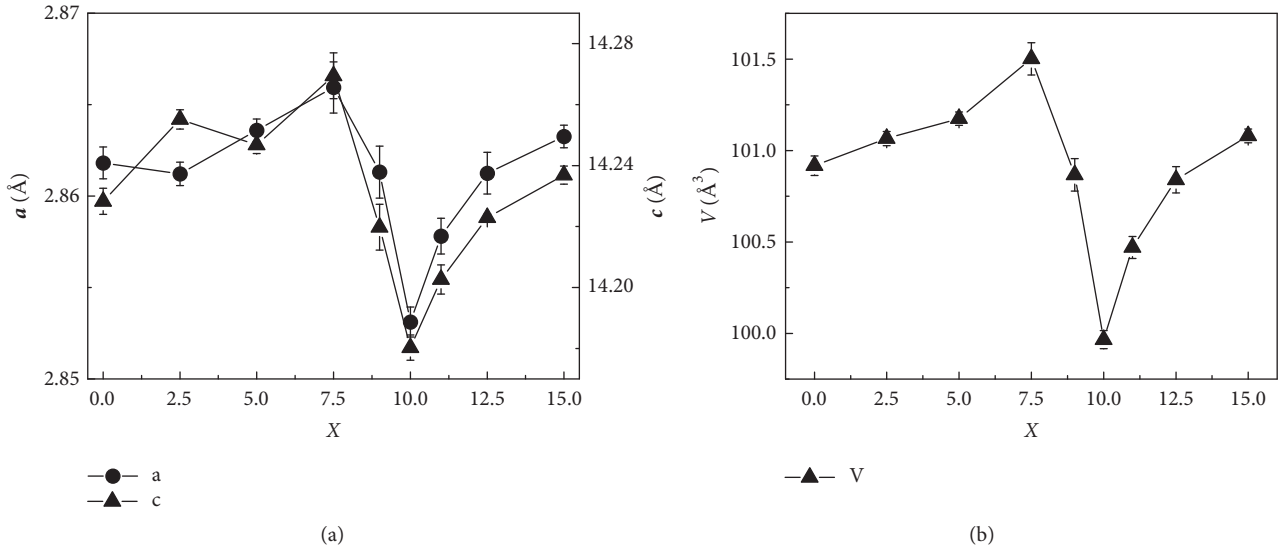


FIGURE 2: Refined XRD pattern of Li_{1.25}Ni_{0.2}Co_{0.333}Fe_{0.133}Mn_{0.333}O₂ ($x = 10.0$ wt%). The black crosses represent the measured points, and the pink curve is the fitted line. The green marks indicate the peak positions, and the blue line is the error curve.

TABLE I: Structural parameters of $\text{Li}_{1.25}\text{Ni}_{0.2}\text{Co}_{0.333}\text{Fe}_{0.133}\text{Mn}_{0.333}\text{O}_2$ are refined by the Rietan-FP.

PVA content	a (Å)	c (Å)	V (Å ³)	R_{WP} (%)	R_{I} (%)	S
0.0%	2.86(1)	14.22(8)	100.9(1)	6.592	5.196	1.0932
2.5%	2.86(1)	14.25(5)	101.0(6)	6.707	5.332	1.0903
5.0%	2.86(3)	14.24(6)	101.1(7)	5.928	5.726	1.0021
7.5%	2.86(5)	14.26(9)	101.5(0)	6.528	5.160	1.0874
9.0%	2.86(1)	14.21(9)	100.8(6)	6.374	5.082	1.0570
10.0%	2.85(3)	14.18(0)	99.9(6)	6.764	5.285	1.1181
11.0%	2.85(7)	14.20(2)	100.4(6)	6.497	5.168	1.0187
12.5%	2.86(1)	14.22(2)	100.8(3)	6.615	5.784	1.2039
15.0%	2.86(3)	14.23(6)	101.0(8)	6.401	5.087	1.0514

FIGURE 3: Variation of (a) lattice parameters a and c and (b) lattice volume V of the pristine sample and PVA-auxiliary samples, where x is the PVA content.

volume of $\text{Li}_{1.25}\text{Ni}_{0.2}\text{Co}_{0.333}\text{Fe}_{0.133}\text{Mn}_{0.333}\text{O}_2$ ($x = 10.0$ wt%) was reduced by 0.94%.

The electrochemical performance of the original and PVA-auxiliary lithium-rich manganese-based cathode samples was investigated at 2.5 and 4.5 V at different rates using lithium metal as the anode. The charge curves for various cycles at a rate of 0.1 C are presented in Figure 4(a). The smooth curves indicate that the electrode material had a stable structure within the tested voltage range [21]. For the pristine sample, the first discharge capacity was 141.5 mAhg^{-1} and after 50 cycles, it faded to 122 mAhg^{-1} , and the capacity loss was 16%.

For the PVA-auxiliary lithium-rich manganese-based sample ($x = 10.0$ wt%), the first discharge capacity was 206.0 mAhg^{-1} and after 50 cycles, it faded to 180.7 mAhg^{-1} , and the capacity loss was only 14%. It can thus be concluded that the use of a moderate PVA-auxiliary sol-gel process can enhance the specific capacity of the sample. This result occurs because the surface area is affected by the PVA content, and the increased surface area provides favorable conditions for the lithium ion insertion/extraction process. As the number of cycles increases, the discharge capacity of all samples

decreases slowly, most likely due to structural deformation and/or side reactions during charge and discharge.

Figure 4(b) shows the cycle performances of all the materials under different rate. Classically, at high current rates, the specific volume drops, which may be due to an increase in electrode polarization during the cycle observed by previous researchers.

Under the various rates, specific capacities of PVA-auxiliary sample ($x = 10.0$ wt%) are always higher than other samples. Especially in 2 C rate, compared with PVA-auxiliary sample ($x = 0.0$ wt%), PVA-auxiliary sample ($x = 10.0$ wt%) has 2.5-fold superior rate capabilities. More importantly, when the magnification returns to 0.1 C, the capacity can be closest to the initial value. This suggests that the cathode material ($x = 10.0$ wt%) has an excellent reversibility. The results in Figures 4(a) and 4(b) indicate that the optimal electrochemical performance of coin cells was achieved for the PVA-auxiliary sample ($x = 10.0$ wt%).

To determine the rate capability of the sample, the battery was cycled between 2.5 and 4.5 V at different current rates of 0.1 C. The results are shown in Figure 5. The rate capability of the PVA-auxiliary sample is significantly higher

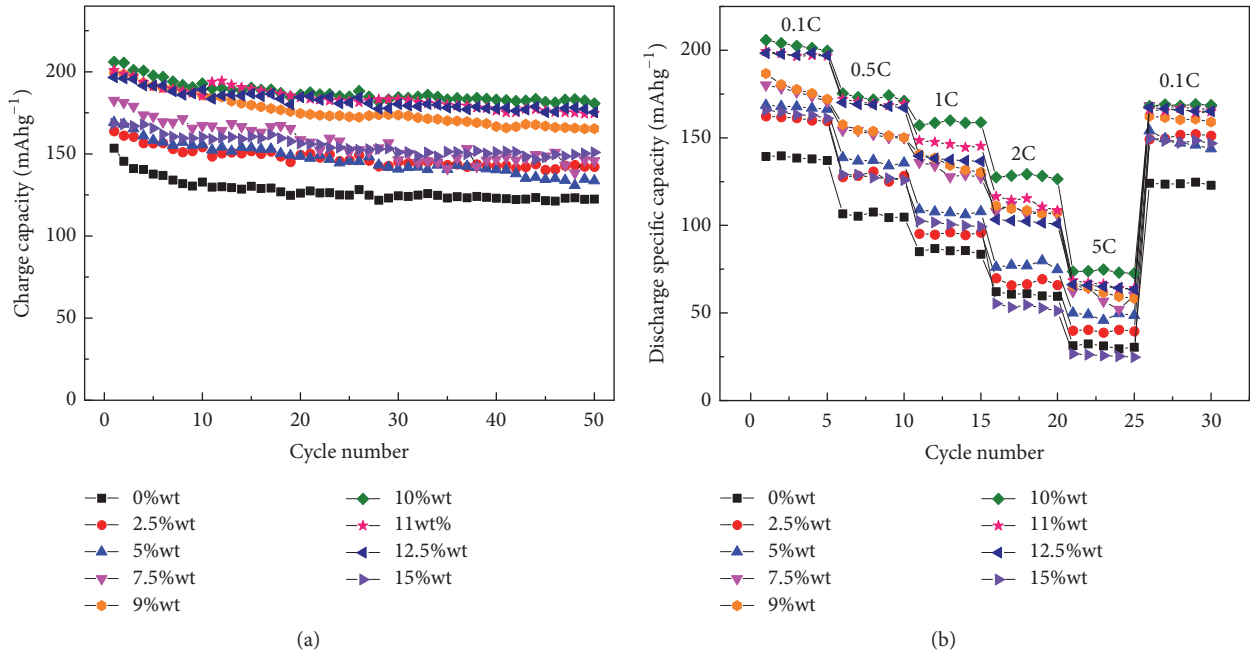


FIGURE 4: (a) Charge curves of pristine and PVA-auxiliary lithium-rich manganese-based cathode materials at 0.1 C; (b) rate capabilities of the $x = 0.0$ – 15.0 wt% cathodes.

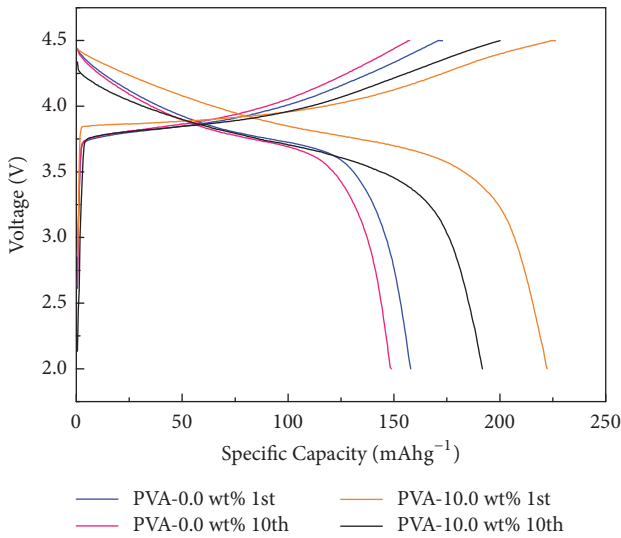


FIGURE 5: Charge/discharge curves of $\text{Li}_{1.25}\text{Ni}_{0.2}\text{Co}_{0.333}\text{Fe}_{0.133}\text{Mn}_{0.333}\text{O}_2$ ($x = 0.0$ and 10.0 wt%) cathodes at the rate of 0.1 C.

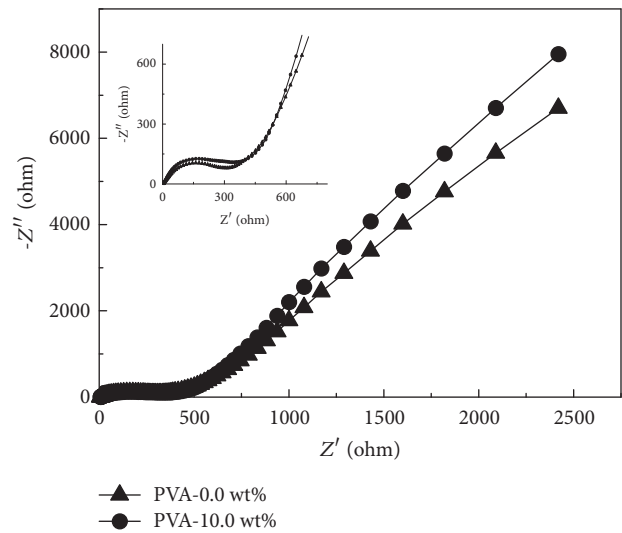


FIGURE 6: Cathodic EIS spectra of $\text{Li}_{1.25}\text{Ni}_{0.2}\text{Co}_{0.333}\text{Fe}_{0.133}\text{Mn}_{0.333}\text{O}_2$ ($x = 0.0$ and 10.0 wt%) materials. The inset shows the cathodic EIS spectra in the low- z' region.

than the original sample. Compared with other samples, the PVA-auxiliary sample ($x = 10.0$ wt%) has an excellent rate performance, because the PVA-auxiliary method reduces the charge-transfer resistance and enhances the reaction kinetics [22].

To study the reaction kinetics of the electrode materials, as shown in Figure 6, the EIS is tested with three electrode units in the frequency range of 10^{-1} to 10^5 Hz. In this region, a slanted line and semicircle were observed. The Z' -intercept

between the composition of the battery and the electrolytic resistance in the high frequency region corresponds to the ohmic resistance (R_e).

The middle-frequency semicircle is associated with the charge-transfer resistance (R_{ct}) at the interface of the electrode and electrolyte [23]. The lithium ion scattering relationship in the cathode material is reflected on the oblique line of the low velocity region of the Warburg impedance (Z_w). The charge-transfer resistance of the $x = 10.0$ wt% sample was

300 Ω , which is smaller than that of the pristine sample (400 Ω). One possible explanation for this result is that the ion transport of the PVA-auxiliary sample is relatively faster. The reduction in charge transfer resistance clearly demonstrates the importance of electron conductivity and Li^+ diffusion when cycling at high current rates, which is closely related to rate capability and charge and discharge cycle data.

5. Conclusions

In this study, a lithium-rich manganese-based cathode material, $\text{Li}_{1.25}\text{Ni}_{0.2}\text{Co}_{0.333}\text{Fe}_{0.133}\text{Mn}_{0.333}\text{O}_2$, was synthesized using a PVA-auxiliary sol-gel process, and the effects of the PVA content on the crystal structure and morphology were investigated using XRD and SEM analyses. Compared with the pristine material, the PVA-auxiliary material ($x = 10.0$ wt%) after the 50 cycles of 0.1 C, the capacity holding rate is 27.7%, and the capacity at 5 C is 74.8 mAhg^{-1} . The improved performance of the PVA-auxiliary sample resulted from the effective reduction of the charge-transfer resistance and enhancement of the reaction kinetics. Because of the role of PVA, the rate capability and circulation of $\text{Li}_{1.25}\text{Ni}_{0.2}\text{Co}_{0.333}\text{Fe}_{0.133}\text{Mn}_{0.333}\text{O}_2$ are improved.

Data Availability

The parameters and data used to support the findings of this study are included within the article.

Conflicts of Interest

The authors declare that they have no conflicts of interest.

Acknowledgments

This work is supported by the National Natural Science Foundation of China (NSFC, 11144007) and National Natural Science Foundation of Shandong Province (ZR2016AM27).

References

- [1] P. L. Taberna, S. Mitra, P. Poizot, P. Simon, and J. M. Tarascon, "High rate capabilities Fe_3O_4 -based Cu nano-architected electrodes for lithium-ion battery applications," *Nature Materials*, vol. 5, no. 7, pp. 567–573, 2006.
- [2] T. Ohzuku, A. Ueda, M. Nagayama, Y. Iwakoshi, and H. Komori, "Comparative study of LiCoO_2 , $\text{LiNi}_{1/2}\text{Co}_{1/2}\text{O}_2$ and LiNiO_2 for 4 volt secondary lithium cells," *Electrochimica Acta*, vol. 38, no. 9, pp. 1159–1167, 1993.
- [3] Y. Gu, D. Chen, and X. Jiao, "Synthesis and electrochemical properties of nanostructured LiCoO_2 fibers as cathode materials for lithium-ion batteries," *The Journal of Physical Chemistry B*, vol. 109, no. 38, pp. 17901–17906, 2005.
- [4] J. Hong, D.-H. Seo, S.-W. Kim, H. Gwon, S.-T. Oh, and K. Kang, "Structural evolution of layered $\text{Li}_{1.2}\text{Ni}_{0.2}\text{Mn}_{0.6}\text{O}_2$ upon electrochemical cycling in a Li rechargeable battery," *Journal of Materials Chemistry*, vol. 20, no. 45, pp. 10179–10186, 2010.
- [5] J. M. Tarascon, E. Wang, F. K. Shokoohi, W. R. Mckinnon, and S. Colson, "ChemInform Abstract: The Spinel Phase of LiMn_2O_4 as a Cathode in Secondary Lithium Cells," *ChemInform*, vol. 22, no. 49, pp. no–no, 1991.
- [6] A. Yamada, S. C. Chung, and K. Hinokuma, "ChemInform Abstract: Optimized LiFePO_4 for Lithium Battery Cathodes," *ChemInform*, vol. 32, no. 29, pp. no–no, 2001.
- [7] Y. M. Sun, X. L. Hu, W. Luo, and Y. H. Huang, "Self-assembled mesoporous CoO nanodisks as a long-life anode material for lithium-ion batteries," *Journal of Materials Chemistry*, vol. 22, no. 27, pp. 13826–13831, 2012.
- [8] K. Zhong, X. Xia, B. Zhang, H. Li, Z. Wang, and L. Chen, "MnO powder as anode active materials for lithium ion batteries," *Journal of Power Sources*, vol. 195, no. 10, pp. 3300–3308, 2010.
- [9] C. Nithya, R. Thirunakaran, A. Sivashanmugam, G. V. M. Kiruthika, and S. Gopukumar, "High-capacity sol-gel synthesis of $\text{LiNixCoyMn}_{1-x-y}\text{O}_2$ ($0 \leq x, y \leq 0.5$) cathode material for use in lithium rechargeable batteries," *The Journal of Physical Chemistry C*, vol. 113, no. 41, pp. 17936–17944, 2009.
- [10] D. Wang, X. Li, Z. Wang et al., "Role of zirconium dopant on the structure and high voltage electrochemical performances of $\text{LiNi}_{0.5}\text{Co}_{0.2}\text{Mn}_{0.3}\text{O}_2$ cathode materials for lithium ion batteries," *Electrochimica Acta*, vol. 188, pp. 48–56, 2016.
- [11] Q. Chang, H. Zhang, X. Wang et al., "Structure and electrochemical performance of hollow microspheres of $\text{LiFexNi}_{1/3-x}\text{Co}_{1/3}\text{Mn}_{1/3}\text{O}_2$ ($0.000 \leq x \leq 0.267$) as cathodes for lithium-ion batteries," *RSC Advances*, vol. 5, no. 69, pp. 56274–56278, 2015.
- [12] T. Rajh, O. I. Mičić, and A. J. Nozik, "Synthesis and characterization of surface-modified colloidal CdTe quantum dots," *The Journal of Physical Chemistry C*, vol. 97, no. 46, pp. 11999–12003, 1993.
- [13] S. Huang, Z. Wen, X. Yang, Z. Gu, and X. Xu, "Improvement of the high-rate discharge properties of LiCoO_2 with the Ag additives," *Journal of Power Sources*, vol. 148, no. 1–2, pp. 72–77, 2005.
- [14] A. Diener, B. Nebe, F. Lüthen et al., "Control of focal adhesion dynamics by material surface characteristics," *Biomaterials*, vol. 26, no. 4, pp. 383–392, 2005.
- [15] W. He, J. Qian, Y. Cao, X. Ai, and H. Yang, "Improved electrochemical performances of nanocrystalline $\text{Li}[\text{Li}_{0.2}\text{Mn}_{0.54}\text{Ni}_{0.13}\text{Co}_{0.13}]\text{O}_2$ cathode material for Li-ion batteries," *RSC Advances*, vol. 2, no. 8, pp. 3423–3429, 2012.
- [16] T. Luo, X. Liu, X. Meng, H. Wu, S. Wang, and Z. Zhan, "In situ formation of $\text{LaNi}_{0.6}\text{Fe}_{0.4}\text{O}_{3-\delta}$ -carbon nanotube hybrids as anodes for direct-methane solid oxide fuel cells," *Journal of Power Sources*, vol. 299, pp. 472–479, 2015.
- [17] Y. Ruan, K. Wang, S. Song, J. Liu, and X. Han, "Improved structural stability and electrochemical performance of $\text{Na}_3\text{V}_2(\text{PO}_4)_3$ cathode material by Cr doping," *Ionics*, vol. 23, no. 5, pp. 1097–1105, 2017.
- [18] N. Cimpoeșu, L. C. Trincă, G. Dascălu, S. Stanciu, S. O. Gurlui, and D. Mareci, "Electrochemical Characterization of a New Biodegradable FeMnSi Alloy Coated with Hydroxyapatite-Zirconia by PLD Technique," *Journal of Chemistry*, vol. 2016, Article ID 9520972, 9 pages, 2016.
- [19] Y. Yin, S. Xin, and Y. Guo, "Nanoparticles Engineering for Lithium-Ion Batteries," *Particle & Particle Systems Characterization*, vol. 30, no. 9, pp. 737–753, 2013.
- [20] W. Dong, Y. Sun, W. L. Chul et al., "Controllable and repeatable synthesis of thermally stable anatase nanocrystal-silica composites with highly ordered hexagonal mesostructures," *Journal of*

the American Chemical Society, vol. 129, no. 45, pp. 13894–13904, 2007.

- [21] H. Kokubo, T. Honda, S. Imaizumi, K. Dokko, and M. Watanabe, “Effects of carbon electrode materials on performance of ionic polymer actuators having electric double-layer capacitor structure,” *International Journal of Electrochemistry*, vol. 81, no. 10, pp. 849–852, 2013.
- [22] Y. Shi and M. L. Falk, “Strain Localization and Percolation of Stable Structure in Amorphous Solids,” *Physical Review Letters*, vol. 95, no. 9, 2005.
- [23] Y. Zhu and C. Wang, “Strain accommodation and potential hysteresis of LiFePO₄ cathodes during lithium ion insertion/extraction,” *Journal of Power Sources*, vol. 196, no. 3, pp. 1442–1448, 2011.

Research Article

Performance Investigation of a Silicon Photovoltaic Module under the Influence of a Magnetic Field

Dioari Ulrich Combari,¹ Emmanuel Wendsongré Ramde ,² Idrissa Sourabie,¹ Martial Zoungrana,¹ Issa Zerbo ,¹ and Dieudonné Joseph Bathiebo¹

¹Laboratory of Thermal and Renewable Energy, Department of Physics, Unité de Formation et de Recherche en Sciences Exactes et Appliquées, Université Ouaga I Prof. Joseph KI-ZERBO, Ouagadougou, Burkina Faso

²Department of Mechanical Engineering and The Brew-Hammond Energy Centre, Kwame Nkrumah University of Science and Technology, Kumasi, Ghana

Correspondence should be addressed to Emmanuel Wendsongré Ramde; eramde@gmail.com

Received 6 September 2018; Accepted 1 November 2018; Published 18 November 2018

Guest Editor: Hong Fang

Copyright © 2018 Dioari Ulrich Combari et al. This is an open access article distributed under the Creative Commons Attribution License, which permits unrestricted use, distribution, and reproduction in any medium, provided the original work is properly cited.

Aside from the terrestrial magnetic field that is generated from the earth core, power transmission, and distribution lines, transformers and other equipment do produce a certain amount of magnetic field that could interfere with the performance of photovoltaic modules. This study conducted an experiment and investigated the performance of a silicon photovoltaic module subjected to a magnetic field. The current-voltage and power-voltage characteristics were plotted in the same axis system and allowed us to find, as a function of the magnetic field, the electrical parameters of the photovoltaic module such as maximum electric power, fill factor, conversion efficiency, and charge resistance at the maximum power point. These electrical parameters were then used to calculate the series and shunt resistances of the equivalent circuit of the photovoltaic module. The results have shown that the efficiency of a solar module is affected by the presence of magnetic fields. However, the magnitude of ambient magnetic field generated by power transmissions lines and other equipment is extremely low (in the order of 10^{-2} mT or less) as compared to the values of the magnetic field used in this study. That made it difficult to conclude as to the impact of such field on solar photovoltaic installations.

1. Introduction

The performance of a photovoltaic module (PV module) depends on climatic and seasonal parameters but may also depend on the presence of some external factors such as electric field, magnetic field, and electromagnetic field.

Various researchers have used theoretical and experimental methods to investigate the effect of climatic and seasonal conditions on photovoltaic modules and arrived at different results.

Emetere et al. [1] examined, through experimental tests, the effects of solar radiation irregularities due to climate change on the electrical performance of photovoltaic modules. Koffi et al. [2] experimentally investigated the seasonal variation of the operating temperature of silicon solar modules under tropical atmospheric conditions, including high

turbidity (Harmattan dust particles). Their results confirmed that monocrystalline modules have lower temperature coefficient than polycrystalline and amorphous solar modules. Dia et al. [3] studied the degradation of photovoltaic modules under tropical weather conditions. The degradation of the photovoltaic modules, due to exposure to UV radiation, temperature, humidity, and aerosols in a Sahelian environment was investigated. The study showed that the degradation of the photovoltaic modules is more affected by temperature as well as solar irradiation. In the same vein, Kazem et al. [4] investigated the effect of dust on the performance of photovoltaic modules. The authors conducted an experiment to identify the effect of deposition of different pollutants (red soil, ash, sand, calcium carbonate, and silica) on the voltage and power output of photovoltaic modules. The results showed a drop of the voltage and the power output



FIGURE 1: Photography of experimental setup.

of the photovoltaic module when dust particles are deposited on the photovoltaic module. This drop was noted to be strongly dependent on the type of pollutant and on the level of deposition. The study also noted that ash pollutant affects the most the voltage of photovoltaic modules as compared to the other pollutants.

Other researchers used experimental methods to study the effect of magnetic field on the performances of solar cells. Betser et al. [5] used an experimental method to measure the mobility of minority carriers in the base of InP/GaInAs heterojunction bipolar transistor under constant magnetic field. The magnetic field was applied perpendicular to the direction of the current flow. The standard magnetotransport theory was used to establish a relation between the base current with no magnetic field, the change in the base current induced by the magnetic field, the mobility of the electrons, and the intensity of the applied magnetic field. The authors obtained the electron mobility in the base of an NPN InP/GaInAs HBT by measuring the base current as a function of the intensity of applied magnetic field. The result was in agreement with the value of the mobility measured by the zero field time of flight technique. Vardanyan et al. [6] proposed a method for measuring all recombination parameters (diffusion length, diffusion coefficient, carriers mobility, back surface recombination velocity) in the base region of bifacial solar cell illuminated by its rear side and under constant magnetic field applied parallel to the surface of the p-n junction. The bifacial solar cell was illuminated with a monochromatic light and the expression of electron photocurrent and the associated parameters were obtained by solving the continuity equation. By measuring the short circuit photocurrents for two different wavelengths without magnetic field and under applied magnetic field, the authors obtained the recombination parameters of the solar cell. Erel [7] conducted an experiment and studied the effect of electric and magnetic fields on the response of three different types of solar cells (monocrystal, polycrystal, and amorphous Si solar cells). The cells were first illuminated with LEDs of different color and secondly by a lamp, with tungsten filament, of different flux intensity. Erel concluded that the short circuit current and the open circuit voltage decreased in the presence of magnetic the field from red LED to the blue one. For an increasing light flux intensity produced by the lamp with tungsten filament, the short circuit current and the open circuit voltage decreased in the presence of the magnetic field.

In a previous work [8] we have shown, by simulation, that within the limits of the study, magnetic fields affect the performance of a photovoltaic module made up of ideal solar cells.

The aim of this work was to investigate potential negative impact of magnetic fields on the performance of a commercial silicon photovoltaic module. From experimental measurements of I-V and P-V characteristics of the photovoltaic module, we found the maximum electric power, the fill factor, the conversion efficiency, and the charge resistance at the maximum power point. Then, we calculated the series and shunt resistances of the equivalent circuit of the photovoltaic module.

2. Materials and Methods

2.1. Experimental Setup. The material used for the experimental study (Figures 1 and 2) was as follows:

(i) a monocrystalline silicon photovoltaic module whose characteristics are as follows:

- (a) maximum electric power $P_{\max} = 5W$
- (b) voltage at maximum power point: $V_{\max} = 17.50V$
- (c) current at maximum power point: $I_{\max} = 0.29A$
- (d) open circuit voltage: $V_{OC} = 22.05V$
- (e) short circuit current: $I_{SC} = 0.32A$
- (f) surface of the photovoltaic module: $S_{\text{mod}} = 270 \text{ cm}^2$

(ii) an inductance in U form used for the creation of the magnetic field

(iii) a device used for the measurement of the intensity of the magnetic field, made up of a probe and a millivoltmeter

(iv) two DC generators: 31.5 V - 2.5 A

(v) three rheostats: 3300 Ω -0.25A, 1000 Ω -0.5A, and 100 Ω - 1.5A

(vi) a magnetoelectric amperemeter and a magnetoelectric voltmeter

(vii) a ferromagnetic voltmeter and a ferromagnetic amperemeter

(viii) a ferromagnetic millivoltmeter

(ix) an autotransformer: 400 V-13A

(x) a pyranometer, Standard ST-1307 to measure the solar irradiance

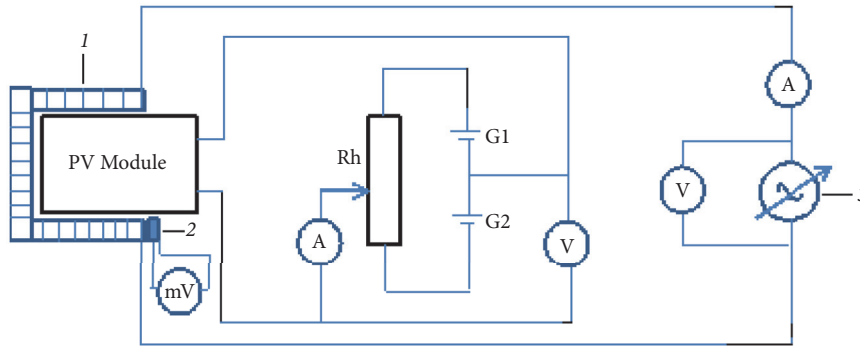


FIGURE 2: Experimental setup ((1) inductance in U form; (2) probe; (3) autotransformer.).

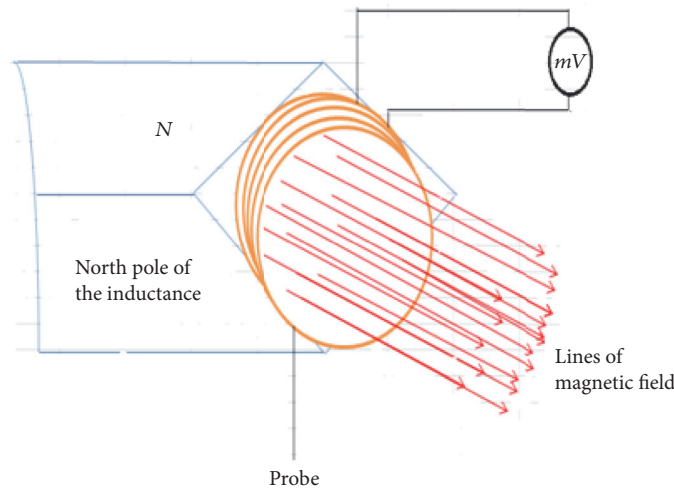


FIGURE 3: Device (probe) used for the measurement of the magnetic field.

(xi) a Midi Logger GL 200A to measure the temperature T_1 at the front side of the photovoltaic module, the temperature T_2 at the back side of the photovoltaic module, and the ambient temperature T_3

The autotransformer was used to vary the intensity of the current through the U inductance located at 1 cm from the photovoltaic module, by varying its supply voltage. Consequently, the intensity of the created magnetic field varied. The variation of the current supplied by the photovoltaic module was obtained by the variation of the charge resistance Rh.

It is worth noting that the test was conducted in Ouagadougou located at latitude 12.37°N and longitude 1.52°W .

2.2. Magnetic Field Measurement

2.2.1. Device for the Magnetic Field Measurement. The probe used for the measurement of the magnetic field intensity was a coil; this is illustrated by Figure 3. This coil is a toroidal inductor whose diameter is 450 mm and it is made up of 10 loops. The loops are made with copper of 1 mm^2 of section and protected with an insulator. This probe is positioned

at the section of the magnetic circuit of the inductance that creates the magnetic field. The probe is connected to a ferromagnetic millivoltmeter of class 0.5 (Figure 3).

The method used for the measurement of the magnetic field is the principle of the electromagnetic induction.

2.2.2. Determination of the Teslametric Constant. We suppose that the inductance is not saturated; therefore, it generates a sinusoidal magnetic field whose instantaneous value is given by

$$b(t) = B_m \sin(\omega t) \tag{1}$$

B_m is the amplitude of the magnetic field.

The sinusoidal magnetic field generated by the inductance in U form produces a magnetic flux through the coil of the probe. The instantaneous value of this magnetic flux is given by

$$\phi(t) = NSB_m \sin(\omega t) \tag{2}$$

N is the number of loops of the probe and S is the section of the coil.

TABLE 1: Effective values of the magnetic field.

E (mV)	0	49.93	74.89	149.76	349.63	499.25	748.88
ΔE (mV)	0	1.00	1.00	2.00	2.00	0.50	5.50
B (mT)	0	10	15	30	50	100	150
ΔB (mT)	0	0.20	0.20	0.40	0.40	0.10	1.10

An electromotive force is induced in the coil and its effective value is measured with a millivoltmeter. The instantaneous value of the electromotive force induced in the coil is expressed in the following:

$$e(t) = -\frac{d\phi(t)}{dt} = \omega NSB_m \cos(\omega t + \pi) \quad (3)$$

$$e(t) = \omega NSB\sqrt{2} \cos(\omega t + \pi) \quad (4)$$

The expression of the amplitude of the electromotive force is given by

$$E_m = \omega NSB\sqrt{2} \quad (5)$$

Thus, we deduced the relation between the effective value of the magnetic field and the one of the electromotive force given by

$$B = \frac{1}{\omega NS} E = K_T E \quad (6)$$

where B is effective value of the magnetic field, E is effective value of the electromotive force induced in the coil, and K_T is teslametric constant.

In this study, the value of the teslametric constant is $K_T = 0.2003 (TV^{-1})$.

Knowing the value of the teslametric constant, we deduced the effective value of the magnetic field from the measured effective value of the electromotive force.

The effective values of the magnetic field are given in Table 1.

Figure 4 is a plot of the effective value of the magnetic field as against the effective value of the electromotive force.

We used Figure 4, which is a straight line passing by the origin of the axis, for the determination of the effective value of the magnetic field.

3. Results and Discussion

3.1. Experimental I-V Characteristics. The experimental setup of Figure 1 allowed us to measure the intensity provided by the photovoltaic module to a variable charge resistance and its voltage for four constant values of magnetic field intensity. The results of the measurement are presented in Table 2.

The results in Table 2 show that, from short circuit to open circuit, the intensity of the electric current decreases when the intensity of the applied magnetic field increases.

We noticed that the ambient temperatures T_3 are higher than the temperatures T_1 measured at the front side of the photovoltaic module. The temperatures T_1 are also higher than the temperatures T_2 measured at the back side of the photovoltaic module.

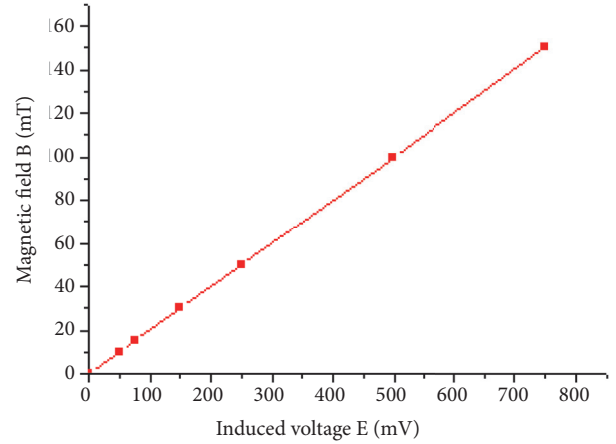


FIGURE 4: Effective value of magnetic field versus effective value of electromotive force.

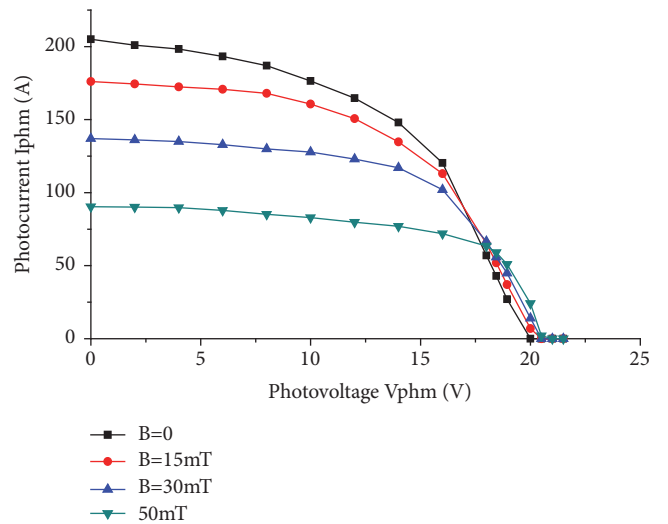


FIGURE 5: Experimental I-V characteristics at different intensity of the magnetic field.

Figure 5 is a plot of the experimental I-V curves of the photovoltaic module for different values of the magnetic field.

The experimental I-V curves have the same shape as the theoretical I-V curves obtained through modelling in a previous study by Combari et al. [8]. As the intensity of the magnetic field in milliTesla (mT) was varied from 0 to 15, 0 to 30, and 0 to 50, the short circuit current decreased by 14%, 22%, and 34%, respectively, while the open circuit voltage slightly increased by 5%, 5%, and 8%, respectively.

TABLE 2: Values of current and voltage of the photovoltaic module against the intensity of the magnetic field and for a solar irradiance of 600 W/m².

V_{mod} (V)	B (mT)				Temperature at front side T_1 (°C)	Temperature at back side T_2 (°C)	Ambient temperature T_3 (°C)
	0	15	30	50			
0	205	176.12	137	90.4	38.9	37.7	52.6
2	201	174.49	136.2	90.16	43.9	41.3	54.5
4	198.35	172.38	135	89.7	43.7	41.5	53.5
6	193.25	170.79	132.85	87.8	42	41.6	54.7
8	187	168	130	85.2	43	41.4	54.6
10	176.42	160.65	127.75	82.9	43.6	41.2	53.6
12	164.69	150.62	123	79.7	44.2	41	52.8
14	148.03	134.79	117	77	44.3	41.2	52.9
16	120.29	113	102	71.88	44	41.3	52.8
18	57	65.05	66.67	63.44	43.4	41	52.7
18.45	42.96	52	55.83	59	43.8	41.4	54
18.94	27	37	44.88	51	43.8	41	55.5
20	0	7	14	24.2	41.6	40.3	54.4
20.91	0	0	0	2	41.4	40.8	55
21.5	0	0	0	0	42.1	41.4	54.6

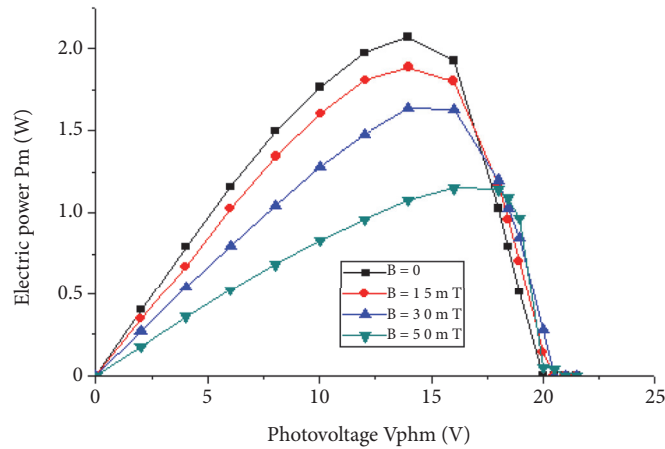


FIGURE 6: Experimental power versus voltage at different intensity of the magnetic field.

3.2. Experimental Power-Voltage Characteristics. The experimental values in Table 2 allowed us to compute the electric power that the photovoltaic module can provide to an external charge. The results are in Table 3.

The results show that the electric power decreases with an increase of the magnetic field, except for points close to the open circuit voltage. The decrease of the electric power means that, as the magnetic field increases, the decrease in current is much more important than the increase in voltage.

Figure 6 is a plot of the electric power versus the voltage at different intensity of the magnetic field.

Figure 6 is also in accordance with the theoretical power-voltage characteristics which were obtained through modelling in a previous study by Combari et al. [8]. It can be observed that, as the intensity of the magnetic field increases,

the electric power at the maximum power point decreases. Also, as intensity of the magnetic field increases, the curves get less steep and shift to the right towards the open circuit voltage region. Consequently, the maximum power point moves towards large values of the voltage but lower values of the current, hence decreasing the electric power. In fact, as the intensity of the magnetic field in milliTesla (mT) was varied from 0 to 15, 0 to 30, and 0 to 50, the electric power at the maximum power point decreased by about 9%, 21%, and 48%, respectively.

3.3. Characteristic Values of the Photovoltaic Module. We present in this section the characteristics of the photovoltaic module under the influence of the magnetic field. The characteristics include current, voltage, and charge resistance

TABLE 3: Electric power and voltage of the photovoltaic module against the intensity of the magnetic field for a solar irradiance of 600 W/m².

V _{mod} (V)	B (mT)				Temperature at front side T ₁ (°C)	Temperature at back side T ₂ (°C)	Ambient temperature T ₃ (°C)
	0	15	30	50			
0	0	0	0	0	38.9	37.7	52.6
2	0.402	0.349	0.272	0.18	43.9	41.3	54.5
4	0.793	0.67	0.54	0.359	43.7	41.5	53.5
6	1.16	1.025	0.797	0.527	42	41.6	54.7
8	1.496	1.344	1.04	0.682	43	41.4	54.6
10	1.764	1.607	1.278	0.829	43.6	41.2	53.6
12	1.976	1.807	1.476	0.956	44.2	41	52.8
14	2.072	1.887	1.638	1.078	44.3	41.2	52.9
16	1.925	1.802	1.632	1.152	44	41.3	52.8
18	1.026	1.171	1.2	1.142	43.4	41	52.7
18.45	0.793	0.96	1.03	1.089	43.8	41.4	54
18.94	0.511	0.701	0.85	0.966	43.8	41	55.5
20	0	0.14	0.28	0.048	41.6	40.3	54.4
20.91	0	0	0	0.042	41.4	40.8	55
21.5	0	0	0	0	42.1	41.4	54.6

TABLE 4: Electrical parameters of the photovoltaic module against the intensity of the magnetic field and for a solar irradiance of 600 W/m².

B(mT)	P _{max} (W)	V _{max} (V)	I _{max} (A)	V _{oc} (V)	I _{sc} (A)	R _{MPP} (Ω)	FF (%)	η (%)
0	2.075	13.65	0.152	20.00	0,205	89.80	50.61	12.81
15	1.931	14.41	0.134	20.50	0,176	107.54	53.49	11.91
30	1.694	15.40	0.11	20.91	0.137	140.00	59.13	10.46
50	1.152	16.00	0.072	21.50	0.090	222.22	59.59	7.12

at the maximum power point (MPP), series and shunt resistances, maximum electric power, fill factor, and conversion efficiency.

3.3.1. Electrical Parameters of the Photovoltaic Module. The electrical parameters (current and voltage at maximum power point, maximum electric power, fill factor, conversion efficiency, and charge resistance at the maximum power point) of the photovoltaic module under magnetic field are found using the method proposed in previous works [8, 10].

During the test, while measuring the characteristics I-V and P-V, the solar irradiance was also simultaneously measured alongside. The retained values were those corresponding to a measured solar irradiance of 600 W. The incident irradiance falling on the photovoltaic module was calculated through the formula $P_{inc} S_{mod}$ and found to be 16.20 W; S_{mod} is the surface of the photovoltaic module, as defined in Section 2.1. The above calculated incident irradiance was used for the calculation of the conversion efficiency.

The results are presented in Table 4.

On one hand, these results show that the maximum electric power and the related conversion efficiency decrease with an increase of the magnetic field; on the other hand the fill factor and the resistance at the maximum power

point increase with an increase of the magnetic field. These experimental results are in agreement with the findings of the studies conducted on a silicon solar cell [10, 11] and on a silicon photovoltaic module [8, 11].

Within the limits of this study, it is clear that the efficiency of a solar module is affected by the presence of a magnetic field. However, the magnitude of ambient magnetic field generated by power transmissions lines and other equipment is extremely low (in the order of 10⁻² mT or less as illustrated in Table 5) as compared to the values of the magnetic field used in this study. That makes it difficult to conclude as to the impact of such field on solar photovoltaic installations.

3.3.2. Series and Shunt Resistances of the Equivalent Circuit of the Photovoltaic Module. The experimental values of the series and shunt resistances of the equivalent circuit of the photovoltaic module were calculated using equations suggested by Combari et al. [8].

Table 6 gives the series and shunt resistances of the equivalent circuit of the photovoltaic module.

The values of the series and shunt resistances of the equivalent circuit of the photovoltaic module increase with the intensity of the magnetic field. This is in line with the results achieved by the theoretical study [8].

TABLE 5: Magnetic field from high voltage power transmission lines [9].

Voltage (kV)	Magnitude of the magnetic field from high voltage power transmission lines according to distance to the source (mT)		
	0 m	30 m	100 m
400	0.03	0.012	0.001
225	0.02	0.003	0.0003
90	0.01	0.001	0.0001

TABLE 6: Series and shunt resistance of the equivalent circuit of the photovoltaic module as a function of the magnetic field and for a solar irradiance of 600 W/m^2 .

B(mT)	0	15	30	50
$R_s (\Omega)$	7.76	9.90	12.20	17.70
$R_{sh} (\Omega)$	257.547	363.430	562.590	888.889

4. Conclusions

This experimental study shows that the maximum electric power output of a photovoltaic module, hence its conversion efficiency, decreases when the intensity of the magnetic field increases. On the contrary, the fill factor and the resistance at the maximum power point do increase with the intensity of the magnetic field. The increase of the experimental values of the series and shunt resistances of the equivalent circuit of the photovoltaic module under magnetic field confirm its resistive behaviour called magnetoresistance.

Thus, the maximum electric power and the conversion efficiency are two electrical parameters extremely dependent on the intensity of the applied magnetic field. Consequently, the presence of relatively important magnetic fields in the neighborhood of a photovoltaic module decreases its performance.

However, it is difficult to conclude as to whether ambient magnetic field generated by power transmissions lines and other equipment have noticeable impact on solar photovoltaic installations, since the magnitude of such field is extremely lower compared to the values of the magnetic field used in this study.

The authors then recommend further studies that will narrow into magnetic fields in the order of those generated by power transmissions lines, transformers, and other equipment.

Data Availability

The data used to support the findings of this study are available from the corresponding author upon request.

Conflicts of Interest

The authors declare that there are no conflicts of interest regarding the publication of this article.

Acknowledgments

The authors would like to acknowledge the support of the International Science Program (ISP) for their research group.

References

- [1] M. E. Emeteri and M. L. Akinyemi, "Weather effect on photovoltaic module adaptation in coastal areas," *International Journal of Renewable Energy Research*, vol. 5, no. 3, pp. 821–825, 2015.
- [2] H. A. Koffi, V. C. K. Kakane, A. Kuditcher, A. F. Hughes, M. B. Adeleye, and J. K. A. Amuzu, "Seasonal variations in the operating temperature of silicon solar panels in southern Ghana," *African Journal of Science, Technology, Innovation and Development*, vol. 7, no. 6, pp. 485–490, 2015.
- [3] F. Dia, N. Mbengue, M. Diagne, O. A. Niassé, B. Ba, and C. Sene, "Contribution to the Study of the Degradation of Modules PV in the Tropical Latitudes: Case of Senegal," *Research Journal of Applied Sciences, Engineering & Technology*, vol. 12, no. 4, pp. 427–438, 2016.
- [4] H. A. Kazem, T. Khatib, K. Sopian, F. Buttinger, W. Elmenreich, and A. S. Albusaidi, "Effect of dust deposition on the performance of multi-crystalline photovoltaic modules based on experimental measurements," *International Journal of Renewable Energy Research*, vol. 3, no. 4, pp. 850–853, 2013.
- [5] Y. Betsler, D. Ritter, G. Bahir, S. Cohen, and J. Sperling, "Measurement of the minority carrier mobility in the base of heterojunction bipolar transistors using a magnetotransport method," *Applied Physics Letters*, vol. 67, no. 13, pp. 1883–1884, 1995.
- [6] R. R. Vardanyan, U. Kerst, P. Wawer, and H. Wagemann, "Method for measurement of all recombination parameters in the base region of solar cells," in *Proceeding of the 2nd World Conference and Exhibition on Photovoltaic Solar Energy Conversion*, vol. I, pp. 191–193, Vienna, Austria, July 1998.
- [7] S. Erel, "Comparing the behaviours of some typical solar cells under external effects," *Teknoloji*, vol. 11, pp. 233–237, 2008.
- [8] D. U. Combari, I. Zerbo, M. Zoungrana, E. W. Ramde, and D. J. Bathiebo, "Modelling Study of Magnetic Field Effect on the Performance of a Silicon Photovoltaic Module," *International Journal of Energy and Power Engineering*, vol. 09, no. 08, pp. 419–429, 2017.
- [9] Ministère de l'Agriculture et de la pêche. Mieux connaître les risques des courants électriques parasites dans les exploitations d'élevage Groupe Permanent sur la Sécurité Electrique dans les élevages agricoles et aquacoles, 2003. Accessed August 20, 2018. http://www.gpse.fr/IMG/pdf/plaquette_courants_parasites.pdf.

- [10] I. Zerbo, M. Zougrana, I. Sourabié, A. Ouedraogo, B. Zouma, and D. J. Bathiebo, "External Magnetic Field Effect on Bifacial Silicon Solar Cell's Electrical Parameters," *International Journal of Energy and Power Engineering*, vol. 08, no. 03, pp. 146–151, 2016.
- [11] H. Fathabadi, "Effect of External AC Electric and Magnetic Fields on the Power Production of a Silicon Solar Cell," *IEEE Journal of Photovoltaics*, vol. 8, no. 6, pp. 1408–1412, 2018.